

A Computational Based Approach Linking Spatial and Temporal Pattern Stiffness to
Decreased Lung Function in Idiopathic Pulmonary Fibrosis

A dissertation submitted in partial fulfillment of the requirements for the degree of
Doctor of Philosophy at George Mason University

By

John Sangobowale
Master of Business Administration
Iona College, 2011
Bachelor of Science
University of Virginia, 2009

Director: Dr. Ancha Baranova, Professor
Department of School of Systems Biology

Summer Semester 2022
George Mason University
Fairfax, VA

Copyright © 2022 by John Sangobowale
All Rights Reserved

Dedication

I dedicate this dissertation to my parents for all of their love and support, and making me believe I can accomplish anything I put my mind to. Love you always.

Acknowledgments

I would like to thank the members of my dissertation committee, Dr. Ancha Baranova, Dr. Naomi L. Gerber, and Dr. Dmitri K Klimov for generously taking time out of their schedules to help support and guide me throughout this process. In addition, I would like to thank my sister Christine Sangobowale for her assistance in reviewing this document and her continued support throughout my academic career. I would also like to thank Dr. Tyrus Berry and Dr. Tim Sauer in the Department of Mathematical Sciences, and Dr. Yotam Gingold in the Department of Computer Science for aiding me in troubleshooting my models. Lastly, I would like to give a special thanks to my dissertation advisor, Dr. Jason Kinser for his continued support and mentorship throughout this process. He was essential to me in completing this study, without his constructive feedback, flexibility, and encouragement I wouldn't have been able to complete this dissertation.

Table of Contents

	Page
List of Figures	vii
Abbreviations	x
Abstract	xi
1 Introduction	1
1.1 Tissue Repair	2
1.1.1 Conventional Repair vs Fibrosis	2
2 Idiopathic Pulmonary Fibrosis	4
2.1 What is Idiopathic Pulmonary Fibrosis?	4
2.1.1 Epidemiology and Risk Factors Associated with IPF	5
2.1.2 Clinical Evaluation of IPF	6
2.2 Pathobiology of IPF	7
2.2.1 Origin of Fibroblast	7
2.2.2 Extracellular Matrix	9
2.2.3 TGF- β and IPF	9
2.2.4 Epithelial-to-Mesenchymal Transition	10
2.2.5 Endoplasmic Reticulum Stress	11
2.3 Radiological Features of IPF	11
2.4 Classification of Interstitial Lung Diseases	14
2.5 The Use of HRCT in Diagnosing IPF	15
2.5.1 Defining IPF in IIPs	16
2.5.2 HRCT and IPF	16
3 Research Methodology	19
3.1 Background and Significance	19
3.2 Specific Aim	23
4 Model Development	26
4.1 Parts of The Network Model	26
4.1.1 Hexagonal Lattice	27
4.1.2 IPF and Disease Regions	29

4.1.3	Pulmonary Ventilation	38
4.1.4	Force and Velocity	40
4.1.5	Energy Minimization	42
4.2	System Iteration	45
5	Model Validation	50
5.1	Force and Velocity	50
5.2	k Constant	53
5.3	Multi-Hexagon Validation	55
5.3.1	Pulmonary Ventilation	58
5.3.2	Energy Minimization	60
6	Model Results	63
6.1	Structural Progression of IPF	64
6.2	Decrease in Mechanical Properties	66
6.3	Model Parameter Tuning	69
7	Discussion	75
7.1	Model Iteration Motivation	75
7.2	Spatial Pattern Stiffness and Pulmonary Deviation	79
7.3	Model Shortcomings and Possible Improvements	83
8	Summary	86
8.1	Model Development	86
8.2	Model Validation	87
8.3	Results and Discussion	88
9	Conclusion	89
	Bibliography	90

List of Figures

Figure	Page
2.1 HRCT image of patient with advanced IPF.	12
2.2 Depiction of well defined UIP characteristics in the peripheral portions of the lungs, with less interior fibrotic effects.	13
2.3 Comparison of chest HRCT from a patient who experienced an acute exacerbation of IPF.	14
2.4 Classification of known and unknown etiologies of interstitial lung diseases.	15
2.5 Highlights the hallmark radiological feature of IPF, honeycombing.	17
2.6 Chest HRCT comparing a healthy lung to a lung with progressive radiological features of IPF.	18
4.1 Comparison of hexagon lattice structure and alveolar tissue to highlight structural similarities.	27
4.2 A snapshot of the hexagonal grid, and the mathematical properties used to construct the lattice structure.	29
4.3 Original IPF HRCT image used during model development to construct the network model.	30
4.4 A snapshot of the binary segmented model image.	31
4.5 A look into the various extracted features of the Model image after segmenting the lung.	32
4.6 The isolated right lung after feature extraction.	33
4.7 Critical image parameters used in developing the network model regions. . .	34
4.8 Region definitions for the model image highlighting the unique parts of the lung used to define the probability criteria.	35
4.9 Applying the scaling factor to map the network structure to the lung boundaries from the model image.	36
4.10 Each region in the lattice structure is represented by a unique color corresponding to its network definition.	37
4.11 The network structure depicting the structural boundary of the lung structure.	38
4.12 Overview of the process steps for the IPF simulation model.	45

5.1	Validation testing for the movement of the node about the network to verify the force and velocity definitions.	51
5.2	Analytical model solutions vs Computational derived solutions for selected model function.	52
5.3	Graphs of the force and velocity energies, and the position of the center of mass, to validate the conservation of energy and movement of nodes within the system.	53
5.4	Evaluation of different spring constants on the applied node in a single hexagon network.	55
5.5	Validation of a multi-hex, 3 by 3 network, with its perimeter nodes held static.	56
5.6	Iteration vs energy graph used to validate a 3 by 3 grid system.	57
5.7	Graph of the system validation energies for a 3 by 3 grid network, increasing the k midway through the simulation.	58
5.8	Cross sectional depictions of the baseline, expanded, and contracted network configurations around the center of mass.	59
5.9	A graphical representation highlighting a constant center of mass of the network as the model expands and contracts.	60
5.10	Displays the decrease in spring energy as the energy minimization function searches for a global minimum.	62
6.1	Cross sectional depictions of the simulation model at $N = 100$ and $EquLen = 0.3$ capturing the progressive onset of fibrosis about the network model. . .	65
6.2	Graph of $N = 100$ and $EquLen = 0.3$ network simulation capturing the expansion and contraction energies.	66
6.3	Graph of the PE and Percolation Threshold for the expanded state of $N = 100$ and $EquLen = 0.3$ highlighting the distinct slope changes between regions.	68
6.4	Network model configurations comparing the progression on IPF of $N = 25$ and $N = 100$ when $EquLen = 0.3$	71
6.5	Underlined trend in energy as local incidences of fibrosis, N are varied when $EquLen = 0.3$ for the expanded state.	72
6.6	Network model configurations comparing the progression on IPF when adjusting for $EquLen = 0.7$ vs $EquLen = 0.3$ when $N = 100$	73
6.7	PE trends highlighting the differences in slope when the equilibrium lengths of the network are varied when $N = 100$	74

7.1	Comparison of network model at 25% stiffness to a HRCT image of a patient with early onset radiological symptoms of IPF.	77
7.2	Comparison of network model at 50% stiffness to a HRCT image of a patient with established radiological symptoms of IPF.	78
7.3	Comparison of network model at 75% stiffness to a HRCT image of a patient with late stage radiological symptoms of IPF.	79
7.4	Focused views of the network model and HRCT image capturing distinct characteristics of honeycombing.	81
7.5	Focused views of the network model and HRCT image capturing distinct characteristics of traction bronchiectasis, septal thickening, and reticulation.	82

Abbreviations

<i>IPF</i>	— Idiopathic Pulmonary Fibrosis
<i>ECM</i>	— Extracellular Matrix
<i>MMP</i>	— Matrix Metalloproteinases
<i>TIMPs</i>	— Tissue Inhibitor of Metalloproteinases
<i>PDGF</i>	— Platelet-Derived Growth Factor
α - <i>SMA</i>	— Alpha-Smooth Muscle Actin
<i>EMT</i>	— Epithelial-Mesenchymal Transition
<i>TGF-β</i>	— Transforming Growth Factor-Beta
<i>EndMT</i>	— Endothelial-Mesenchymal Transition
<i>PRRs</i>	— Pattern Recognition Receptors
<i>PAMPs</i>	— Pathogen-Associated Molecular Patterns
<i>LTBP</i>	— Latent TGF- β Binding Protein
<i>LAP</i>	— Latency-Associated Protein
<i>ILD</i>	— Interstitial Lung Disease
<i>IIP</i>	— Idiopathic Interstitial Pneumonia
<i>UIP</i>	— Usual Interstitial Pneumonia
<i>ER</i>	— Endoplasmic Reticulum
<i>TNF-α</i>	— Tumor Necrosis Factor-Alpha
<i>UPR</i>	— Unfolded Protein Response
<i>AE – IPF</i>	— Acute Exacerbation of Idiopathic Pulmonary Fibrosis
<i>SP – C</i>	— Surfactant Protein-C
<i>SNP</i>	— Single-Nucleotide Polymorphism
<i>HRCT</i>	— High Resolution Computed Topography
<i>IIP</i>	— Idiopathic Interstitial Pneumonia

Abstract

A COMPUTATIONAL BASED APPROACH LINKING SPATIAL AND TEMPORAL PATTERN STIFFNESS TO DECREASED LUNG FUNCTION IN IDIOPATHIC PULMONARY FIBROSIS

John Sangobowale, PhD

George Mason University, 2022

Dissertation Director: Dr. Ancha Baranova

Idiopathic pulmonary fibrosis (IPF) is a chronic, progressive disease of unknown etiology that is characterized by the histopathological pattern of usual interstitial pneumonia. The pathogenic mechanisms that regulate the activation, differentiation, and proliferation of fibroblast have been at the central stage of efforts to understand the biological pathway that drives the fibrotic process. Despite the extensive knowledge on the pathogenesis of IPF, the mechanical dysfunction associated with the remodeling of the lung tissue is still not fully understood. This study developed a computational based approach to study the pulmonary mechanics of a hexagonal lattice network of alveoli-like structures to improve understand of the mechanical properties of the lung. A dynamic probabilistic representation of a closed two-dimensional elastic model of nodes and springs was constructed from a baseline High Resolution Computed Topography (HRCT) IPF image. The progressive development of fibrosis was reconstructed from early to late-stage representations of IPF images. Given a predefined probability, regional collagen deposition was simulated by increasing random isolated lesions of the alveolar wall, represented by springs in the lattice model. The local onset of fibrosis was initialized by stiffening

springs along a strain-dependent random walk to account for excess deposition of extracellular matrix and tissue remodeling as the lung deviates from its normal geometry. The regional deposition of collagen and the local manifestation of fibrosis were represented by increasing the elastic constant of the spring at the site of initiation and springs along a strain dependent random walk of length N , by a factor of 100. The value of N representing the maximum distance the spread of fibrosis was allowed to travel from its initiation site in the network model. After each expansion and contraction, the nodes were allowed to move in the direction of the applied force, while the total spring energy of the network was minimized. The cycle was repeated until all the springs k constants in the network model were increased. This study focused on modeling and analyzing various functions of the lung, and its parameters to construct a novel approach to recreate early to late-stage cross sectional representations of IPF. The model was proven to show that the onset of fibrosis tends not to follow a linear path, but establishes a sharp increase in energy as the lung structure reaches a critical threshold. The shift in slope as the concentration of spring stiffness increased was broken down into three distinct regions, $< 25\%$ (early onset), $\geq 25\%$ and $\leq 75\%$ (progressive), and $> 75\%$ (late stage) of the disease. This study provided a new approach to examining how pulmonary mechanics and spatial orientation of lung tissue affects the progression of IPF, and developed a framework to model other biological systems.

Chapter 1: Introduction

The respiratory system is a complex network that assists in enriching blood with oxygen and expelling carbon dioxide and waste products from the body. When the lung is inflated and contracted, stress is introduced in the alveolar walls by the increased pressure introduced by the disequilibrium of the lungs resting volume. The inhaled oxygen travels through the trachea, bronchi, and bronchioles until it reaches the alveoli. The alveoli, or air sac are surrounded by capillaries where gas exchange occurs; oxygen molecules travel into the capillaries to enrich the blood while waste products such as carbon dioxide gets removed and exhaled from the body. The alveolar walls must be thin enough to allow for gas exchange, but strong to withstand the countless stress-strain cycles of the lung. In some people this process might be compromised by complications in the lungs interstitium, which is a descriptive term for the collection of supporting tissue within the lung. More specifically, in patients with idiopathic pulmonary fibrosis (IPF), which is categorized as a non-neoplastic pulmonary disease that attributes to the formation of scar tissue within the lungs [1] and destroys the functional components of the interstitium, which leads to overall organ failure. Under normal circumstances fibroblasts lay dormant. However, they may lose negative control of the collagen production, which triggers the cascade of problems. This leads to the distortion of the lungs structural design and functionality, which ultimately results in organ failure and death. IPF affects the middle-age and elderly populations and progresses with age. Progression of the disease varies from person to person, its underlined cause is still debated. IPF has little to no treatment options, and mortality rates are high due to respiratory failure, pulmonary hypertension, heart failure, pulmonary embolism, pneumonia, and lung cancer [2, 3]. In addition, it is still not fully understood why certain individuals are more predisposed to the disease than others.

1.1 Tissue Repair

Acute inflammation takes place as an immediate response to trauma caused to the body. It may be regarded as the body's first line of defense against injury. Inflammation involves rapid vascular changes, edema, and recruitment of leukocytes to the affected area. Prolonged, or chronic inflammation, is characterized by simultaneous repair and tissue remodeling proceeding along the inflammatory response; fibrosis typically results from this extended period of inflammation. Although most fibrotic disorders have distinct etiological and clinical features, they share the commonality of the production of aggregates that leads to the destruction of normal tissue architecture.

Normal tissue repair can essentially be broken down into a two-phase process, the initiation phase, where signals initiate the replacement of injured cells to be replaced by normal healthy cells of the same type, followed by the repair phase, where the proliferation of fibroblast is used to form new connective tissue. Under normal circumstances this process leads to restoration of tissue functionality, however, if the process becomes disruptive, it may lead to the loss of function.

1.1.1 Conventional Repair vs Fibrosis

When epithelial and/or endothelial cells are damaged, an immune response is triggered which releases a cascade of signaling molecules that initiates an anti-fibrinolytic response that promotes the formation of blood-clots and provisional ECM [4]. Immediately following damage, vasoconstriction is activated by vasoactive mediators, such as epinephrine, serotonin, and thromboxane, to limit blood loss. Hemostasis is initialized through the aggregation of the platelets when attached to the vascular wall leading to clot formation. Attachment of the platelets to the exposed collagen surfaces activate platelet degranulation which release cytoplasmic granules preloaded with mediators such as platelet-derived growth factor (PDGF), the vasoactive substances, and cytokines/chemokines to promote the generation of new platelets, increase their aggregation, and attract inflammatory cells to the site of injury. Within the provisional ECM, cytokines, chemokines, and growth factors

are activated to provide the biochemical support for the further recruitment of leukocytes. Neutrophils, lymphocyte, and monocytes are key players in the immune response; normally, they eliminate invading organisms, tissue debris, and dead cells. This is achieved only after blood flow is increased as histamine activates vasodilation. At this time, profibrotic cytokines and growth factors, such as transforming growth factor-beta (TGF- β), the Th2 cytokines, interleukin 1 (IL-1) and platelet-derived growth factor (PDGF) are secreted from the lymphocytes and other cells in the ECM and supplement the activation of macrophages and fibroblasts [5, 6]. In granulation tissue, fibroblasts are activated. They acquire α -smooth muscle actin (α -SMA) expression to become myofibroblasts capable of remodeling of the granulation tissue, enabling it to produce of collagen, elastin, and fibronectin. Collagen is secreted to the ECM in the form of procollagen, and is cleaved to produce tropocollagens. The aggregation of tropocollagens produces collagen filaments. Myofibroblast along with collagenases and matrix metalloproteinases (MMPs), and its inhibitor tissue inhibitor of metalloproteinases (TIMPs) assist to promote wound contraction and maturation [7]. Epithelial and/or endothelial cells constantly divide, and a balance is created that synthesizes and removes collagen in a harmonic fashion until the tissue is fully healed. Once the wound is healed, the production of the ECM components that promote remodeling are halted. Changes to cell signaling resulting in uncontrollable inflammation and prolonged repair, including sustained production of growth factors, may lead to excess accumulation of ECM components.

When the rate of new collagen generation surpasses the rate at which it is degraded, fibrotic clump is formed. Thus, excess deposition of collagen results in the formation of permanent scar tissue.

Chapter 2: Idiopathic Pulmonary Fibrosis

The culmination of fibrosis due to an unknown cause is a major characteristic of Idiopathic Pulmonary Fibrosis (IPF). There are many risk factors associated with IPF, some which are age dependent, while others possess genetic predispositions. Manifestation of IPF is usually categorized by its pathological features, but to understand the underlying causes of the disease its pathobiology must be fully understood. Clinical evaluation of IPF is detrimental to the diagnosis of IPF. Early detection of IPF can lead to a more diverse set of treatment options and better quality of life.

2.1 What is Idiopathic Pulmonary Fibrosis?

Idiopathic is a term used to describe a condition or process of occurrence which is unknown. Idiopathic Pulmonary Fibrosis is an Interstitial Lung Disease (ILD) characterized by chronic inflammation and displays the pathoradiological pattern of Usual Interstitial Pneumonia (UIP) [8]. The general consensus and current hypothesis for the causality of IPF is that an unidentified stimulus or stimuli causes repeated injury to the alveolar epithelium which leads to an abnormal repair response. Epithelial cells are subjected to Endoplasmic Reticulum (ER) stress which leads to TGF- β activation, recruitment of profibrotic cytokines such as tumor necrosis factor-alpha (TNF- α), and transition to mesenchymal phenotype. Fibroblast produces collagen-secreting mesenchymal cells that trigger the repair process; however, in IPF this repair process becomes impaired which leads to the dysregulation of normal tissue homeostasis. The dysregulation of normal tissue repair and lifecycle of fibroblasts allow fibrosis to manifest. Although straightforward, lung remodeling and the development of fibrosis rely on a collection of adverse exposures and predefined factors.

The pathophysiological of IPF can be subdivided into three stages [9]. The first stage can

be categorized as the predisposition stage, were genetic mutations or variations predispose individuals to the development of fibrosis. Not all individuals in this stage will develop a clinically relevant disease state; whether or not will depend on a particular combination of inherited mutated variants. The next stage, the initiation stage is marked by the activation and recruitment of molecular mediators that are responsible for epithelial cell dysfunction such as ER Stress, excessive TGF- β activation, TNF- α , chemokines that lead to EMT, fibrocyte recruitment, and fibroblast differentiation [9]. The collection of mediators in the initiation stage leads to the progression stage, during which mesenchymal cells release abnormal quantities of ECM proteins, which trigger the remodeling and formation of scar tissue in the lung. The recurring cycle of repair leads to the manifestation of fibrosis in IPF patients. Although the pathophysiology of IPF can be generally subdivided into three stages, individuals with IPF may circumvent some of these stages as the disease develops.

2.1.1 Epidemiology and Risk Factors Associated with IPF

Cases of IPF are on an upward trend over the recent years with an estimated prevalence of 50 per 100,000 cases [10]. IPF, the most common form of the Idiopathic Interstitial Pneumonias (IIP) and ILD have slightly different prevalence and incidence in men versus women. In the United States, the overall prevalence of IPF is 13.2 per 100,000 for women and 20.2 per 100,000 for men, whereas incidence cases were 7.4 per 100,000 persons for men and 10.7 per 100,000 persons for women [11]. Notably, the prevalence of IPF rises dramatically with the increase in age. The pathophysiological symptoms of IPF are rarely seen in individuals younger than 50 years, but present in about 0.2% of those older than 75 [10]. The median survival rate of patients with IPF at the time of diagnosis is 3 years. Nevertheless, some patients live well beyond this mark. Respiratory failure resulting from disease progression is the most common cause of mortality [12, 13]. Some patients with IPF experience acute exacerbations, defined as the sudden worsening of symptoms like shortness of breath [14]. These episodes are associated with a higher risk of death in patients with IPF, yet no cause can be found as to what triggers the event [15]. The acute exacerbation experienced

in IPF patients are theorized to accelerate the underlying symptoms of the disease, and might be triggered by an infection or exposure to environmental pollutants [16, 17]. Toxic environmental exposures seem to be a recurring factor in patients that exhibit symptoms of IPF. Pollutants such as smoke, biological antigens, or dust may contribute to development of lung fibrosis in genetically predisposed individuals. One study showed that patients that were exposed to smoke and/or dust were found to possess IPF more often than non-exposed individuals [18].

Pulmonary fibrosis has been seen in cohorts of families, leading to the belief that there could be a genetic predisposition to at least some forms of the disease [19]. Surfactant protein C (SP-C) expression is confined to alveolar type II cells. SP-C is highly expressed in lung tissue and is necessary for the reduction of alveolar surface tension [20]. Abnormalities found in the SP-C encoding gene in a mother and daughter pair who had ILD provided support to the role of genetic factors in ILDs [20–22]. Although evidence supports causative role of SP-C mutations in specific cases of pulmonary fibrosis, these mutations only account for 1% of the IPF cases [9]. A whole-genome linkage study was conducted on individuals with pulmonary fibrosis using a single-nucleotide polymorphism (SNP) panel of more than 6,000 markers [23]. Chromosome 10q22 region was identified as harboring genes responsible for the disease.

2.1.2 Clinical Evaluation of IPF

Symptoms of IPF include occasional chest pain, dry cough, decrease tolerance for physical activity, and shortness of breath. These symptoms typically last for an extended period of time such as months or years and may persist even when the patient is at rest. Individuals that show signs of these symptoms may be diagnosed by a health care provider or other medical professions through testing and knowledge of a medical history. A typical medical history assessment usually begins with a questionnaire of the patient’s activities such as if the patient is a smoker, and/or if they have ever been exposed to asbestos or other environmental dangers. Next, a physical exam may be performed, in the examination the

healthcare provider will try to identify if the patient exhibits crackles in their breathing. Crackles are often associated with inflammation or infection of the lung, and can be a symptom of IPF. Physicians also look to see if there are any signs of cyanosis, such as blue discoloration of the skin around the mouth or fingernails due to the lack of oxygen in the blood and clubbing which is the enlargement of the fingernail beds. The collection of these symptoms results in a disease progression to advance stages of IPF.

A more definitive methodology to diagnosis IPF is to take a combined approach of qualitative and quantitative methods. Medical testing including but not limited to bronchoscopy, chest High Resolution Computed Topography (HRCT) scan, chest X-ray, measurements of blood oxygen levels, pulmonary function tests, surgical lung biopsy, and test for connective tissue disease such as rheumatoid arthritis, lupus, or scleroderma can all be used to better differentiate IPF from other interstitial lung diseases.

2.2 Pathobiology of IPF

Idiopathic Pulmonary Fibrosis is an unremitting fibrotic disease that accumulates over the span of a lifetime. The mechanisms of the disease amassing over time are still unknown. Theories on how individual components contribute to the diseases progression are currently being tested and modeled; each of these contributors play essential role in our understanding of the diseases development and progression.

2.2.1 Origin of Fibroblast

Mesenchymal cells embedded within the interstitial spaces between cell structures are called resident mesenchymal cells. Fibroblast is found in every tissue of the human body; they are cells responsible for the production of collagen and other fibers. Fibroblast is the architect of the design for the structural properties of the connective tissue which is determined by the characteristics of the ECM. Resident mesenchymal cells are a major source of fibroblast in fibrosis [24]. Fibroblasts are also produced within the epithelium by a process called epithelial-mesenchymal transition (EMT) [25]. It is also hypothesized that fibroblast are

also produced in the endothelium by ways of endothelial-mesenchymal transition (EndMT) [26]. Myofibroblasts are differentiated from fibroblasts by acquiring the cytoskeletal characteristics of contractile smooth muscle cells via their production of α -SMA [27]. Depending on their location fibroblast can display a variety of morphologies.

Fibroblasts and IPF

Under normal conditions fibroblast remains inactive and expresses few smooth muscle actin and trigger little ECM production [28]. After tissue injury, several signaling molecules are activated which trigger the activation, migration, and differentiation of fibroblast to synthesize ECM components. Differentiation of fibroblast is achieved through several mediators, including TGF- β , PDGF, IL-4, IL-13, and high extracellular stress. These mediators promote recruitment of inflammatory cells and mesenchymal activation which give rise to activated myofibroblasts. In IPF, excessive activation of fibroblast leads to the appearance of profibrotic myofibroblasts, commonly seen in the diseased lung [9]. Unlike resident lung fibroblast, myofibroblasts secrete ECM components which include type I and type III collagen. Under normal circumstances once damaged tissue is restored myofibroblast undergoes apoptosis, and tissue architecture and function are restored. In IPF, accumulation of fibroblast and activated myofibroblast in the lung interstitium leads to the deposition of excesses type I collagen. Elevated levels of type I collagen eventually lead to excessive tissue remodeling and lung fibrosis. Small concentrated areas of newly formed fibroblast coupled with ECM proliferation are termed fibroblastic foci. As these areas continue to expand and grow some of the fibroblast infiltrate the epithelium and end up damaging the epithelial cell exposing the underlying alveolar basement membrane [29]. This exposure allows the fibroblast and myofibroblast to infiltrate the alveolar space which leads to further deposition of ECM and profibrotic mediators that destroy the basement membrane. Normally fibroblast is removed from the site of tissue injury after repair has been completed, however, disruptions in the apoptotic pathways led to apoptosis resistant fibroblast which is the main element in continued fibrosis in IPF [30].

2.2.2 Extracellular Matrix

Extensive pathological remodeling of extracellular matrix by fibroblast is responsible for the progressive development of fibrosis in IPF. The supportive tissue of epithelial organs consists of the cells and connective tissue that hold the various ECM products [31]. Homeostasis of ECM is controlled by fibroblast through the communication of cells within the stroma [32]. The overabundance of type I and III collagen and various signaling proteins are present when functional abnormalities are seen in the ECM. Although the ECM is a critical component in the development of fibrosis in IPF, it's still not exactly known how the mechanisms are altered that lead to structural remodeling. One study suggests that translational control of proteins with the stroma directs a positive feedback loop between profibrotic matrix and fibroblasts; this loop propagates fibrosis and tissue remodeling [33]. Extensive research has been dedicated to the understanding of the ECM and its components. By fully comprehending its biological mechanisms, one could possibly assist in developing therapies that inhibit the overproduction of collagen and restore homeostasis to the ECM in IPF.

2.2.3 TGF- β and IPF

One of the most studied proteins in the regulation of the ECM has been TGF- β . TGF- β is a multifunctional cytokine that exist in three isomer forms, TGF- β 1, -2 and -3 and is responsible for the development of fibrosis in a number of diseases [34]. Each of the distinct isoforms of TGF- β exhibit similar biological activity, although TGF- β 1 is primarily attributed to the formation of tissue fibrosis. TGF- β is secreted by many cell types, however circulating monocytes and tissue macrophages are the predominant cellular sources [7]. In patients with IPF, elevated levels of activated TGF- β can be found inside the lungs. These elevated levels are responsible for the excess accumulation of fibrous connective tissue. Normally, TGF- β is stored inside the cell as a disulphide-bonded homodimer non-covalently bound to LAP. This interaction keeps TGF- β inactive. However, during the development of lung fibrosis alveolar epithelial cells express increased levels of integrin α v β 6 [35] which is an

epithelia specific receptor for the ECM protein fibronectin [36]. This increased production of integrin $\alpha v\beta 6$ is only regulated during tissue injury and in the production of TGF- β . Activation of TGF- β requires dissociation from LAP; this is achieved by the mechanical tension facilitated by the binding of $\alpha v\beta 6$ to the small latent complex (SLC) and LTBP [37]. Because this process is catalyzed by several agents, a number of those agents have been targeted in the production of anti-fibrotic drugs. Once activated, TGF- β promotes the transcription of procollagen I and III [38]. TGF- β is thought to play a central role in the pathological process underlying IPF. TGF- β not only stimulates the production of various extracellular matrix proteins, but also inhibits the degradation of these same matrix proteins leading to increased production of fibrous agents [39]. Development of therapeutic processes that would allow for the proper balance of TGF- β positive and negative effects are the focus of many IPF studies.

2.2.4 Epithelial-to-Mesenchymal Transition

Epithelial cells are attached to the basement membrane by its basal surface and can undergo epithelial to mesenchymal transition (EMT) by a biological process that allows epithelial cells via multiple biochemical processes to acquire the molecular and cell physiological phenotype of mesenchymal cells [34]. This molecular reprogramming provides the newly acquired cells the ability to increase the production of ECM components, enhance resistance to apoptosis, and increase migratory capacity [26]. EMT can be classified into three subtypes, Type 1 EMT, which is responsible for EMT during implantation, embryogenesis, and organ development. Type 2 EMT, which is EMT associated with tissue regeneration and organ fibrosis, and Type 3 EMT, which is associated with cancer progression and metastasis [34]. Alveolar cells typically exhibit type 2 EMT in IPF patients; inflammatory injury to the lung can result in the recruitment of a diverse array of cells that trigger the EMT. Although epithelial cells acquire mesenchymal features in IPF pulmonary lobules, understanding the importance of how it promotes the differentiation of epithelial cell to fibroblast and how it aids in the fibrotic process is a major focus of study.

2.2.5 Endoplasmic Reticulum Stress

The Endoplasmic Reticulum (ER) is a network of interconnected membranous tubules responsible for the production of proteins and lipids. The ER has a number of functions within the cell; which includes the synthesis, folding, modification, and transport of proteins via the Golgi apparatus. ER homeostasis can be interrupted when there is an imbalance in the demand for protein synthesis, ability to produce, fold, and transport proteins, or when viral infections, environmental toxins, and inflammatory cytokines stress the system [40, 41]. In response to the stress, the ER activates the Unfolded Protein Response (UPR). The UPR is initiated by three proteins, inositol requiring 1 (IRE1), PLR-like ER kinase (PERK), and activating transcription factor 6 (ATF6) [40]. The activated UPR regulates the biochemical pathways to increase folding to reduce ER stress by decreasing the amount of unfolded proteins. As the ER regains equilibrium negative regulation of UPR is activated to prevent hyperactivity. If the cell cannot reestablish homeostasis by the UPR the cell is triggered for apoptosis [40, 42]. Elevated levels of UPR markers have been found in alveolar type II cells in IPF patients[43]. Therefore, if a complete understanding of the biological mechanisms surrounding how ER stress is controlled and how UPR is activated, we can better understand the mechanisms of IPF.

2.3 Radiological Features of IPF

Pathological distinctions of the lung are used to differentiate IPF from other interstitial lung diseases. The term usual interstitial pneumonia is used to describe the morphologic and histological patterns of ILD and is most often associated with IPF. UIP is associated with the temporal heterogeneity of areas of normal lung tissue, interstitial fibrosis, and dense areas of collagen producing myofibroblasts and matrix deposition called fibroblastic foci [44]. Fibrosis is mostly observed in the inferior portions of the lower lobe, with subpleural reticular opacities, honeycombing, and traction bronchiectasis, as seen in Figure 2.1 [44, 45].



Figure 2.1: Patient with advanced IPF. Chest HRCT shows peripheral and subpleural bilateral reticular abnormalities, with honeycombing, and traction bronchiectasis.

These patterns are often associated with UIP and are the fundamental radiological features of IPF in the lungs. The spatial heterogeneity of UIP represents normal lung immersion with diseased lung. Both the temporal and spatial patterns of UIP are well established in the peripheral portions of the lungs and spare the central portion. Moreover, the characteristic patterns of UIP decrease as one moves from the outer portion of the lobule to the center, as seen in Figure 2.2 [9]. The central portion of the pulmonary lobule exhibits normal tissue formation with little to no inflammation or fibrosis.

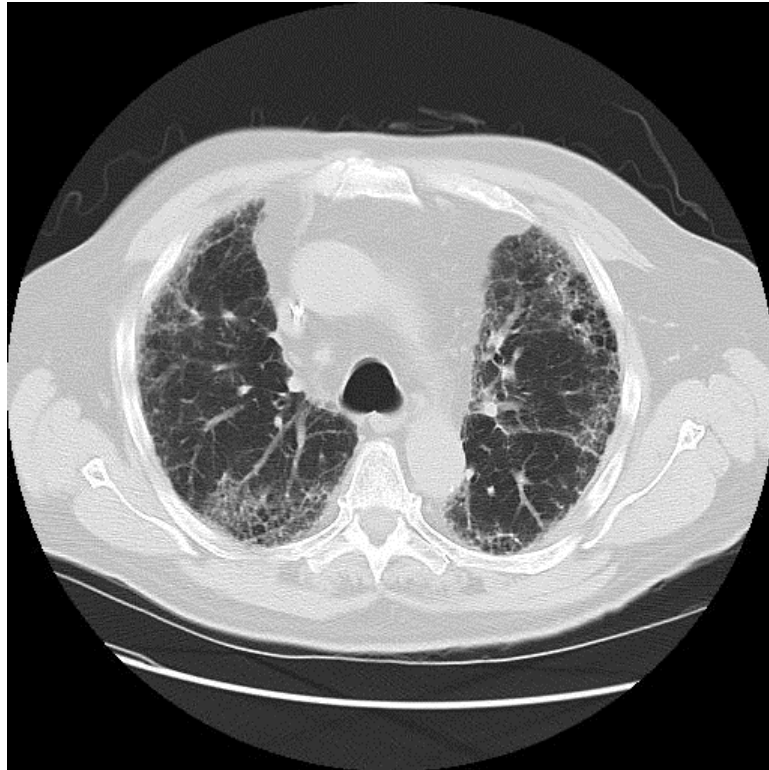


Figure 2.2: Depiction of an IPF patient with well defined UIP characteristics in the peripheral portions of the lungs, with the interior portion exhibiting lesser fibrotic effects.

When damage to the lung that typically lacks significant chronic fibrosis is observed it can readily be attributed to an episode of acute exacerbation of IPF, AE-IPF, Figure 2.3. The classic radiological pattern of the peripherals of the pulmonary lung remain intact while the central portions of the lobule show acute lung injury with edema, alveolar septal thickening, and airspace fibrin [9].

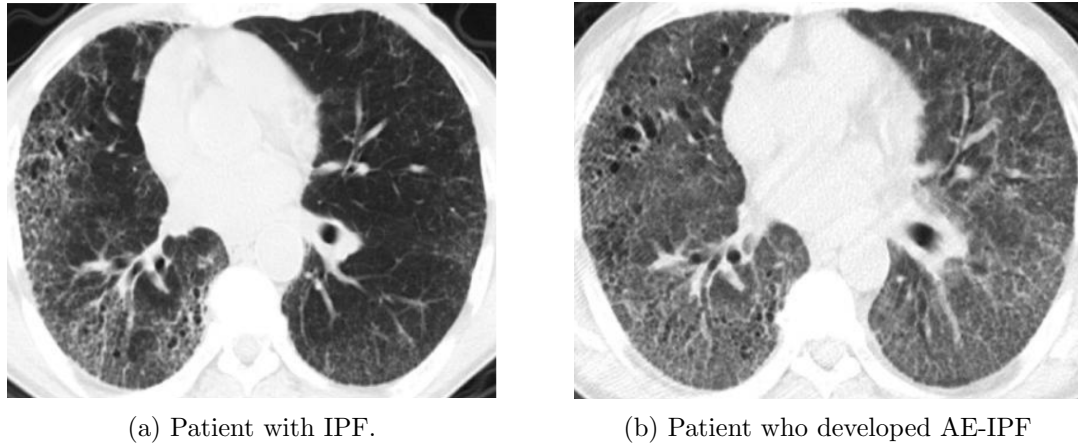


Figure 2.3: Chest HRCT of a patient who developed AE-IPF, which depicts diffuse ground glass opacities and acute lung injuries. Source: Hui Qiu, et al. *Front Immunol.* 2017.

2.4 Classification of Interstitial Lung Diseases

Without a lung biopsy diagnosis of interstitial lung diseases possess a level of uncertainty. Proper classification of ILDs is critical to the treatment and welfare of individuals with ILDs. High Resolution Computed Topography (HRCT) and clinical data are used to aid in the differential diagnosis of ILDs in the absence of a lung biopsy. Currently there is no standardized system for collecting and scoring the extent of ILDs, however, ILDs can be subdivided into two generalized categories consisting of known and unknown etiologies. Figure 2.4 shows that, upon further subclassification, the unknown etiologies yield a group of clinically and pathological distinct diseases termed Idiopathic Interstitial Pneumonias (IIPs). The IIPs are comprised of major idiopathic interstitial pneumonias (idiopathic pulmonary fibrosis (IPF), idiopathic nonspecific interstitial pneumonia (NSIP), respiratory bronchiolitis-interstitial lung disease (RB-ILD), desquamative interstitial pneumonia (DIP), cryptogenic organizing pneumonia (COP), and acute interstitial pneumonia (AIP)), rare idiopathic interstitial pneumonias, namely, idiopathic lymphoid interstitial pneumonia (LIP),

and idiopathic pleuropar-enchymal fibroelastosis (PPFE), and unclassifiable idiopathic interstitial pneumonias [45].

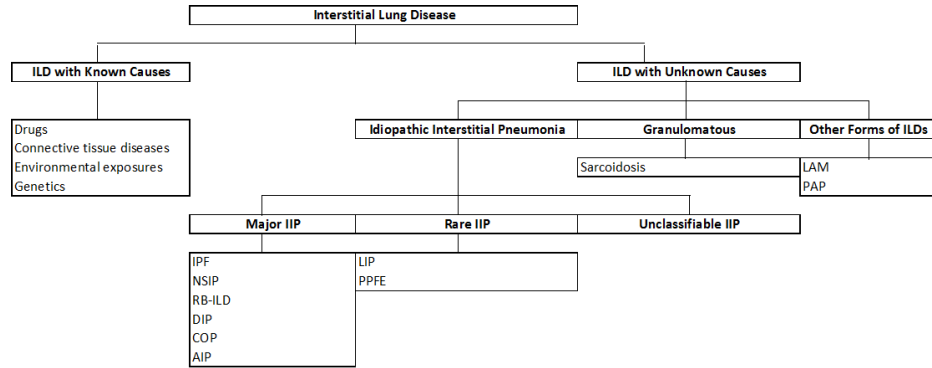


Figure 2.4: Classification of known and unknown etiologies of interstitial lung diseases (ILDs).

The multidisciplinary approach of combining clinical, radiological, and pathological data is essential in determining proper diagnosis. The radiological pattern of UIP is the most important distinction of IPF when trying to differentiate IPF from other IIP. The ability to differentiate and score the extent of disease in patients with IPF is vital for the prognosis and treatment implications in patients with IPF.

2.5 The Use of HRCT in Diagnosing IPF

For maximum spatial resolution, thin-section HRCTs are used in differentiating IPF from other IIPs. Higher resolution images increase the sharpness and detail of the appearance of the image resulting in the ability to extract more meaningful information. The anatomical position of the body is important when images are taken of the lung during diagnosis of IIP. Supine positioning often shows ground glass opacities in the dependent portion of the lung [46]; this could be attributed to the collapse or partial closure of the lung due to its positioning. The pronated position provides the optimal view of the lung when capturing

HRCT images. The prone position resolves the over expression of ground glass opacities due to the individuals positioning by removing excess force applied to the lung.

2.5.1 Defining IPF in IIPs

The initial classification of IIPs are carried out by applying exclusion criteria; after all known causes fail to be accepted further classification is defined by its radiological findings. The primary role of HRCT is aiding in of classification of IIP by distinguish UIP from other IIP diseases. IIP is generally categorized by the level of opacity; if UIP is not established a surgical lung biopsy may be required. Characteristic HRCT findings of UIP include bilateral basilar subpleural pattern of septal reticulation, with traction bronchiectasis and honeycombing Figure 2.1. When HRCT findings are not definitive for UIP other pathological features should be extracted and combined with clinical data to aid in identifying other IIPs.

2.5.2 HRCT and IPF

In order to properly diagnosis IPF exclusion of all other interstitial lung diseases, idiopathic interstitial pneumonias, and diseases associated with environmental exposures must be taken into account. HRCT findings of IPF are consistent with UIP; these characteristics gradual decline as one moves from the basilar and peripherals regions of the lobules to the center of the lobe. The hallmark feature of IPF is honeycombing, which is characterized as clusters of cystic air sacs, as seen in Figure 2.5. In HRCT images these air sacs are typically 3-10 mm wide and can sometime manifest as large as 2.5 cm [47]. Honeycomb cysts share well defined walls that frequently stack upon one another that form cyst layers [46, 48]. Reticular opacities in IPF are often coarser in patients with IPF compared to other IIPs [46] and sometime mimic honeycombing cyst. Although typically not directly associated with IPF, patchy areas of ground glass may be present in the basal and peripheral portions of the lobule. In addition to ground glass opacity, consolidation, nodules, pleural effusion,

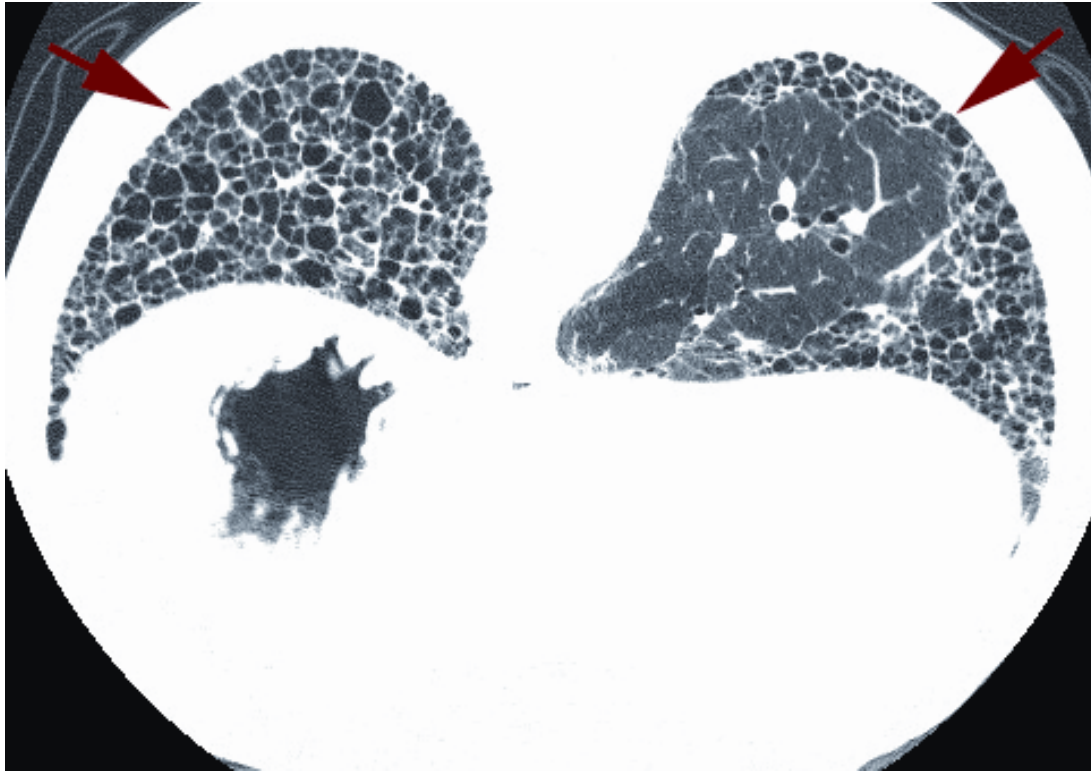


Figure 2.5: HRCT featuring the hallmark feature of IPF, honeycombing. The red arrows highlight the clusters of cystic air sacs along the basal and peripheral regions of the lung.

and lymphadenopathy are characteristics of atypical findings present on HRCT [48]. Although uncommon, these patterns do not rule out IPF, but redirect the diagnosis to other IIPs. Misdiagnosis is common in IPF with studies showing 30-40% of improper diagnosis, when non-biopsy based methods are used [49]. Repeated HRCTs aid the diagnostics and prognostic of IPF, because they accurately reflect the extent of fibrosis progression over time. Figure 2.6, shows the difference in the architecture of a normal lung verses a late stage IPF lung. Worsening of the fibrosis, which is attributed to the increase of basilar honeycombing, decreases the survival rate of patients with IPF [50, 51]. The benefit of using HRCT lies in its ability to visualize and quantify the extent of the disease. Visualization of the morphological changes aids in monitoring the development and determination of the

prognosis of the disease. Only when all other options have been exhausted, lung biopsy should be done.



(a) Normal Healthy Lung.

(b) Late Stage IPF lung.

Figure 2.6: Normal tissue architecture can be seen in image (a), where none of the radiological manifestation of IPF have set in, whereas the distortion of lung tissue due to fibrosis can be seen as in the late stage IPF image (b).

Chapter 3: Research Methodology

This study constructed a dynamic representation of the lung consisting of an elastic lattice structure. This approach helps to examine conditions under which its spatial architecture began to deteriorate and its mechanical properties started to decline. Under percolation theory, the springs of the lattice model, represented by the alveolar walls were stiffened to mimic the random onset of collagen deposition as the disease progresses in individuals with IPF. These random uncorrelated lesions mimicked connected clusters of tissue about a random graph. The locally correlated lesions were then added to replicate the deposition of ECM and tissue damage that tend to form surrounding to areas of fibrotic tissue. As these incidents increased, the spatial orientation of the lattice structure began to morph and the overall stiffness of the model began to increase until it reached a point known as the percolation threshold. At this point, the model exhibited a sharp increase in its total spring energy and a decline in its mechanical property. This study developed a multifunctional model of the lung that measured changes in the models elastics energy, and determined the percolation threshold to replicate the visual characteristics onset of early to late stage IPF to help explain why the pathological and radiological progression of IPF tends not to follow the mechanical properties associated with the disease.

3.1 Background and Significance

Percolation theory provides an understanding of how systems at the macroscopic level transition from one phase to another through the random removal of bonds at the microscopic level. That is to say, percolation is a model for structurally disordered systems [52]. Network models consist of nodes and links that are defined in Euclidean space. Such networks can be used to emulate natural processes like lung function to help describe its mechanical

properties. Therefore, combining network models and percolation theory one can aid in the understanding of why the mechanical dysfunction of lungs with IPF may follow a different course of progression from its underline pathophysiology.

The physiological characteristics of the lung are interdependent with providing the overall mechanical functionality that is expressed in lung dynamics. Physiologically, the lung is suspended in the thoracic cavity immersed by pleural fluid that provides the necessary lubrication to aid in the lung movements. Besides the pulmonary arteries that extend from the lung, the lung is physically isolated from other surrounding parts of the body by a thin layer of pleural fluid. This property of the lung allows us to model this organ independently and determine how the various parts of the lungs interstitium contribute to the overall mechanical physiology of the lung. Examining the mechanics of the alveolus, the function lies in the fact that each cell shares its walls with its neighboring alveolus. This functional relationship between the components that make up the respiratory system is often referred to as “interdependence”. Interdependence plays a critical role in maintaining parenchymal integrity, by ensuring tension in the lung is harmoniously distributed throughout the alveolar network. The coupling of alveolar walls causes stress to be generated and distributed throughout the entire lung, specifically during inhaling and exhaling; stress is generated and transferred from the organ down to the molecular level. One way pressure can be quantified is by measuring the lung stress-strain relationship. Pressure can be measured as a unit of qualifying elastic energy considerations, by examining the alveolar walls interconnections defined as its resulting lengths change per initial length. As with most biological tissue, the lung parenchyma is known for its viscoelasticity, meaning that energy, like breathing forces on the lung will be dispersed or scattered overtime as the material adjusts itself towards a state of lower global energy. Since the lung parenchyma is viscoelastic, there are viscous transformations during each breathing cycle. It is estimated that roughly 10-20% of the energy used in breathing is lost due to friction between the alveolar walls. [53] This structural damping effect is referred to as hysteresivity. Frictional energy loss and elastic energy storage are key aspects in describing lung parenchymal mechanics. Any change in the function

of the lung has a quantifiable impact on the function of those altered cells. One change is the effect of changes to the extracellular matrix of the cells. Altering the mechanical forces of the cell lead to a redistribution of how stress is managed in the parenchyma alveolar walls. This is how IPF is understood to initiate and development as an interstitial lung disease, micromechanical changes occur in the cell, which eventually lead to cell dysfunction and organ failure.

Due to interdependence of the alveoli any stress to the alveolar wall will eventually cause stress to its adjacent neighbors. For that reason, stress is normally concentrated as incident area is low, leading to more stress being placed on the area surrounding the obstructed alveoli. When degrees of fibrosis are low, fibroblastic foci are known to increase the proliferation of collagen deposition by synthesis and release of the fibrotic mediators. At this level, when the overall observed concentration of fibrosed area is low, but the clusters of fibrosis continue to proliferate, lungs continue to function normally. However, at higher density of fibrotic areas, the pathological features of IPF set in, large clusters of fibrotic tissue are observed, and mechanical dysfunction of the lung is detected. Since damage is distributed across the lung, this changes the local stress distribution in the affected areas. stress will move to areas that were not meant to bear significant stress, promoting further increase in the levels of fibrosis.

Under percolation theory, at some concentration in-between, the effects of accumulating fibrosis start manifesting. A threshold concentration must exist, where the mechanical dysfunction of the lungs tissue percolates and tips the scale from one state of the disease to the other. This threshold concentration, also known as the critical probability, is called the percolation threshold [52]. This disconnect of lung pathology and function to its clinical results are especially evident in the early stages of the progression of the disease where the physiology of the lung begin to morph, but the function remains intact. One might speculate that the gradual onset of mechanical dysfunction of the lung parenchyma is prevented by the septal patterns exhibited by the lung. However, this claim might be unfounded. Clearer understanding on how the two are linked is warranted.

The degree in which the progression of IPF varies in patients can be attributed to the variability of lung function in the individual. This is due to the difference in the underlying tissue constituents, or the differences in septal patterns organization exhibited in the lung parenchymal amongst similar patients in the same stage. Local deposition of collagen increases the regional tissue stiffness of the lung, but has shown minimal effects on the overall stiffness. Previous studies have shown [54, 55] that the total number of isolated regions of fibrosis may be a false indicator on the overall stiffness of the lung; rather, if the regions create a cross-link about the total region of the lung the spatial pattern organization can produce a critical probability where the rapid decline of overall stiffness measured by the bulk modulus can be shown. Under this assumption, the theory provides a better representation of the overall progression of the disease where the stiffness and numerical classification of the site of percolation provides a reference for the late stage rapid failure of the mechanical properties of the lung. In essence, it provides validation that the decline in lung function seems to be correlated or is attributed with disease progression, whereas in other cases there is almost no physiological change during the progression of IPF before a rapid decline in clinical performance is exhibited [56, 57]. A clinical evaluation of pulmonary function was tested in the Bois study [58] where a cohort of patients conducted various pulmonary test over a period of time. These tests provided significant clinical evidence that captured deteriorating lung function over time in IPF patients. This study provided evidence that depicted staging of the disease did not always correlate with lung function. The difference in these outcomes may suggest that the principle pathological morphology that controls the mechanical function of the lung may follow a different course of progression from its clinical outcomes.

Spatial organization of lung parenchymal has already been established to direct the diagnosis of ILDs [45]. The spatial organization of collagen deposition would, therefore, directly influence the percolation threshold. The scarring patterns seen in IPF represent a distinct class and size of clusters of lesions that manifest during disease progression. This may indicate that the development of fibrosis is not random, but occurs with a significant

degree of correlation. One possible explanation for this is that when local deposition of collagen is initiated, the local stiffness triggers increase in the levels of pro-fibrotic mediators within the surrounding area, which then stimulate production of a collagen in a positive feedback loop that give rise to locally noticeable sites of fibrosis. When negative pressure is experienced within the pleural cavity the lungs stretch and the overall stiffness of connective tissue increases until air is exhaled from the body. Any disturbance in the spatial or geographical nature of the lungs architecture typically results in the disruption of normal lung function. In IPF, this increase in tissue strain can contribute to the local positive feedback loop that aids in the fibrosis. In normal lung tissue the spatial and geographical positions of collagen and elastin protein fibers in connective tissue make it possible to carry out normal lung respiration [53]. Tissue architecture is closely related to lung function, therefore its elements and how they are arranged should wield an import influence on its physiological expression [55]. However, assuming the degree of mechanical function is based solely on the extent of tissue remodeling without understanding how the two are interrelated is unreliable. Ideally, developing a technique that would not only link the two but that would also quantify and qualify the degree of remodeling and describe how the spatial rearrangement of tissue effects its physiological characteristics would allow us to better understand the progression of IPF.

3.2 Specific Aim

The principal goal of this study is to model the relationship between the radiological features of IPF and the mechanical function of lungs. More specifically, this study aimed to model how the network models stress-bearing constituents, the alveolar walls, contribute to the changes in its mechanical properties over time. The change in in its mechanical property was determined by the change in elastic energy as its physical characteristics where altered. In this study, a 2D network system was created to represent a cross sectional model of the lung which consisted of various interdependent elements that contributed to the overall function of the model. The model measured the progress of IPF by examining the relationship

between model elasticity and pressure at the organ level. First, the 2D network system was created by mapping a diseased HRCT lung image to a Euclidean grid space by assigning each node and spring in the grid to a diseased region. Each region in the grid was assigned characteristics representative of its pathophysiological features. A probability distribution was created that is most consistent with the clinical radiological observation of the onset of fibrosis and then assigned within the grid system. Breathing was then simulated to include the macro effects of pressure. Inhaling and exhaling is critical to account for changes in alveolar mechanics by measuring how the changes in the elastic properties of respiration contribute to its underlying cellular constituents. The springs of the network model were then randomly stiffened based on these probabilities to mimic the random onset of collagen deposition as the disease progresses in individuals with IPF. The stress of the neighboring springs that accompany the initial onset of fibrosis, then trigger the local manifestation of the disease as more ECM is deposited as a response to the stress on the lung tissue represented by the springs in the network. The spring with the most stress is then stiffened to adopt the tissue damage that tends to form close to the area of fibrotic tissue. After each spring constant was increased, the system's energy was then minimized to capture the viscoelasticity of the model and to account for the change in energy as the system shifted to a higher energy state as the disease progressed. The cycle was then repeated to imitate the progressive nature of IPF to understand the early and late-stage spatial orientation of the lattice model. As these incidents increase, the lattice structure should begin to morph and the overall elastic energy, which models tissue stiffness, should begin to increase until it reaches the percolation threshold. As the model reaches the percolation threshold, there should be a sharp increase in its unit measure and its spatial arrangement should have the distinct radiological features representative of late stage IPF and mechanical dysfunction. This study builds on the prior work that examined percolation as it relates to the random fibrotic lesions as it manifests across the lung [54, 55, 59] to introduce a dynamic probabilistic representation of the lung to model trends in energy. It observes how physiological changes at the cellular level coupled with the structural level characteristics contribute to mechanical

dysfunction as expressed by its energy constitutes. Ultimately, it aims to determine why the radiological progression of IPF tends not to follow the clinical deterioration associated with the disease.

Chapter 4: Model Development

A 2D network of springs was developed to represent the cross-sectional physiology of the lung parenchyma to numerically calculate its elastic properties. The theory of the model was modeled after the study performed by Bates Et al. [54, 55, 59] which studied the bulk modulus of network models. The mechanical behavior of the lung was formulated using a 2D network consisting of linear elastic springs connected at node terminals with each spring representing an alveolar wall.

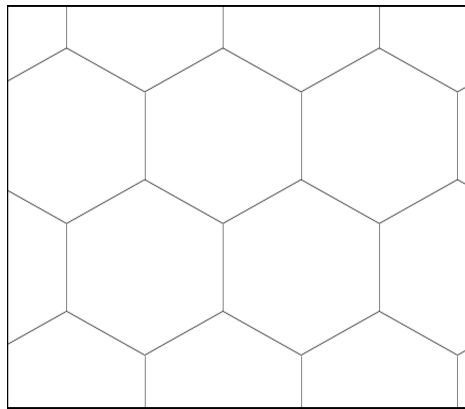
4.1 Parts of The Network Model

The model was developed using the open-source Python programming language (Python Software Foundation, Python Language Reference version 3.6) to construct the individual components of the Network. The network consists of various functions, each with its own characteristics that contributed to the overall function of the lung. The master network class consist of a Python dictionary that mapped an arbitrary sequence identifier to a node and spring class. The node sequence initialized the individual variables of the node class that held the nodes original and current location, a list of its neighboring nodes (the node sequences that are directly connected to the node class), the force of the node, its velocity and mass, and a flag that indicated if the node was movable or static. The spring sequence initialized the individual variables of the spring class which contained the springs equilibrium and its current length, its equilibrium constant, K , and a list of its neighboring springs. Both the node and spring classes inherit all the properties and methods from the network class, creating a child class that can link its individual characteristic to the overall network model. Along with the variables and methods that compose the three main classes, other supporting functions contributed to the overall function of the system. The following

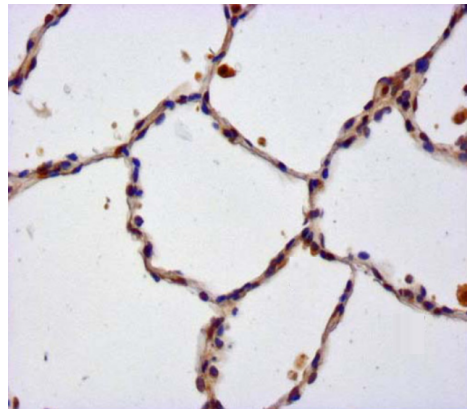
sections will go into further detail on how each method was created and how it contributed to the overall lung model.

4.1.1 Hexagonal Lattice

A vertical hexagonal lattice was created as the foundation for the pulmonary structure. Each spring in the lattice structure is meant to represent the alveolar wall, whereas each node is an anchor point that connects each spring and allows the springs to move about system. The hexagonal interior was chosen because of its resemblance to the alveolar structure of the lung parenchyma Figure 4.1. A closed network system was selected to capture the effects of pressure and mimic the physiological cross-sectional structure of the lung.



(a) Hexagon lattice structure



(b) Macroscopic image of pulmonary tissue

Figure 4.1: Note the similarities in the hexagon structure (a) and the alveolar walls (b). The macroscopic characteristics of pulmonary tissue resemble a well-defined hexagon lattice structure. Source: Sisson et al. *Adv Biosci Biotechnol.* 2012 (Figure b).

The initial structure was created by first taking the grids size s , edge length L , center of the originating hexagon (\vec{X}_c, \vec{Y}_c) , and mapping out a hex backbone that consist of the height totaling the width of the grid size. The height h of an individual hexagon is equal to $2L$. The centers of the hexagons that comprise of the grids backbone was then captured by

determining the adjacent hexes in the vertical position directly above the origination center, as seen in Figure 4.2. The vertical distance between adjacent hexes is equal to $h \cdot \frac{3}{4}i$, where i is equal to the range of 0 to the width of the grid size, by 2 (exclusively). If the width of the grid size was even, the last center value of the structure would have to be shifted by $\cos(30^\circ)$ since the formation of the backbone is staggered. After the centers of the hexes that compose of the backbone structure were established, each of the hexes corners were computed by calculating the 90° , 150° , 210° , and 270° angles adjacent to the center value

$$\begin{aligned} \vec{X}_c &= L \cdot \cos(\alpha) \\ \vec{Y}_c &= L \cdot \sin(\alpha) . \end{aligned} \tag{4.1}$$

Once the backbone was constructed each additional node that composed of the grid space was calculated by computing the width of the hexagon adjacent to the node along the backbone by $\frac{\sqrt{3}}{2} \cdot h$, as seen in Figure 4.2. This allowed for the construction of an equidistant hexagonal lattice with each side being shared by 2 hexagons and each corner being shared by 3 in the vertical orientation, as seen in Figure 4.2.

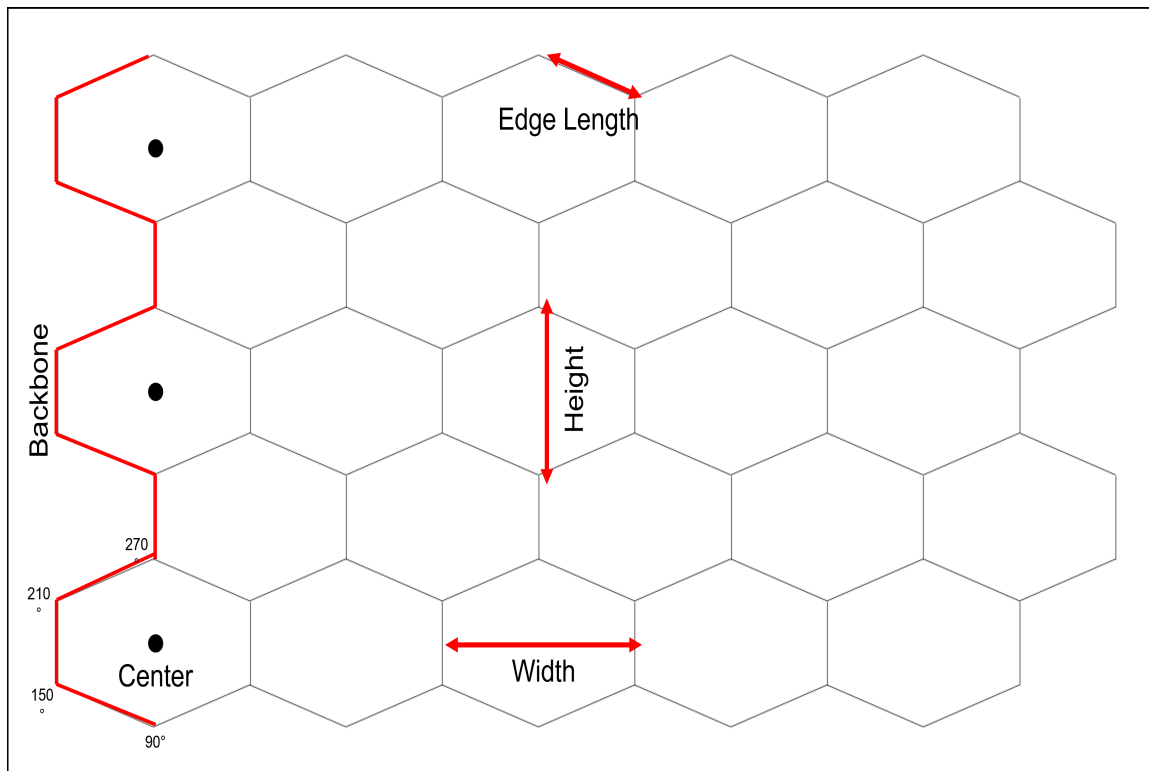


Figure 4.2: The structural properties of the hexagon structure, including the edge length, height, width, and the mapping of the hex backbone to construct the initial network.

4.1.2 IPF and Disease Regions

To develop a system model that was representative of both the lung and the onset of the disease, it was necessary to examine various HRCT images of early and late stage IPF patients to try to replicate the progression of the disease states. One methodology of constructing a 2D network that mimicked the onset of IPF was to take a hexagonal lattice, map it to a HRCT image, and define various regions that correlated with the radiological progression of the disease present in the image.

IPF Network Region Development

The 2D lung structure was developed by first selecting a pixel value from the darkest and lightest portion of the lung in a HRCT image, as seen in Figure 4.3. Once the pixel values

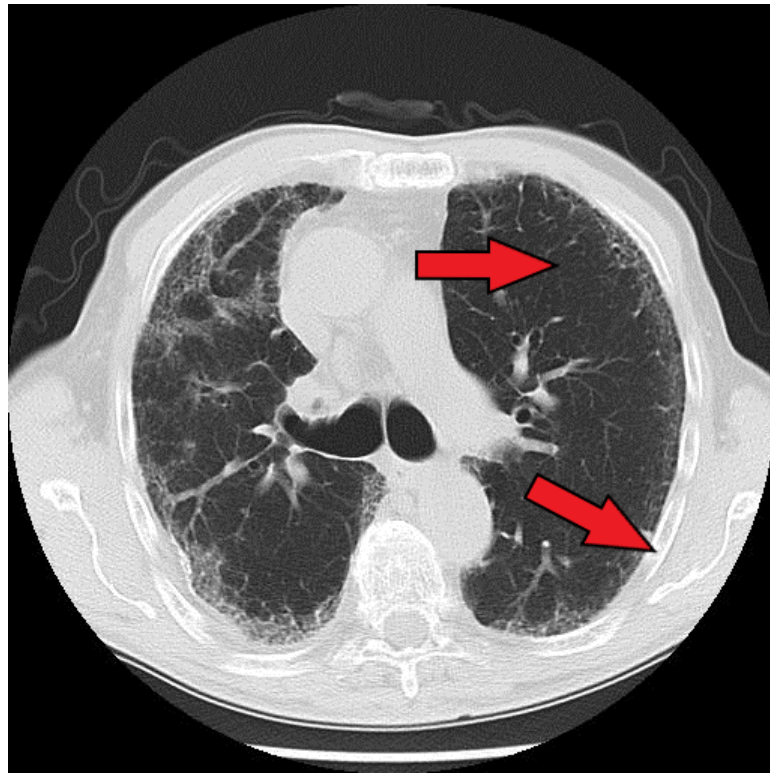


Figure 4.3: This image highlights the darkest and lightest portions of the lung used during model development to segment various structural elements.

were determined, a new image was created by filtering the color channels by the average value of the selected pixels. Since the HRCT images used in the study were in gray scale format, a Boolean image was created by selecting all the pixel values less than 145 to create a segmented image that separated the right and left lung from the rest of the image white space, as seen in Figure 4.4. From the segmented binary image, each of the unique features and objects were extracted and saved in an array. There were a total of 37 features extracted from the image with each feature representing a distinct label that highlighted

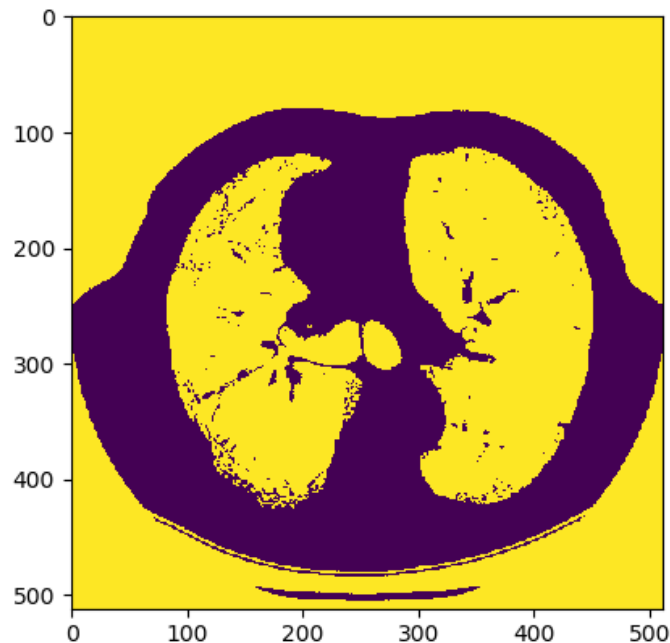


Figure 4.4: Creates a binary image where all the points less than the average pixel value, True, are highlighted in yellow and all the values greater than the pixel value, False, are highlighted in purple.

objects that were unique from the threshold value, in Figure 4.5, each color represents a unique feature extracted from the image. In this study, the right lung was selected by extracting the second label from the array of features in the segmented image. As seen in Figure 4.6, the right lung was isolated by extracting all the similar pixel values in that region. By comparing this image to the original image 4.3, you can observe that within the right lung there are a number of pixels values that fell outside the threshold boundary in the interior and the peripheral regions of the lung. These values are most representative of the attributes of traction bronchiectasis and honeycombing in IPF. Since the lung has been isolated, the missing values on the inner and outer parts of the lung could be filled with a mathematical morphology that takes the closest values around the non-featured pixels and

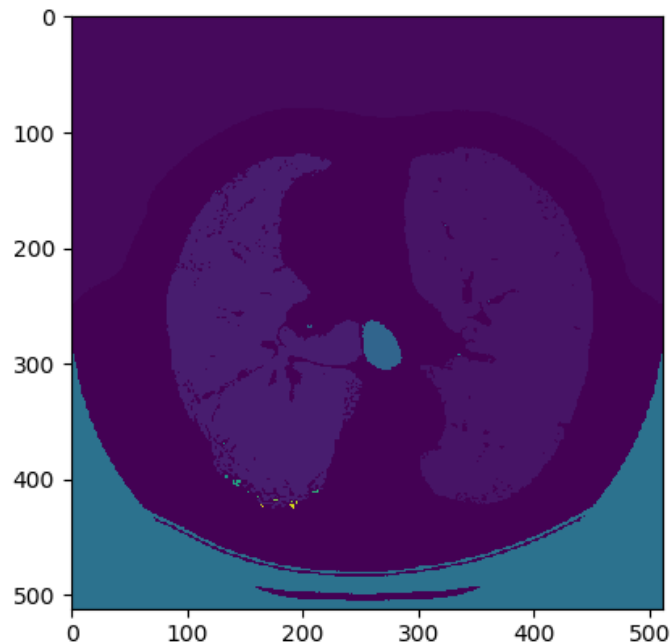


Figure 4.5: Feature extraction of HRCT model image. Each unique color represents a feature embedded in the image.

fills them in with the sounding binary values, as seen in Figure 4.7a. This process provides a smooth backbone outline of the lung that removes imperfections from the lung boundary and interior region. Next, in ordered to define distinct boundaries that represented the unique probabilities of the onset of fibrosis, a combination of binary erosions and feature extracts were used to overlay the smoothed lung with each of the distinct regions. First, a binary erosion of 5 and 20 iterations were used to create 2 unique imagines that shrunk the original image by removing the outer objects of the matrix, as seen in Figure 4.7b and 4.7c. Next, the isolated lung structure was subtracted from the smoothed lung image to extract the original unique features of IPF that were filled after the lung was isolated, Figure 4.7d. After all the regions were defined, each of the distinct regional components of the images

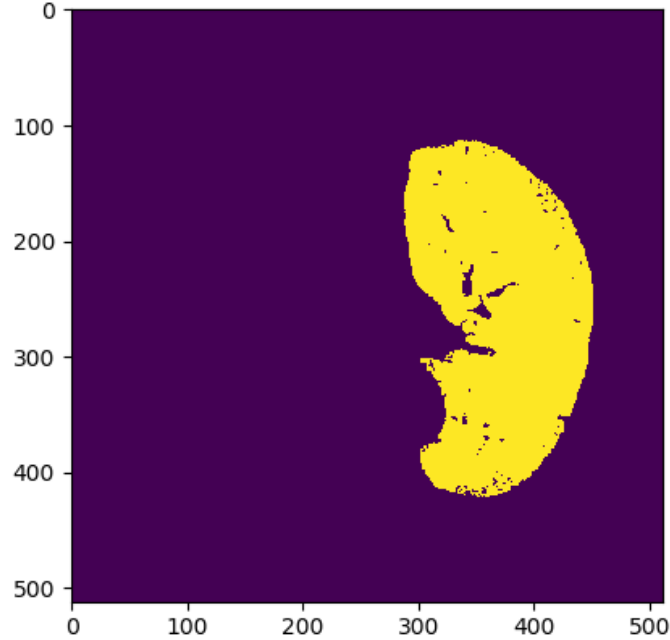
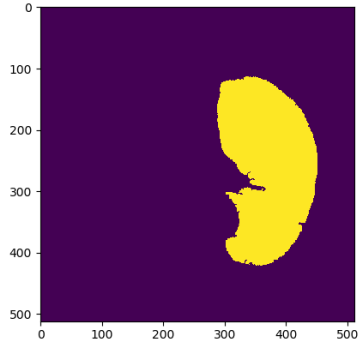


Figure 4.6: The isolated right lung after feature extraction. The right lung was separated from the rest of the embedded features by extracting similar pixel in a selected region.

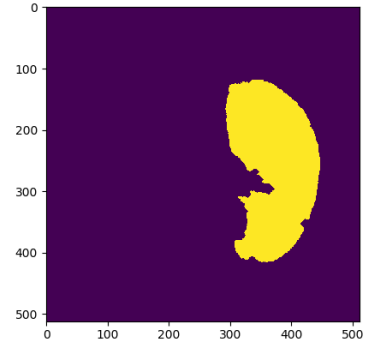
were superimposed on the smoothed lung to create a lung with 5 distinct boundaries that could be referenced and manipulated to represent the onset of the disease, as seen in Figure 4.8.

Spring Regions Assignment

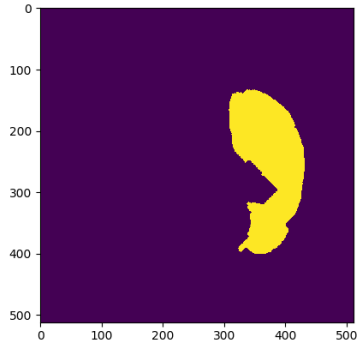
Once the model regions were developed, the network model consisting of nodes and springs were mapped to the model vector and assigned labels corresponding to their region location within the lung. This was achieved by first selecting the side of the lung of interest; in this study the right lung was selected from the HRCT model. Next, to account for the differences in sizes of the hexagonal lattice and the HRCT model, a scaling factor, SF , was



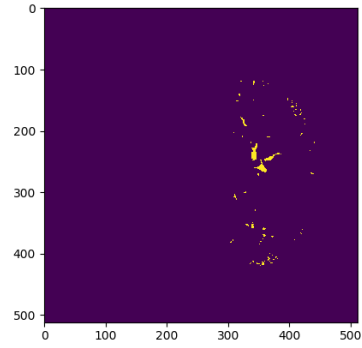
(a) Binary Fill Holes



(b) Binary Erosion 5 Iterations



(c) Binary Erosion 20 Iterations



(d) Fibrotic remnants of original IPF image

Figure 4.7: The critical image parameters used in developing the network model regions.

calculated to map the nodes of hex grid to the model space. This was calculated by taking the size of the image vector, s_{IV} , which consist of its height and width, and dividing it by size of the hexagonal lattice, s_{Hex} , which consist of the maximum value of the height and width of the hex vector

$$SF = \frac{s_{IV}}{s_{Hex}} . \quad (4.2)$$

By creating a scaling factor, it allowed the mapping of different size configurations of hexagonal lattice structures to the model space. Once the scaling factor was determined for a

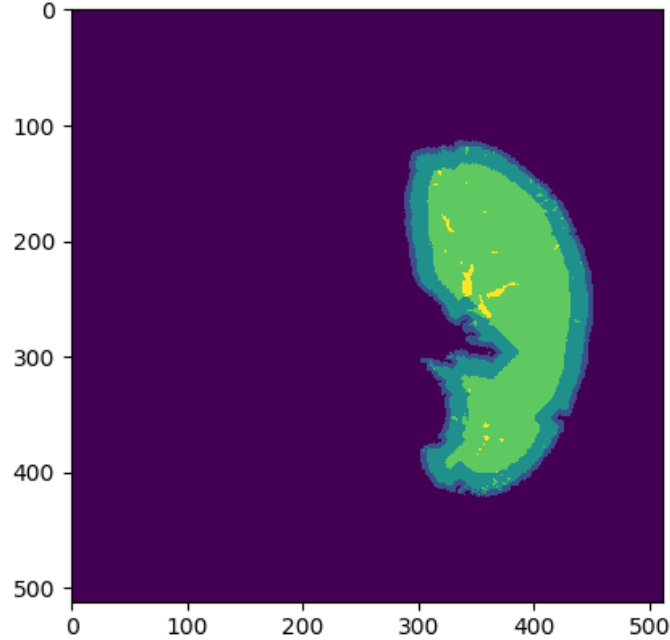


Figure 4.8: Each region is represented by a unique color that corresponds to a defined probability of collagen deposition.

particular gird size, the midpoint for each string was calculated by taking the average distance between its two nodes. Once the midpoint was determined, the scaled pixel location, SPL , the location where the midpoint maps too on the image was calculated by multiplying the spring midpoint, S_{mid} , by the scaling factor and rounding to the nearest integer, $SPL = S_{mid} * SF$. To determine the region value, the location of the scaled pixel was mapped back to the image model vector and the corresponding region was extracted, as seen in Figure 4.9. After the pixel-region transformation, all the springs that mapped outside of the lung boundary were removed from the final network model so that it wouldn't interfere with the model simulation, as seen in Figure 4.10.

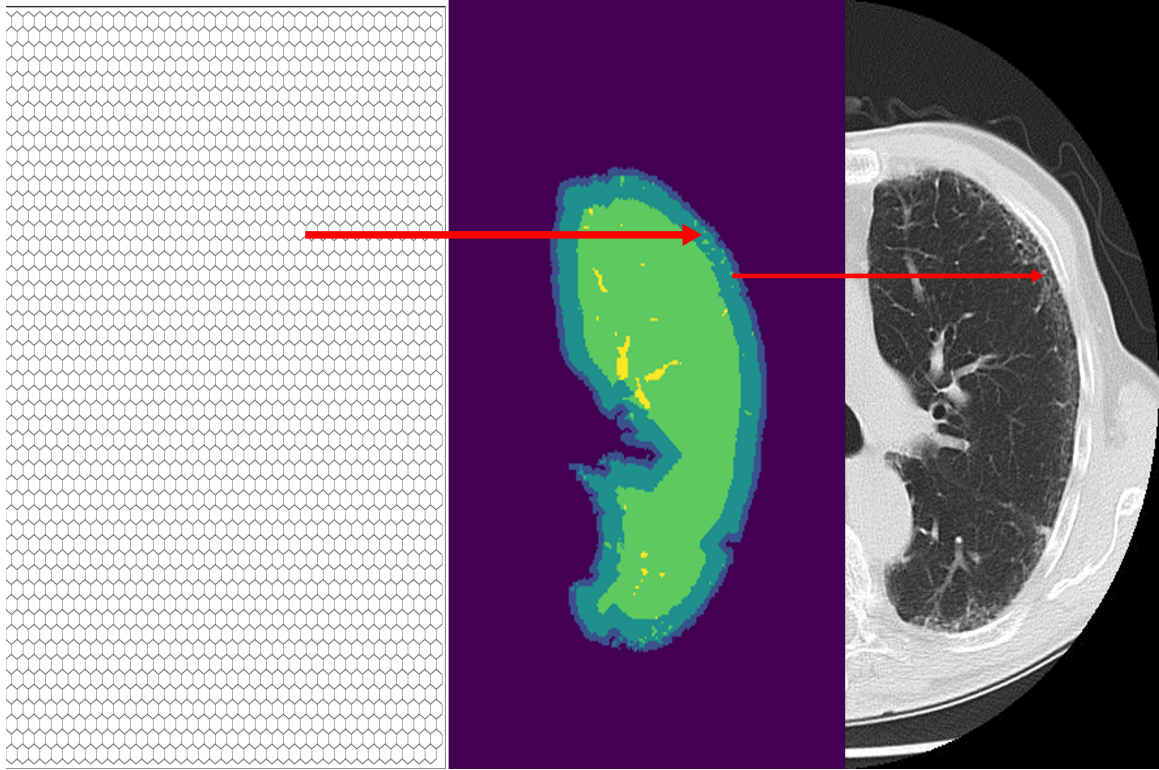


Figure 4.9: Each spring in the network was transformed by its scaling factor to map its location in the network structure to a defined boundary within the model image.

Node Assignment and Mobility

Consistent with determining the spring's locations within the model, each node's location was mapped to the lung image to determine and assign its unique characteristics to the node class. For each node, the location of its scaled pixel value was determined and assigned to the model via the pixel-region transformation. If a node fell inside the exclusion region, the node was removed from the network model. Once all the node's regions were determined a parameter was set that determined if a node was allowed to move within the network model. The mobility of the nodes was determined by first creating a network boundary of the hex network to determine the perimeter nodes. This was achieved by utilizing a built-in python function called `alphashape`, which calculates a generalized boundary of a

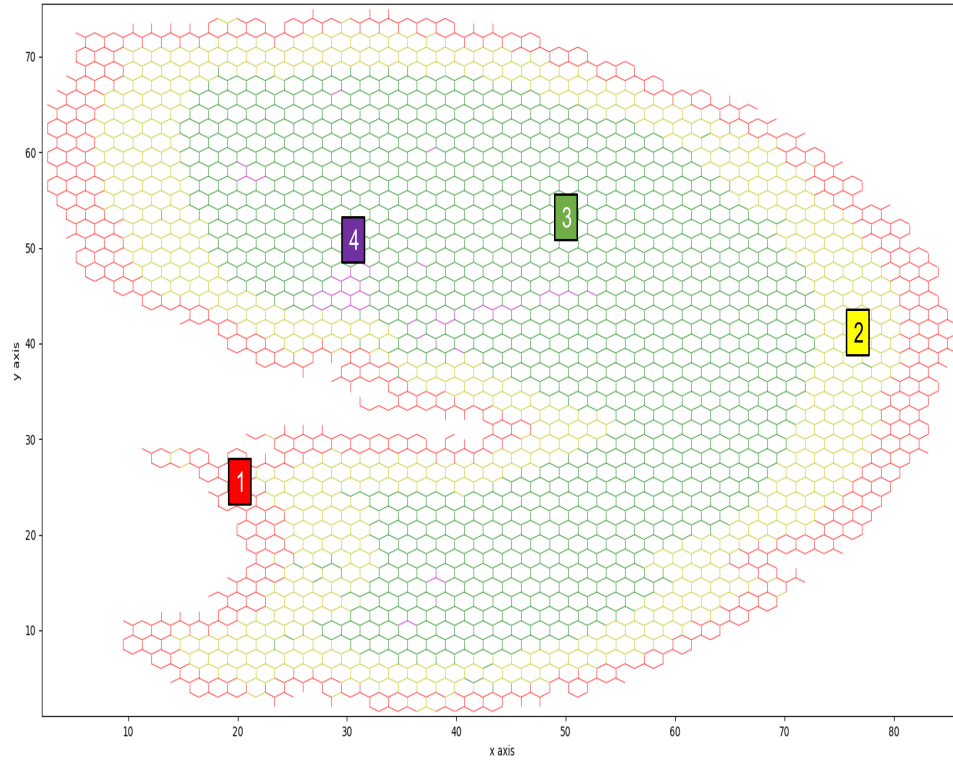


Figure 4.10: Each region in the lattice structure is represented by a unique color corresponding to its system boundary. The network model was constructed to define each region with a select probability.

polygon containing set points within a Cartesian coordinate system. Once the boundary nodes were discovered the network was fine-tuned to account for the unique shape of the lung boundary; any additional perimeter nodes were identified, and all the boundary nodes were set to immutable. The remaining nodes not in the network boundary were set to movable and could move freely within the system, as seen in Figure 4.11 The nodes that are set as immutable represent the fixed volume of the lung that remains constant during the peaks and troughs of the respiratory cycle. The closed system allows the model to mimic the transpulmonary pressure expressed in the lung and capture the alveolar morphology during its fixed volumes.

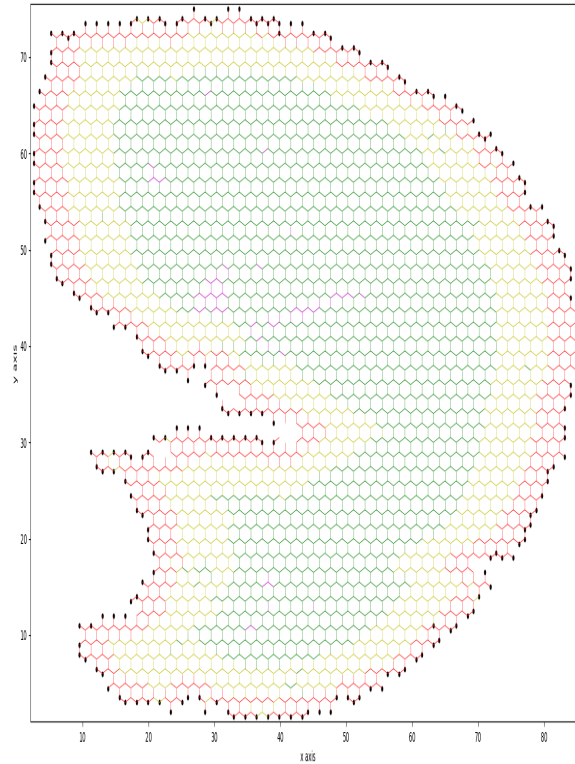


Figure 4.11: Each node highlighted in black corresponds to the lung boundary.

4.1.3 Pulmonary Ventilation

To ensure a dynamic system and to capture the mechanical properties of the lung, a respiratory cycle was added to the model to mimic the tissue and cellular processes that proceeds as ventilation occurs. In each breath, the lung expands and contracts by a certain volume to aid in the respiratory cycle. This process is achieved by Boyle's Law which is governed by the pressure-volume relationship. Lung compliance is a measure of the lungs expandability given changes to its internal pressure. Alveolar elasticity and surface tension are the main influences that contribute to lung compliance. During inhalation, the diaphragm contracts, decreasing the lungs pressure which allows air to flow inside the lungs ultimately increasing the lungs volume. During exhalation the diaphragm expands, increasing lung pressure while simultaneously decreasing the lungs cavity which forces air outside the body.

In the model, respiration was simulated by taking each node within the network, and expanding and contracting it uniformly around the lungs center of mass. The center of mass, C_m , was calculated by taking the total summation of the node's masses, m_i , multiplied by its current locations, \vec{X} , and dividing it by the total sum of all nodes mass, M ,

$$C_m = \frac{\sum_{i=1}^N m_i \cdot \vec{X}_i}{M} . \quad (4.3)$$

Once the center of mass was determined each node was moved by a fixed percentage away from and towards the center of mass in a cyclical manner. This was done by first calculating the polar R component of each node from the center of mass. R was determined by subtracting the lungs C_m from each of the nodes locations, \vec{X} , and taking the square root of the sum of squares of the vector

$$R = \sqrt{(\vec{X} - C_m)^2} . \quad (4.4)$$

To determine the new length of the vector used in pulmonary expansion, R_{Exp} , the R component was multiple by the fixed volume size, s , parameter, whereas to contract the node, R_{Con} , the R component was multiple by 1 divided by the volume size value

$$\begin{aligned} R_{Exp_{i+1}} &= R_{Exp_i} \cdot s \\ R_{Con_{i+1}} &= R_{Con_i} \cdot \frac{1}{s} , \end{aligned} \quad (4.5)$$

where R_i is the current polar length. Since the model starts from an equilibrium position, the initial expansion was only moved by half the fixed volume to establish the displacement around the equilibrium length. After the new R component was determined, the angle, θ , around the C_m was calculated by taking the arctangent of the node vector subtracted by

the C_m . This value is then used to calculate the new location of the node vector, \vec{N} ,

$$\theta_{\vec{N}} = \arctan \left(\frac{\vec{X}_y - C_{m_y}}{\vec{X}_x - C_{m_x}} \right) . \quad (4.6)$$

To convert the polar coordinates, (r, θ) , to Cartesian coordinates, (x, y) , and retrieved the updated node location, the x component of the node was calculated by taking the updated x value of the R component, R_x and multiplying it by the cosine of theta, $\cos(\theta)$, then adding the x component of the C_m , C_{m_x} . Similarly, the y component of the node was determined by taking the updated y value of the R component, R_y , and multiplying it by the sine of theta, $\sin(\theta)$, then adding the y component of the C_m , C_{m_y}

$$\begin{aligned} \vec{X}_x &= R_x \cdot \cos(\theta) + C_{m_x} \\ \vec{X}_y &= R_y \cdot \sin(\theta) + C_{m_y} . \end{aligned} \quad (4.7)$$

This method was used to ensure each node was adjusted around the center of mass in a uniform technique.

4.1.4 Force and Velocity

Movement within the network structure is dictated by the force applied to each node and its accompanying velocity. A variation of the Verlet Integration - the Velocity Verlet Algorithm, is a time dependent integration method was used to calculate the trajectories of the nodes in the network. The Verlet algorithm is used to help solve the second order differential equation of Newton's second law of motion

$$\vec{F} = m\vec{a} , \quad (4.8)$$

where F is the force exerted on a particle, m is the mass, and a is the acceleration. Acceleration can be rewritten as the change of velocity, v , over the change in time, t , $a = \frac{\Delta v}{\Delta t}$, and solving for v we obtain the expression for velocity as

$$v_{i+1} = v_i + a\Delta t , \quad (4.9)$$

which defines the first equation of motion. Since velocity v can also be expressed as the change in position over time $\bar{v} = \frac{\Delta x}{\Delta t}$ we can solve for position to get

$$x_{i+1} = x_i + \bar{v}\Delta t , \quad (4.10)$$

where \bar{v} is defined as the average velocity. Finally, applying the Merton rule and combining the equation with the velocity expression, we get the following relationship

$$x_{i+1} = x_i + v_i\Delta t + \frac{1}{2}a\Delta t^2 , \quad (4.11)$$

where we obtain the second ordered equation of motion utilizing the initial velocity and acceleration. Equation 4.10 can then be used to obtain the Velocity Verlet integration by leveraging the forward and reverse forms of the Taylor series expansion.

The force, F , of each node was calculated by adding the elastic engines of the springs acting on the node. This was performed using Hooke's law,

$$\vec{F} = k\Delta l \cdot \hat{u} , \quad (4.12)$$

which determines the elasticity of a spring defined as the amount of stretch or compression beyond the equilibrium length, Δl , multiplied by the spring constant, k . This was applied in the network model by adding the unit vector, \hat{u} , to the force equation to capture, and normalize the direction of displacement. For each the perimeter nodes, the nodes force was divided by 2 prior to adding the force on the acting node to mimic the dissipation of

energy as the nodes around the pleura space reach the thoracic wall. Since the network was modeled after the pleura space with a defined volume with nodes and springs, a molecular dynamic solution was used where the area was preserved as the various iterations of the model was allowed to proceed, therefore it was deemed appropriate to use the basis of the Verlet integration algorithm to solve the simulation. The force of each node is calculated and stored in a variable. The initial force of each node is averaged with the current force and used as the applied force when determining the nodes velocity v_{i+1}

$$v_{i+1} = \left(v_i + \frac{1}{2} (F_i/m + F_{i+1}/m) \Delta t \right) \cdot \mu , \quad (4.13)$$

where v_i is the initial velocity of the node, F_i/m and F_{i+1}/m are the nodes initial and current accelerations, Δt is the change in time, and the mass, m of the nodes was assumed to be 1g. The term μ was added to represent the friction coefficient of the system to express the dampening effect experienced by the lung as the volume changes during pulmonary ventilation. The new location of node x_{i+1} was calculated leveraging the nodes positions and accelerations with a defined time step

$$x_{i+1} = x_i + v_i \Delta t + \frac{1}{2} (F_i/m) \Delta t^2 , \quad (4.14)$$

where x_i is the initial position of the node.

4.1.5 Energy Minimization

To account for the change in energy as the system iterates from one state to the next, an energy minimization function was developed utilizing a process similar to simulated annealing that works by first allowing a subset of nodes to move about the network, then gradually allowing them to settle to a new more stable configuration. The annealing process selects the minimal energy state within the search space defined by the step size of a random set of nodes. If the new configuration after an iteration step is better than the previous

one, the previous configuration is replaced with the new configuration. However, if the new configuration is suboptimal, the new location of the nodes can sometimes be accepted with a defined probability. This process is repeated until the energy reaches a defined acceptance criteria and the systems converges to a global minimal state.

The annealing process was initialized by first defining the initial temperature for the gradient decent. The initial temperature, T_i , was determined by calculating the absolute value of the difference between the objective function of the current and candidate state of the initial step size multiplied by 100

$$T_i = |e_n - e_c| \cdot 100 , \quad (4.15)$$

where the objective function was defined as the total elastic energy, E_S , of the network configuration and it was used to provide an unbiased evaluation of current, e_c , and candidate energies, e_n . During each iteration of the model, the initial temperature was recalculated as a hyperparameter to calculate the temperature used for the acceptance probability, or metropolis acceptance criterion. To calculate the temperature variable, the model employed a method called “Fast Simulated Annealing” which was used to decrease the value of T as a function of the number of iterations, I , of the search

$$T_{i+1} = \frac{T_i}{(I + 1)} . \quad (4.16)$$

The node locations of the initial network configuration and energy were saved in a placeholder variable as the current best solution to track the optimal configuration as the function searched for the lowest energy state. Next, a step size was induced by selecting a random subset of nodes and allowing them to move about the network based on their applied forces. The objective function was then used to calculate and compare the energy of the candidate step to the current network configuration. The difference between the energies were calculated, and if the energy of the candidate state was lower than the current best solution,

then best solution was replaced with the candidate state. Next, the candidate solution was further assessed to determine how its solution would be updated in the next iteration step. The current temperature of the search was calculated, and the metropolis acceptance criteria, P_C , was determined by

$$P_C (e_c, e_n, T) = e^{-\Delta E/T} , \quad (4.17)$$

where e_c is the energy at the current state, e_n is the energy at the proposed next step, ΔE is the change in energy between the current state and candidate state, and T is the current temperature.

To define the subsequent iterations starting configuration, the candidate energy was evaluated against the current energy and the metropolis value. The solution was assessed utilizing two metrics. First, if the candidate energy was less than the current energy the candidate configuration was accepted. Second, if the candidate solution increased the energy of the system, the configuration was accepted probabilistically where the likelihood of accepting the solution was calculated based on the acceptance criterion and a random value generated between 0 and 1. If the random number was less than the metropolis criterion then the worse solution was accepted. Accepting a worse value allows the function to escape from a local minimum when the temperature is high in search for a global minimum. As the function progresses, the value of T decreases and the probability of accepting a higher value is reduced. Finally, a global energy minimization acceptance criterion was developed to determine if the network converged to a minimum energy state. After each iteration, an acceptance criterion, AC , was determined by taking the change in energy between steps divided by the candidate energy

$$AC = \frac{\Delta E}{e_n} . \quad (4.18)$$

If the candidate energy was greater than the best energy and the change in AC was less than 10^{-7} for 20 consecutive iterations the best network configuration was then set to the

current configuration and the function is considered converged.

4.2 System Iteration

The simulation of lung mechanics and the onset of IPF was conducted in a series of steps highlighted in Figure 4.12. The model was first initialized by creating a 2D hexagonal lattice

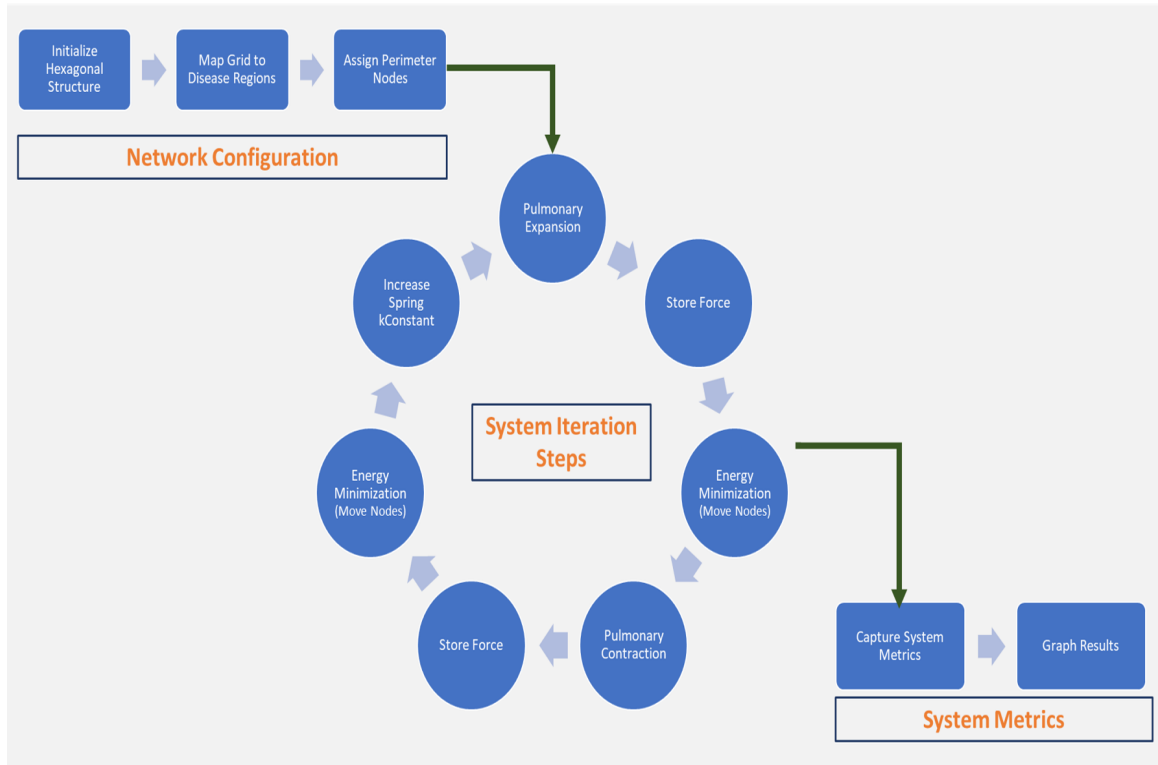


Figure 4.12: Each step in the simulation model is governed by a distinct set of rules and functions used to simulate the progression of IPF in the system.

structure and mapping the nodes and springs to an IPF image 4.9. Once the network was mapped to the image, each node and spring were assigned to distinct region corresponding to the physiological characteristics of IPF 4.10. To define the lung boundary, excess nodes and springs were removed from the network that fell outside the pleural cavity. Once the boundary and regions were established, the simulation was initialized to be homogeneous

with spring constants set to 1 AU (Arbitrary Unit) and the nodes that define the perimeter of the lung structure were held fixed. Since various nodes and springs were removed from the initial model, each of the springs and node neighbors variables in the network was updated to capture the changes in subclass. To simulate pulmonary respiration under normal resting conditions, the nodes within the network were allowed to expand and contract by a set value above and below the baseline network configuration. After expansion and contraction, the nodes in the outer most region were fixed to represent the maximum and minimum volumes of the lung. This was performed to capture the intrapulmonary pressure experienced by the lung under normal conditions, and to vary the stress-strain relationship of the springs within the network system. As in Bates Et al. [54, 55, 59], the initial elastic spring constant and the unstressed spring lengths were identical to represent the baseline network configuration. Fibrosis was then simulated by applying a two-rule classification system where each rule was initialized in step-wise fashion.

Rule 1 - Percolation: a spring is chosen at random and stiffened by a factor of 100 given a probability distribution of the expected region of initial collagen deposition.

Rule 2 – Strain dependent random walk: a spring is chosen by calculating the maximum strain exerted by the neighboring springs stiffened in Rule 1. The spring was then stiffened by a factor of 100 and extended by $N - 1$ times. If the spring was already increased, a random spring neighbor was selected.

After each expansion or contraction, the outer nodes were held fixed and rules 1 and 2 were applied followed by applying a energy minimization function to minimize the energy that was added to the system by increasing the springs k constant. Each application of the minimization function was to return the system to a global minimum energy state. After each iteration, the Total Energy (E_T), Total Node Energy (E_N), and Total Spring Energy (E_S) of the network were calculated. This sequence of events was repeated until all the springs in the network were stiffened. The total Spring Energy, or elastic energy of the network was used to describe lung compliance and capture how the change in volume of

each iteration coupled with the increase of k contributed to the change in elastic properties of the network. The total node energy tracked the ability of the individual springs, or alveolar walls to move as the disease progressed. The E_T was calculated to monitor the state of the overall system. Rule 1 of the model represents percolation theory, where the system is trying to extract the percolation threshold from one state to another. Rule 2 represents the local deposition of collagen seen in neighboring fibers in IPF. This allows the springs from Rule 1 to initialize the site of spring stiffness and for $N \gg 1$, seed the path of local stiffness. When $N = 1$, Rule 2 no longer applies because no extension beyond the initial random site is allowed to change; only Rule 1 applies, and the percolation threshold is achieved independent of local stiffness. Since the application of Rule 2 creates local clusters based on the maximum strain of its neighboring spring, a spring may be visited more than once in the determination of the strain dependent random walk although springs are only allowed to increase their stiffness once. This method results in local cluster sizes less than or equal to N springs. With the assignment of static disease regions, each incident is localized to regions with pathological characteristics that force onset to occur in a probabilistic manner.

The initial configuration of the simulation was setup by inputting the magnitude of oscillation for the network boundary. During each cycle, the nodes were stretched and compressed uniformly by 5% of the baseline configuration. At the peaks and troughs of the cycles, the border nodes were held fixed to represent the lungs tidal volume. The degree of ventilation was chosen to replicate the anatomic disposition of the lung as it oscillates during each cycle. Pulmonary tidal volume equates to approximately 10% of the total lung capacity, or 500 mL [60] and it can be used as a reliable measure in replicating normal pulmonary mechanics.

To replicate the onset of fibrosis and differentiate the regions of the lungs that correlated to the radiological characteristics of IPF, each region was assigned a probability that represented the likelihood of collagen deposition as the disease progressed. The regions of probability were set up to represent the characteristic HRCT findings of IPF, which include

bilateral basilar subpleural pattern of septal reticulation with traction bronchiectasis and honeycombing. In addition to its basilar orientation, IPF is pronounced in the peripheral portions of the lungs and diminishes as it migrates to the medial portion of the lung. As such, the model regions were set up as a gradient system where the likelihood of selecting a random spring from the network was greatest in the inferior portions of the network and decreased as you moved towards the center of the lung. Once a spring was selected and its k constant increased, the strain, S , of each of its neighboring springs was then calculated by $|\Delta L|/EquLen$, where ΔL was the change in length beyond the equilibrium length divided by the equilibrium length, $EquLen$, of the spring. Following spring selection, a strain dependent random walk of $N - 1$ was selected and the neighboring springs with the greatest amount of strain were stiffened by a factor of 100 AU to represent the local clustering of fibrosis. Once the springs were stiffened, the nodes are allowed to move a small distance in the direction of the applied force during the energy minimization step to account for the step size when the exterior nodes were held fixed in both the expanded and contracted positions. As stated above in section 4.1.5, after each iteration the system was tested to see if the network converged to a minimal energy state. The ΔE of the current and candidate state of the network was computed; if the energy difference in the new state was lower than that of the previous state, the new network configuration was accepted. This process was repeated until the acceptance criteria of the minimization function was met, which was defined as $\Delta E/e_n$ remaining below 10^{-7} for 20 consecutive iterations. After the system converged to a minimum energy state, the total energy of the network was calculated as the sum of the spring and node energies

$$E_T = \sum_{i=1}^{Max} e_{s_i} + e_{n_i} . \quad (4.19)$$

The spring energy, e_s , also known as elastic or potential energy was calculated as half the product of the spring constant multiplied by the square of their displacement $\frac{1}{2}k\Delta l^2$,

and the node energy, e_n , or the kinetic energy of the system, was calculated as half the product of the node mass multiplied by the square of its velocity $\frac{1}{2}mv^2$. This process was repeated until all the springs inside the network system were stiffed. Once the simulation was complete, each of the model iterations and parameters were examined to identify how and if they correlated with early and late-stage characteristic progress of IPF.

Chapter 5: Model Validation

To ensure accuracy and reliability of the pulmonary model each validation process was designed to discern improper behaviors in the designed functions. For each function, a set of defined requirements and parameters were developed to mimic the biophysiological aspects of IPF. A stepwise approach was taken to validate each of the functions of the model. As pieces of the function were verified, additional levels of complexity were added to the system and tested to confirm its validity. These functions were designed and evolved over several iterations to the final version seen in the system model. Each function was validated to maximize effectiveness to assure their computational solutions align with its mathematical properties and carry out their designed functionality in a reproducible manner.

5.1 Force and Velocity

To verify the code utilized for the force and velocity equations a single hexagon structure was constructed and its computational properties were examined. The force and velocity solutions were compared utilizing its theoretical and analytical derived solutions to its computational metrics. Each of the parameters in the model function were used to replicate the individual mechanics that contributed to the overall network model. To begin, a single hexagon was initialized where all the springs had the same lengths and k constants in its equilibrium configuration. This created an initial configuration where the nodes possessed no net force or velocity. Next, a single node was selected at the topmost vertical position of the hex structure with the greatest y-value. Its position was updated so its new y coordinate was 1.25 times greater than its equilibrium value. This created a new net force on the node by stretching the two adjacent springs beyond their equilibrium lengths. The node was allowed to move in the direction of the applied force for a set number of iterations, and the

location of the node was tracked as seen in Figure 5.1. As noted in Hooke’s law, force is directional proportional to the change in length of the spring. By elongating the springs

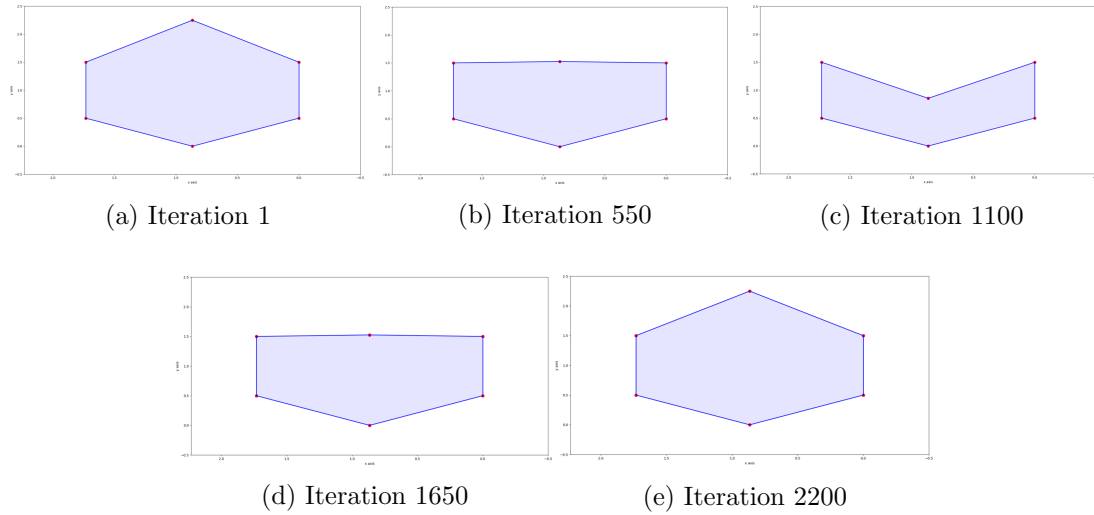


Figure 5.1: Snapshots of the iterations of the adjusted node about the system to validate the force and velocity definitions. The node was allowed to move in the direction of the applied force.

length a new net force was applied to the network. To confirm the computation solution, an analytical derived solution of the applied force and velocity acting upon the node was manually computed where all five neighboring nodes in the network were held constant. A single node was isolated so the energy could be tracked and the force of the node acting on the structure could be computed. After the force was calculated, the node’s velocity was computed from the derived force so that the Spring and Node energies could be calculated to confirm both the acting force and velocity of the system by analyzing the networks total energy. As seen in Figure 5.2, the systems total energy for a single iteration was analytically calculated and possessed an error rate of $-4.84E-08\%$ from its computational solution. This slight difference can be attributed to rounding errors from the two solution methodologies. Furthermore, the conservation of energy and momentum of the nodes were tested. A network validation test of 5000 iterations was perform where a single node was

Function	Grid Size	kConstant	Analytical Solution: Total Energy (TE)	Computational Solution: Total Energy (TE)	Error %
Force and Velocity	1x1	1	0.021	0.021	-4.84E-08
	3x3	1	0.052	0.052	-1.61E-09
kConstant	1x1	100	1.071	1.071	-5.79E-08
	3x3	10	0.148	0.148	-1.44E-09

Figure 5.2: For the selected model functions, an analytical solution was computed and compared to its computational derived solution. Error was calculated as $100 * (Computational - Analytical) / Analytical$

moved and the acting force allowed the node to move about the grid space. It was observed that ignoring any energy damping parameters and keeping the neighboring nodes fixed, the E_T of the system was conserved, Figure 5.3. As seen in Figure 5.3, the E_N and E_S of the network oscillated harmoniously with every iteration. This should continue until a new net force is applied to the network. For each iteration in the validation simulation, the center of mass was calculated to map the weighted distribution of the position of nodes within the system as the node was allowed to move about the network. This was done to validate that the node moved along a known path, and confirm the nodes that were help constant were indeed stationary. This also helped to verify there was no unexpected movement in the nodes X, and Y position over a given iteration as the model is allowed to progress. As seen in Figure 5.3 the observation of the cyclical shift in the Y-value of the C_m , and the stationary position of the X-positions as the system progress confirms the not only the initial displacement of the top node in the Y direction, but also the calculations for the Force and Velocities of the computational model.

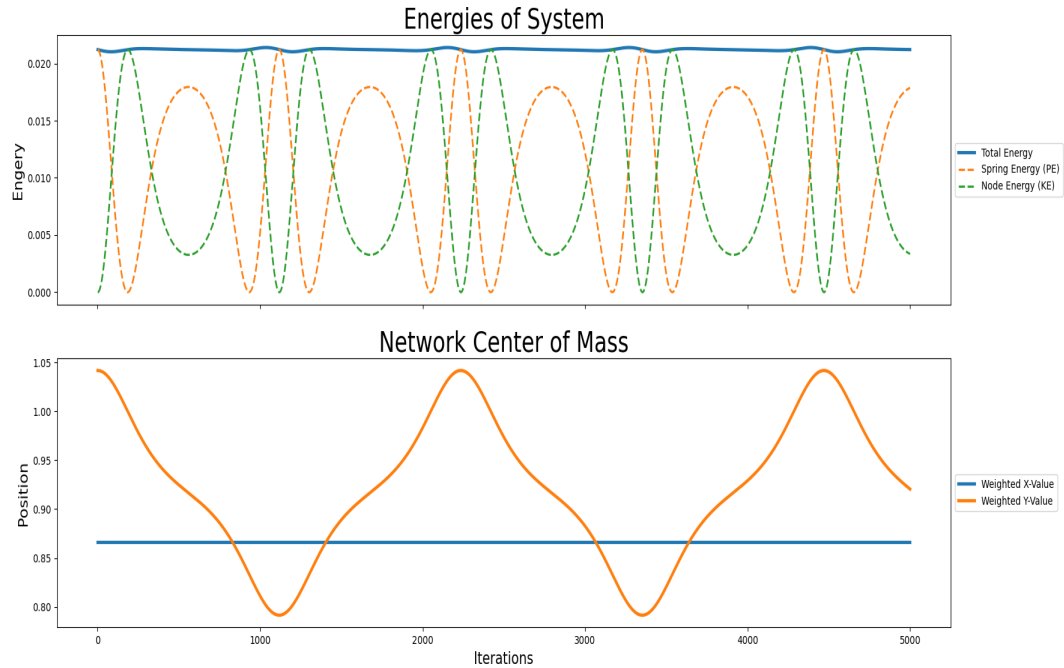


Figure 5.3: The conservation of energy coupled with the oscillation of the spring and node energies, and the defined progression of the center of mass to confirm the systems computational properties when applying the derived the force and velocity definitions.

5.2 k Constant

After each iteration of the model simulation, the k constant was increased by $N - 1$ to simulate the onset of fibrous in a localized region and to capture the stiffening of the Alveolar walls represented by each spring in the network model. To validate the mathematics of increasing the k constant in the computational model, an analytical solution was derived from increasing the k constant of a single spring while the node was free to move on the force applied to the attached node. The error metric, the difference in total energy between the analytical and computational solution was computed and evaluated as seen in Figure 5.2. An error rate of $-5.79E-08\%$ for a single iteration was derived from the computational

solution.

In the initial configuration of the validation, the springs k constants and lengths were set equal to 1. Holding the springs in the network static, the k constant of the spring connected to the top left side of the movable node was increased by a factor of 100. After the spring was increased the node was updated so that its new y -value was 1.25 times greater than its equilibrium value, and as in section 5.1 was allowed to move in the direction of the forces acting on the node. As seen in Figure 5.4a, increasing the spring constant caused the node to move in the direction of the stiffed spring as the spring contracted, resting expansion in search of return to its equilibrium length of 1. Next, the k constant was decreased to a value of 0.01 to validate the effects of the spring constant metric on the system. Decreasing the k constant below the equilibrium concentration had the opposite effect on the node, increasing the level of compliance in the direction of the spring with the higher k value, the top right spring neighbor as seen in Figure 5.4b. However, this happened at a much slower rate since the force acting on the node decreases as the value of the k constant decreases. As the total number of stiff springs in the system increase, the springs with the higher k value will possess a higher acting force on the node as the springs try to return to a lower energy, or it's equilibrium length.

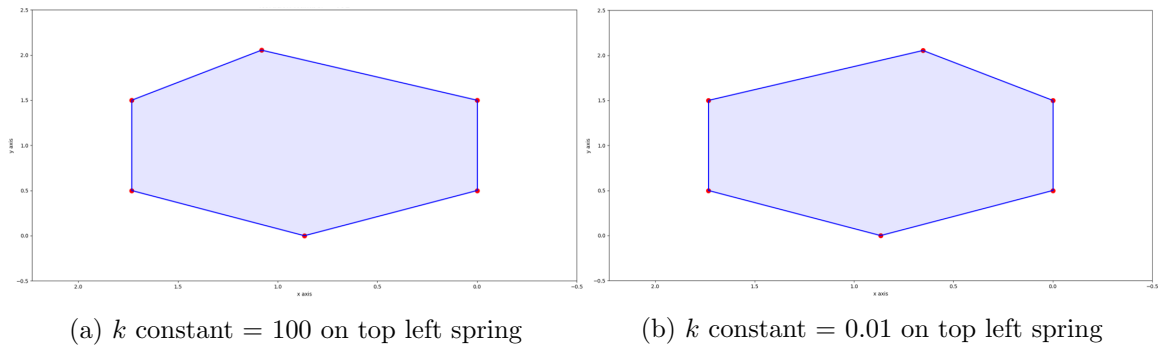


Figure 5.4: Validation of the effects of adjusting the spring constants on the top left spring. Figure (a) depicts how increasing the spring constant returns the spring to its equilibrium length, whereas Figure (b) shows how decreasing the spring shifts the resistance to the spring possessing the higher k .

5.3 Multi-Hexagon Validation

The goal of the study was to increase the level of complexity of the model by adding dynamic functions to computationally capture characteristics of the lung and its alveolar mechanics to ultimately explain the biological behavior of individuals with IPF. Once the computational model of a single hexagon was validated, the system was expanded by increasing its network size to introduce additional functionality to measure the impact of these components on the pulmonary model. The force and velocities of the expanded network were validated by applying a similar methodology as the single hexagon system. To validate the enlarged network a 3 by 3 hex system was created which consisted of a total of 30 nodes and 38 springs. All the exterior nodes of the network were held fixed and the interior nodes were allowed to move a small distance in the direction of the applied force, Figure 5.5. Each of the nodes forces and energies were tracked and used to confirm the computational mode as seen in Figure 5.2. To validate the consistency of the equations over a series of iterations, the networks total energy, E_T was calculated and observed in Figure 5.6 for a total of 1000 iterations. As observed in the Figure 5.6, without any additional forces applied to

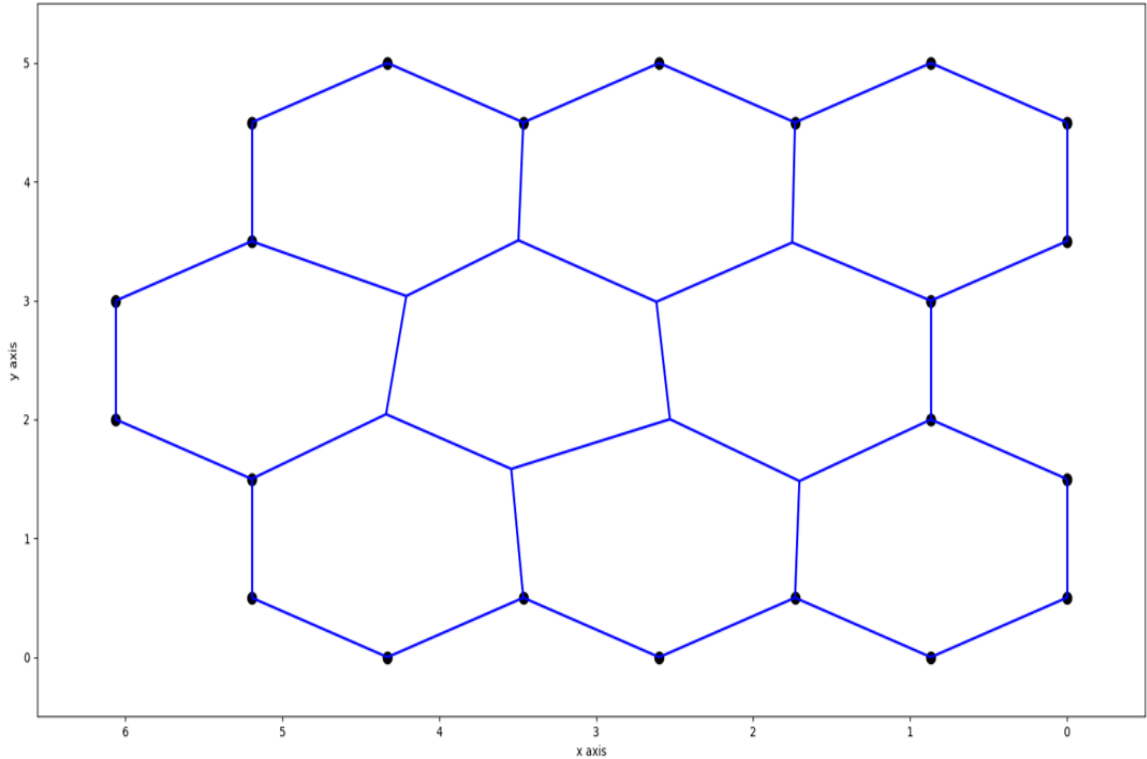


Figure 5.5: Grid space of a 3 by 3 hexagon network used to validate a multi-hex system. The perimeter nodes are highlighted in black, and the interior nodes were allow to move about the network.

the network, the kinetic energy was transformed to elastic potential energy as the system maintained a constant total energy, as the energy was conserved in the closed system.

Similarly to the force and velocities, increasing a k constant of a spring was validated by tracking the E_T over set number of iterations. According to Hooke's law, increasing the spring constant, k of a spring will cause the magnitude of the force to increase in the direction of the applied vector. The rise in force sequentially increases the total energy of the system by magnifying the elastic energy of the network. As seen in Figure 5.7, after the first 500 iteration, the k constant of a single spring was increased by a value of 10 and proceeded for an additional 500 iterations. As observed in the graph, the E_T of the system increase by a factor of 2 representing the distinct energy contribution of increasing the

elastic constant of the spring in the network.

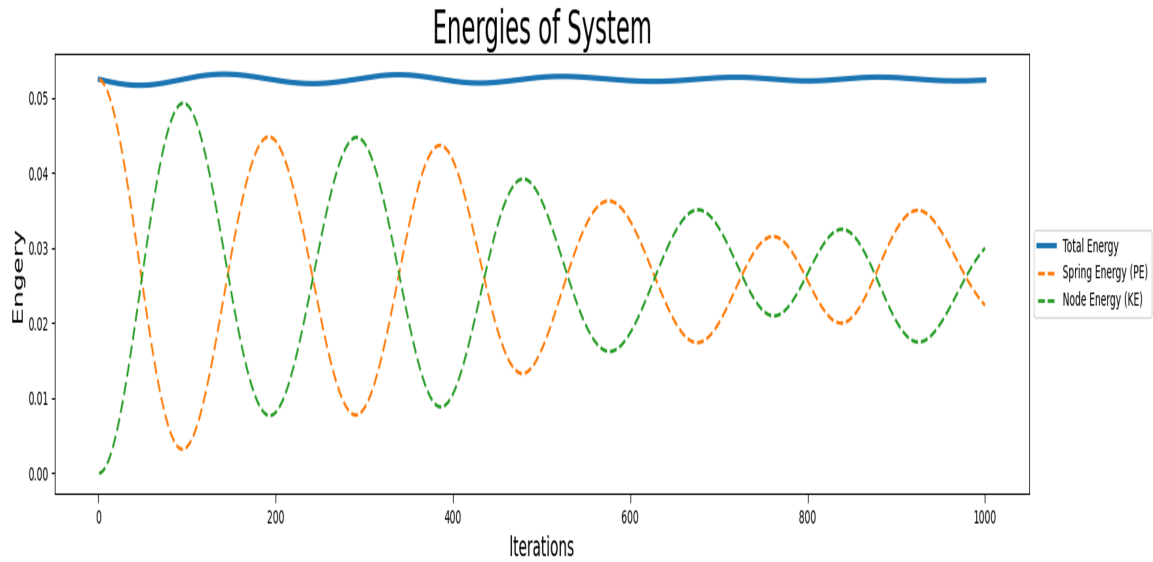


Figure 5.6: The computational metrics for a multi-hex network was verified by maintaining a constant E_T for 1000 iterations as the internal nodes were allowed to move about the network.

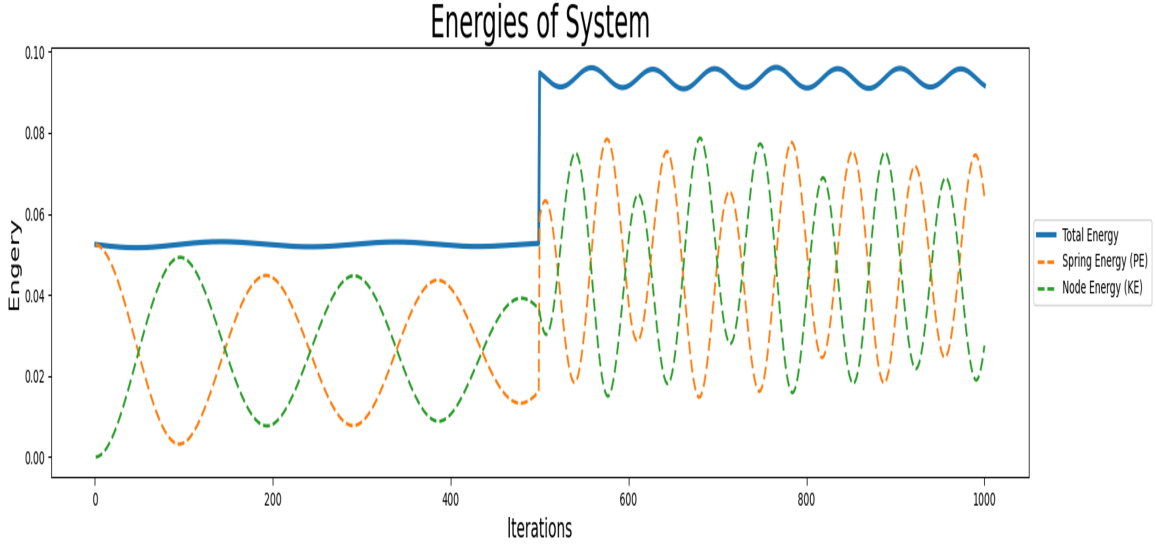


Figure 5.7: After 500 iterations the k constant was increased to validate its computational metrics. Increasing the k constant increased the E_T of the system by increasing the E_S of the network, as seen in the graph.

5.3.1 Pulmonary Ventilation

Pulmonary ventilation is the physiological process of providing oxygen and removing waste from the body. There are various biological and mechanical properties required to execute this process. This model focused on implementing the mechanical characteristics most associated with the expansion and contraction of the pulmonary tissue to model how its physical properties contribute to the progression of IPF. After validating the model of a single and multi-hexagon system, the pulmonary ventilation function was analyzed for the network model. Prior to validating the ventilation function, the center of mass, C_m was validated by manually calculating the center of mass of a single hexagon structure and comparing it to the computational value. To begin, a single hexagon was created with its center point originating at (1,1). Next, the center of mass was manually and computationally calculated by taking the node's masses and multiplying it by their current locations and dividing it by the total sum of all nodes, as seen in section 4.1.3. The C_m

for both the manual and computational calculated values for the single hex structure was (1,1), as expected from its origination position. To initialize the pulmonary ventilation model, a 25 by 25 hexagonal network was created by mapping the grid space to a simple lung image to represent the respiratory area of the simulation model. A simple network was defined as a grid space where all the interior springs possessed the same region value. The simple network model consisted of a total of 867 nodes and 1238 springs, which were initialized to have no net force and an equilibrium spring length of 1. Next, the C_m of the network was calculated, and all the nodes were expanded and contracted to achieve a total displacement of 50% in the x and y directions around its center of mass value of (21.92,19.86), as seen in Figure 5.8. The validation model used this particular displacement

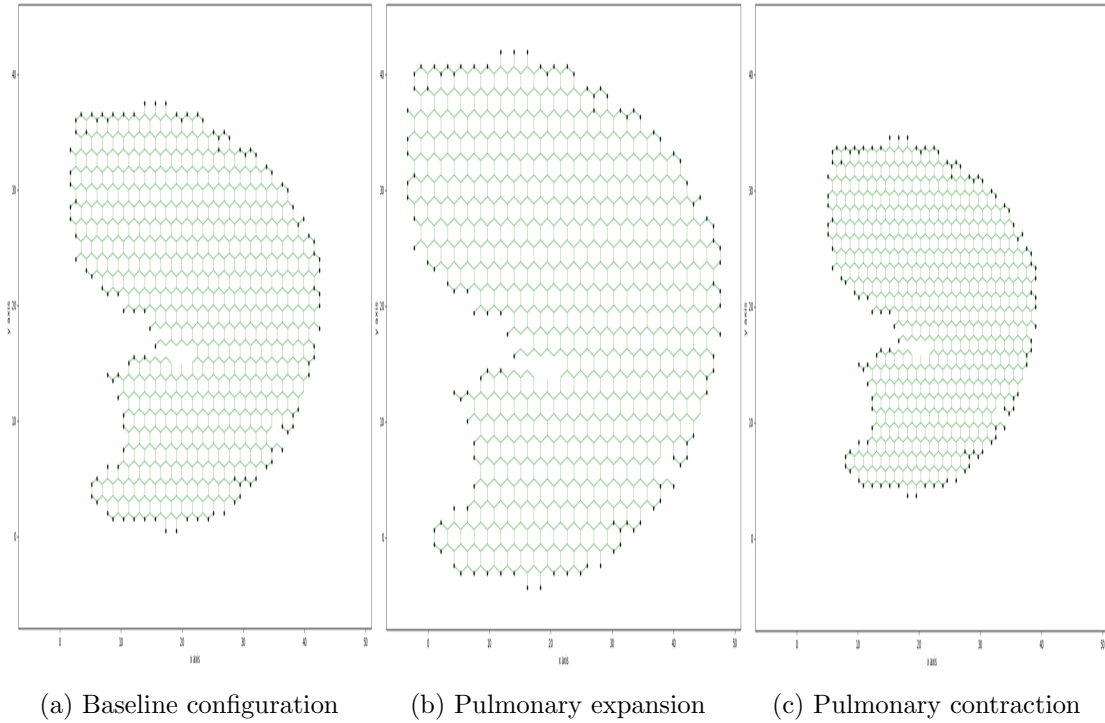


Figure 5.8: Cross sectional depictions of the baseline (a), expanded (b), and contracted (c) network configurations around the center of mass used to validate the pulmonary ventilation functions.

factor to exaggerate the physiological parameters of the lung to capture the visual effects of expansion and contraction of the network from its initial configuration, and to track the networks center of mass over a set number of iterations. Figure 5.9, shows how the center of mass remained constant in conjunction with the calculated center of mass for each iteration of the simulation, confirming both the expansion and contraction computational functions utilized in the pulmonary ventilation model.

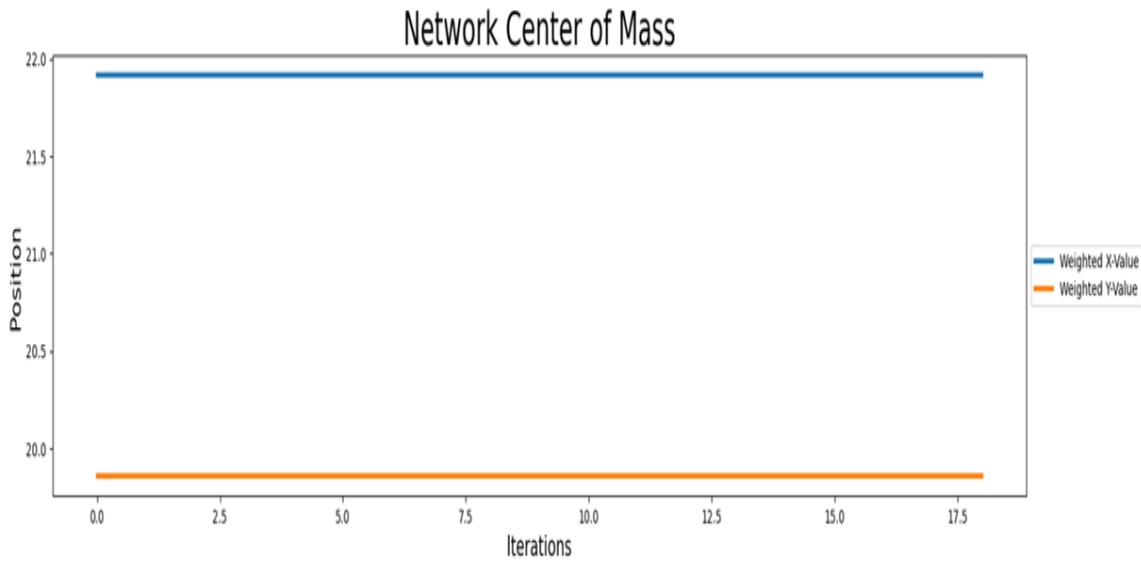


Figure 5.9: Highlights a constant center of mass over a set number of iterations as the lattice structure expands and contracts, to validate the pulmonary ventilation function.

5.3.2 Energy Minimization

At the conclusion of each iteration of the model, the k constant was increased which pumped energy into the system. To combat this, a variety of physiological mechanisms were added to the model to mimic the biological properties of energy dissipation enacted by the lung to mitigate the issue. However, as the disease progressed with each iteration, the system demanded a more efficient methodology to offset the high energy. Thus, a gradient decent

methodology called simulated annealing was utilized which allowed the network to settle to a minimum energy state. To confirm the computational approach of the function, the length of a single spring was stretched beyond its equilibrium position and the change of energy was captured as the network rearranged itself to a lower energy state. As seen in Figure 5.10, the initial energy of the system was high due to the artificial energy injected into the model by stretching the spring beyond its equilibrium position. As the annealing process progressed, the network quickly adjusted itself to a lower energy state as it altered its configuration along the search space. As observed in the graph, it took about 3500 iterations until the function started to plateau along the energy minimum as the global solution was found. This process was conducted in both the expanded and contracted states after the pulmonary ventilation functions were applied. Once the acceptance criteria was met the function was said to have converged and the process repeated until all the springs in the network were increased.

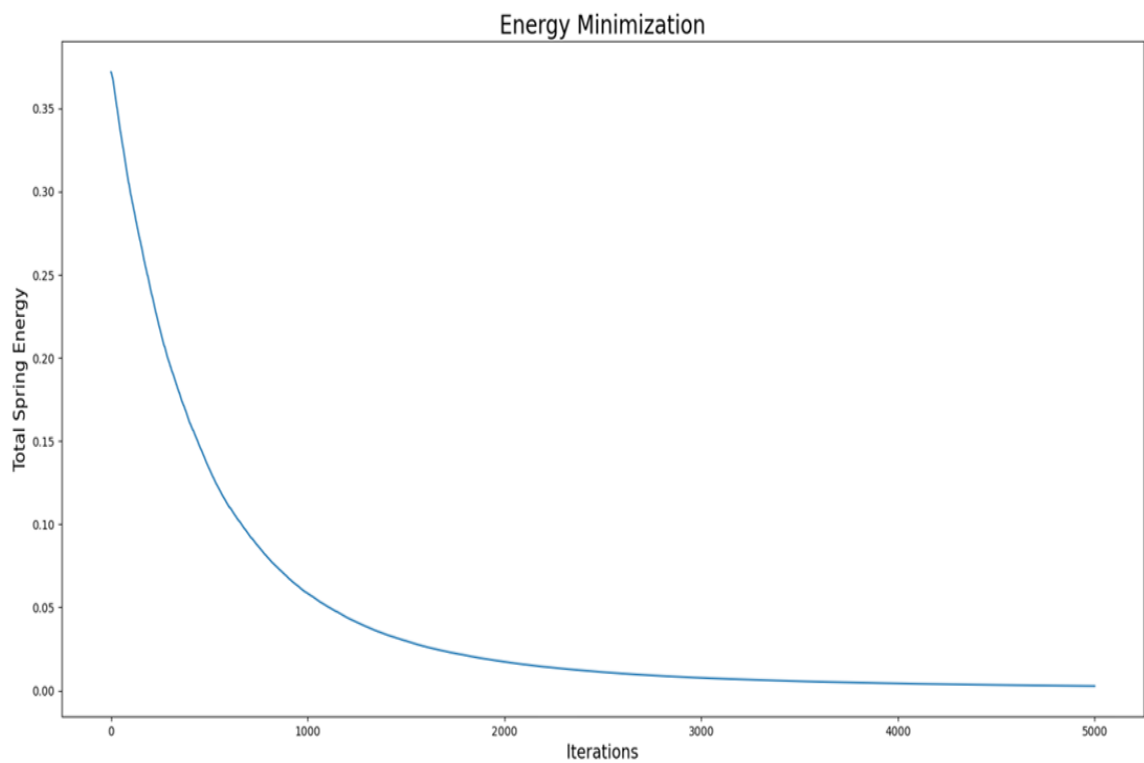


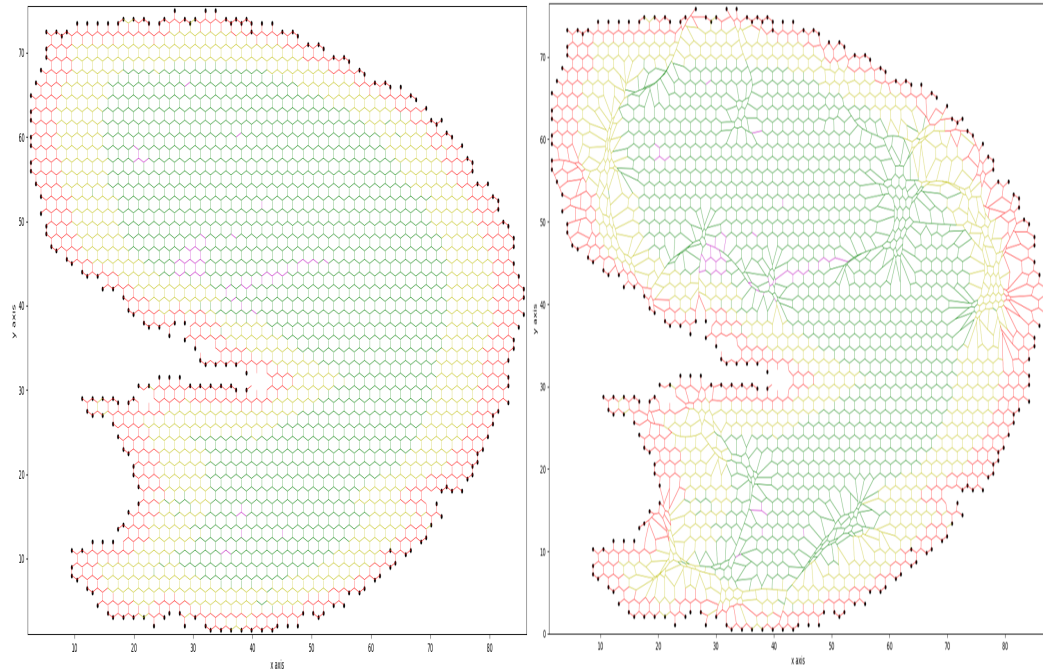
Figure 5.10: Displays the decrease in the networks spring energy as the energy minimization function searches for a global minimum.

Chapter 6: Model Results

A 50x50 2D network structure was initially constructed and transformed to represent a cross sectional image of an IPF HRCT. The final network consisted of 3436 nodes and 5011 springs, after each node and spring in the model were manipulated and assigned regions values. Each region was constructed to represent the distinct probability of the onset of fibrosis initiating in the alveolar interstitium. Regions 1,2,3 and 4 were assigned the probabilities of .60, .24, .01, and .15, respectively, and a single spring was selected at random to determine the initiation point of fibrosis. To mimic the onset fibrosis in IPF, each spring k constant was increase by a factor of 100. Regional deposition of collagen was created by taking a value of $N > 1$, which defined the strain dependent random walk and increasing its k constant in conjunction with the starting point. To adjust the degree of the disease state, the equilibrium length of the springs was altered at the start of the model simulation below the baseline configuration. The baseline configuration of the network was set with a springs lengths and k constant of 1 AU. The elastics properties of the network model were defined by the alveolar walls, which were characterized by springs connected to nodes about the network structure. The edge nodes were held fixed and created a boundary that defined the area of the lung. Each node was expanded and contracted around the networks center of mass to mimic pulmonary ventilation, and after each iteration the nodes were allowed to move in the direction of their applied force and a new equilibrium configuration was determined by minimizing the total spring energy of the system. This was repeated until all the springs k constants were increased in the network model.

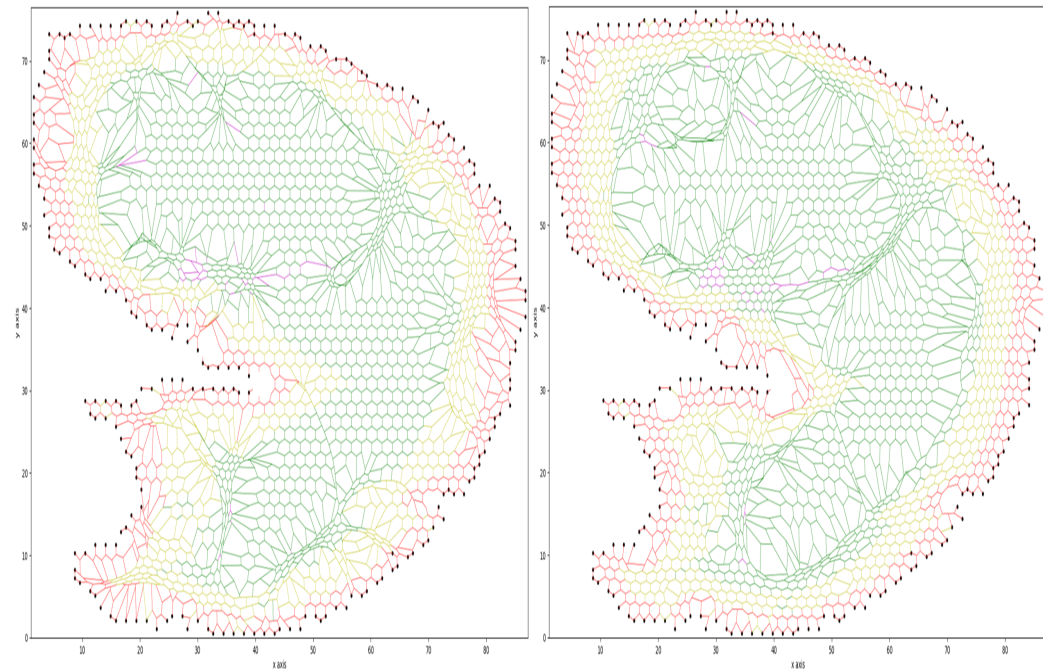
6.1 Structural Progression of IPF

At the beginning of each independent model simulation, the network structure was pre-stressed by altering the equilibrium spring length after the baseline configuration was constructed, and the boundary nodes fixed. This was done to define the level of disease of the network model, as seen in Figure 6.1. Figure 6.1 illustrates the progressive onset of fibrosis as the concentration of spring stiffness increases in the network model. Figure 6.1a demonstrates the baseline configuration prior to any spring stiffening in the model. The uniform distribution of hexagons along the network boundary showcases healthy lung tissue with no radiological features of fibrosis. As fibrosis begins to manifest, the network structure begins to diverge from its normal orientation and develop fibrotic-like clusters starting in the peripheral portions of the lung that begin to span across regions, as seen in figure 6.1b, which represents the lung with 25% of the springs stiffened. Figure 6.1c highlights the progressive nature of IPF as the model hits 50% of spring stiffness. The image starts to define the structural features associated with IPF, with parts of the interior portion exhibiting fibrosis, and the number of initiation sites increasing as the regional expansion of fibrosis becomes more prominent. The probabilities that govern the network boundaries continue to reveal progressive onset of fibrosis as the hexagons in the interior portion of the lung remains intact, with well-defined reticulation in the outer regions becoming more established. At 75% stiffness, Figure 6.1d demonstrates the hallmark radiological features of IPF, which contain cross sectional septal thickening, reticulation, traction bronchiectasis, and honeycombing, which is defined as the tight layered hexagonal structures in the peripheral portions of the lung. The interior portions of lung show continued progression of fibrous with well-defined interconnected lesional patterns that are manifested across the lung boundaries, and pockets of healthy lung that remain intact.



(a) 0% Stiffened (Baseline configuration)

(b) 25% Stiffened



(c) 50% Stiffened

(d) 75% Stiffened

Figure 6.1: Cross sectional depictions of the simulation model at $N = 100$ and $EquLen = 0.3$ for 0% (a), 25% (b), 50% (c), and 75% (d) stiffened concentration levels capturing the progressive onset of fibrosis about the network model.

6.2 Decrease in Mechanical Properties

Idiopathic pulmonary fibrosis, or IPF, can be segmented into three phases, the initiation, progression, and manifestation phase. In the network model, after the simulation was executed the total spring energy was calculated and normalized by dividing the maximum energy of the model at each concentration point for both the expanded and contracted energy states of the network. The total normalized spring energy for each concentration interval was graph, as seen in Figure 6.2. A polynomial smoothing methodology was

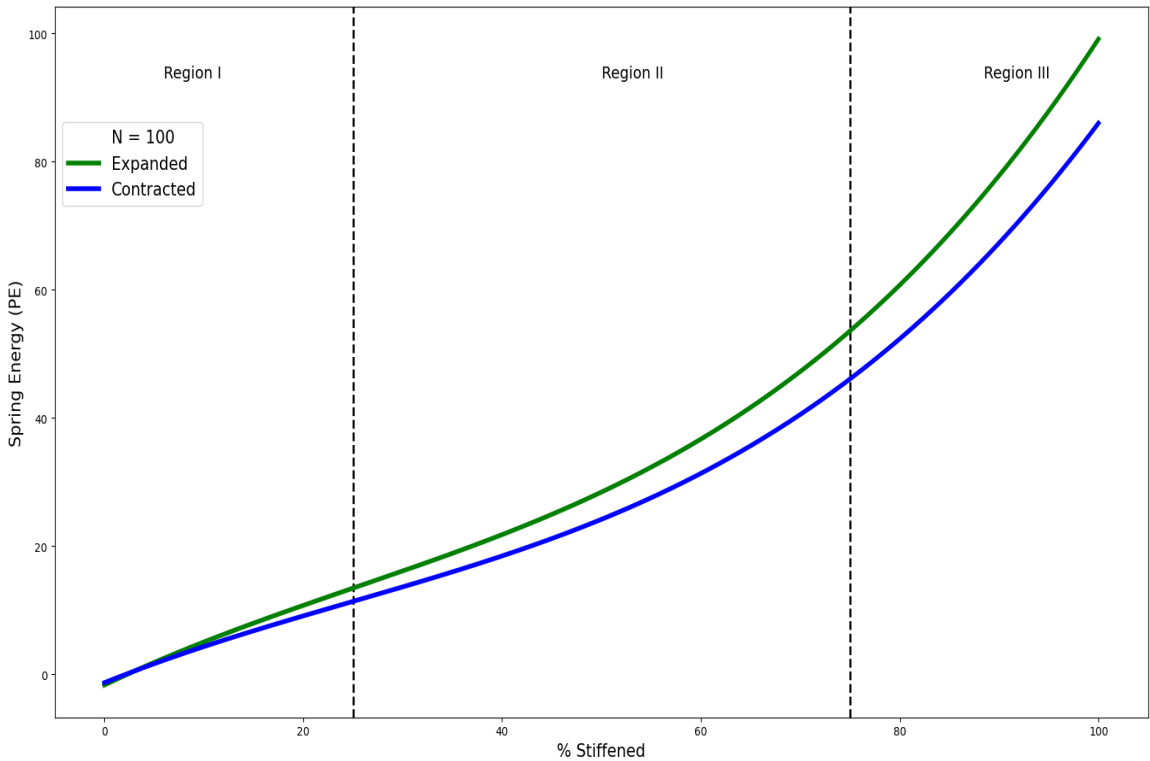


Figure 6.2: Graph of $N = 100$ and $EquLen = 0.3$ network simulation capturing the expansion and contraction energies. The distances between the equilibrium configurations are greater in the expanded position, therefore possess a greater overall energy.

applied to smooth the raw data by reducing the energy noise of the graph. The simulation model was broken into 3 distinct regions. Region I corresponded to the concentration of

stiff springs in the network that were $< 25\%$, also known as the initiation phase, or early onset stage. Region II corresponded to the number of stiff springs between 25% and 75% , which was known as the progression phase, and Region III corresponded to the number of stiff springs $>75\%$, also known as the manifestation phase, or late stage.

In the early stages of the disease when the concentration of stiff springs is less than 25% , the beginning of an exponential curve can be observed. The normalized difference between the expanded and contracted energies starts at 0% and increase to 14% by the end of the Region boundary. The normalized energy difference at a specific concentration stiffness, E_{nd} , was determined by

$$E_{nd} = \frac{e_e - e_c}{E_d} , \quad (6.1)$$

where e_e , and e_c are the total spring energies of the expanded and contract network, and E_d is the maximum difference in energy amongst all iterations. E_{nd} defines the amount of effort required for the network to complete a respiratory cycle at a given concentration, relative to the entire network. As seen in Figure 6.3, the slope of the fitted curve in Region I is 0.43 , which defines the change in spring energy per each change in concentration stiffness. This value increases exponentially until it reaches Region II, where the relationship between the energy difference between the two states change and the slope defines a new relationship between the Region boundaries. The E_{nd} in Region II are 15% at the beginning of the boundary and 58% at the end. The gradual increase in energy accounts for the continued progression of fibrosis in IPF. The slope of the fitted curve between network concentration 25% and 75% is 0.85 , where the shift in slope accounts for the increased local and regional clusters of fibrosis. When the concentration of spring stiffness surpasses 75% , the simulation enters Region III where the coupling of the clinical and mechanical function of IPF manifest, as the progression of the disease becomes irreversible and follows a general linear trend. As seen in Figure 6.3, the slope of the Region III boundary is 1.98 , which corresponds to more than double that of Region II, highlighting the increased energy requirement need to expand the lung as the disease progresses. The effects of Region III may hold less

significance on the patient health than other Regions, since the percolation threshold may have occurred prior to manifestation. The percolation threshold of the models was defined as the concentration point where more than 50% of the normalized difference in energy was required to expand and contract the network. In the simulation, where the value of $N = 100$ and the $EquLen = 0.3$, the percolation threshold occurred when 67% of the network springs were stiffened. The percolation threshold of the model can shift depending on the disease state, which was defined by the equilibrium spring length of the network. These distinct regional boundaries help explain why the mechanical decline is highly dependent on not only the level of fibrosis, but also the spatial arrangement that define them.

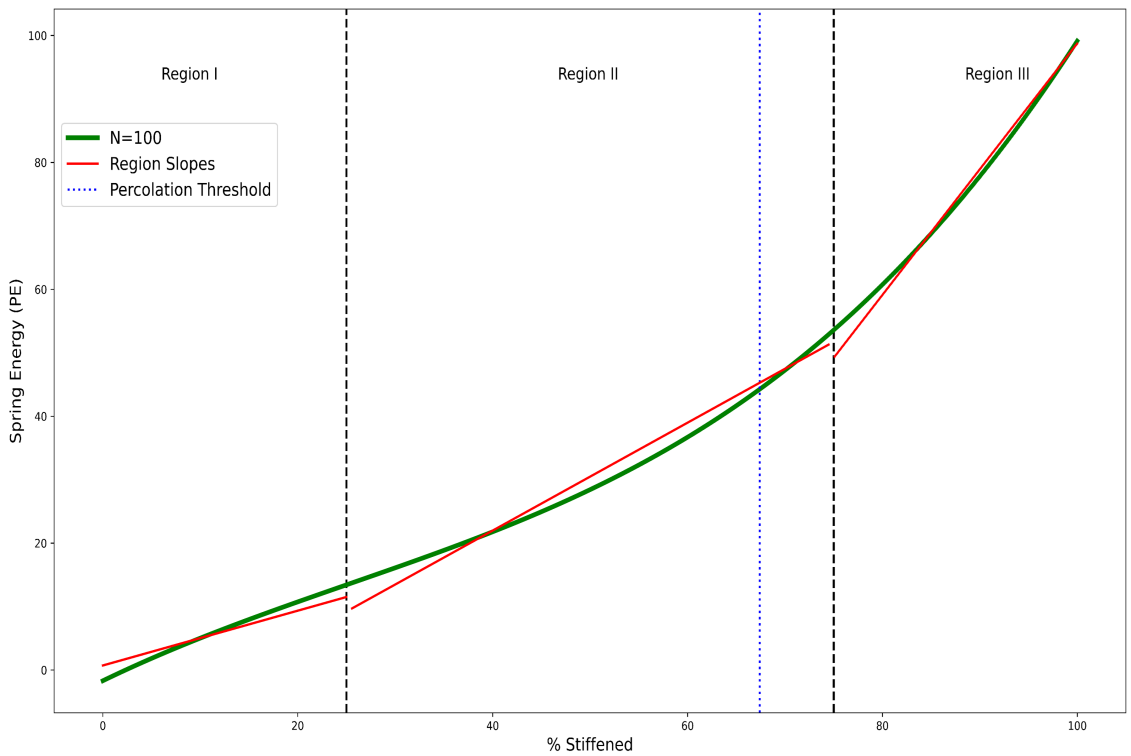


Figure 6.3: Observe the distinct slopes in Regions I-III as the incidences of fibrosis increase in the expanded state for $N = 100$ and $EquLen = 0.3$. The Percolation Threshold is established when $c = 67\%$.

6.3 Model Parameter Tuning

Sections 6.1 and 6.2 examined a simulation model where the value of $N = 100$, and the $EquLen = 0.3$. In this section, various combinations of the two parameters are analyzed to examine how the modification of the parameters affected the simulation model. To begin, set values of $N = 1, 25, 50$, and 100 were selected and modeled with an equilibrium length of 0.3 . The distribution of N values were selected to examine how the change in regional fibrosis governed by the strain dependent random walk effects how the initiation, progression, and manifestation phases of IPF are formed in the model. Figure 6.4, shows how the values of $N = 25$ and $N = 100$ were modeled and analyzed.

At low concentrations of fibrosis, Figure 6.4a and Figure 6.4b, the number of incidents of localized fibrosis are inversely proportional to the value of N . As N increases the number of localized clusters decrease as the model progresses. At concentration levels above 50%, as the simulation progresses, the model demonstrates that the number of initial clusters begin to plateau. The regional incidents of fibrosis disperse, and the model adjust itself to a lower energy configuration. In addition, the cross sectional lesional patterns begin to manifest and establish itself in the interior lung. Figure 6.5 demonstrates how the underline trend in energy varies as the spread of fibrosis, N , is adjusted. As N increases, the slope of the ratios between spring stiffness and spring energy increase, specifically in Region II. This change is attributed to the spatial organization of the lung. As more regional and cross-sectional clusters are formed, more stress is introduced in system, which in turn, requires more energy to adjust the network.

Analogous to the parameter adjustments of N , the equilibrium spring lengths were varied with a set number of values, $0.3, 0.5$, and 0.7 when N was held constant with a value of 100 . The distribution of equilibrium spring values was selected to examine how the change in length from the baseline configuration affected the disease progression of the model. As the equilibrium spring lengths decrease, the radiological characteristic of IPF begin to take shape, as seen in Figure 6.6. In figure 6.6e and 6.6f, the tighter clusters, honeycombing, and cross regional fibrotic effects are all observed in the model where the

value of the equilibrium spring length is lower. The regions with a $EquLen = 0.7$ maintain a greater percentage of structurally coherent hexagons in the model. The disease effects for this length takes a longer time to manifest itself within the network, as seen in Figure 6.7. As the disease progresses, the total spring energy is not only lower in the contracted state, but also requires less energy at a given concentration to expand and contract the lung. The percolation threshold for the $EquLen$ for 0.3, 0.5, and 0.7, are 0.67, 0.71, and 0.72 respectively. The shift in concentration depicts the additional extent of fibrosis needed to trigger the percolation threshold. This illustrates the need to re-iterate the clear relationship between the extent of fibrosis and spatial orientation on the mechanical properties of the lung.

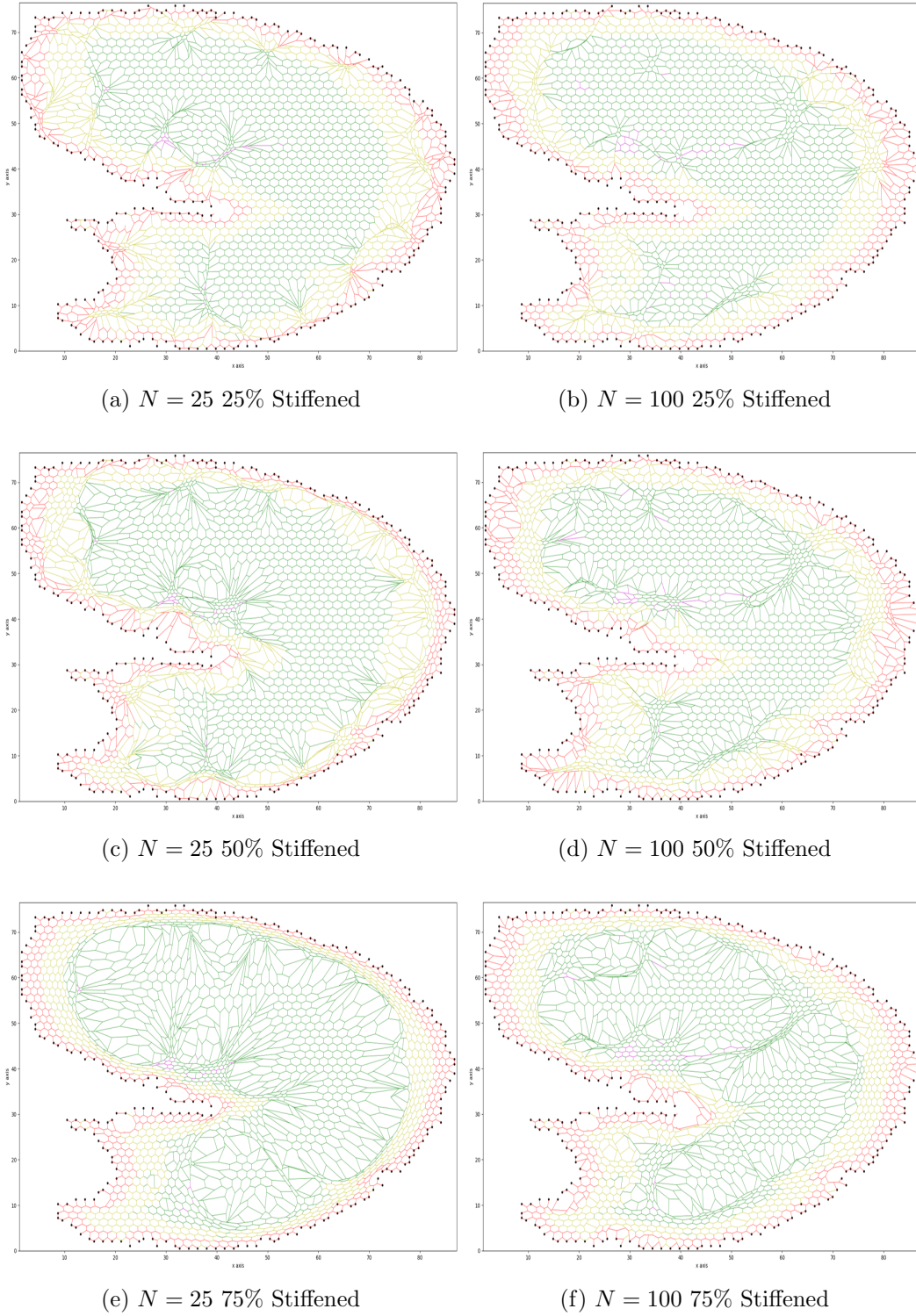


Figure 6.4: Network model configurations comparing the localized progression of IPF for $N = 25$ vs $N = 100$ when $EquLen = 0.3$.

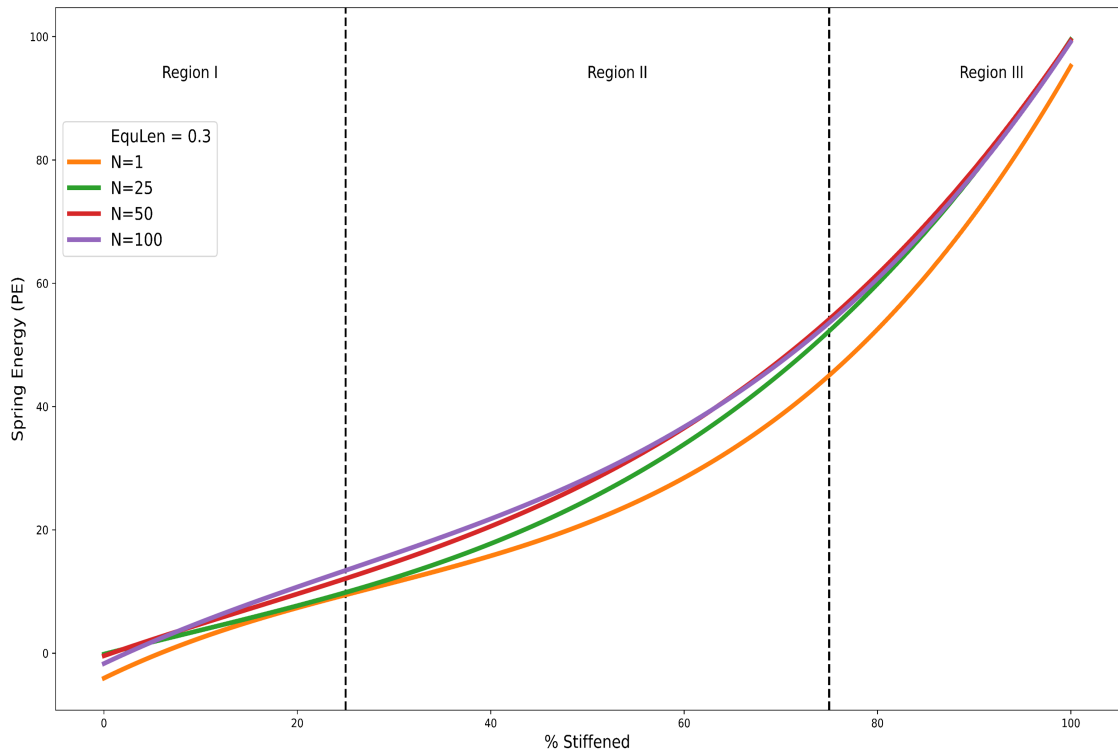


Figure 6.5: Underlined trend in spring energy as local incidences of fibrosis, N are varied when $EquLen = 0.3$. As N increases, the rate of change between regions becomes more linear in Region II.

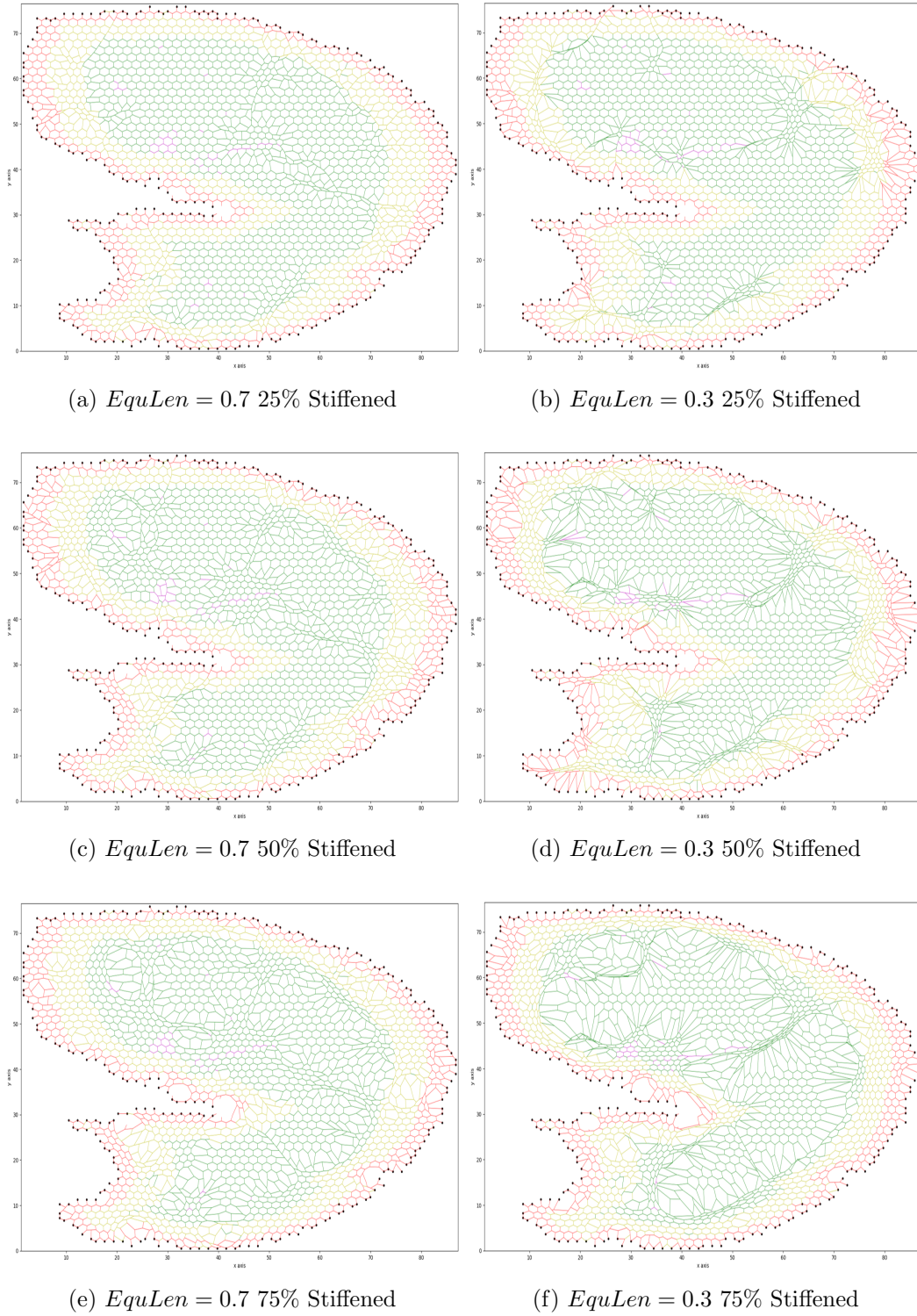


Figure 6.6: Network model configurations comparing the overall progression of IPF when the equilibrium spring lengths are adjusted, $EquLen = 0.7$ vs $EquLen = 0.3$ when $N = 100$.

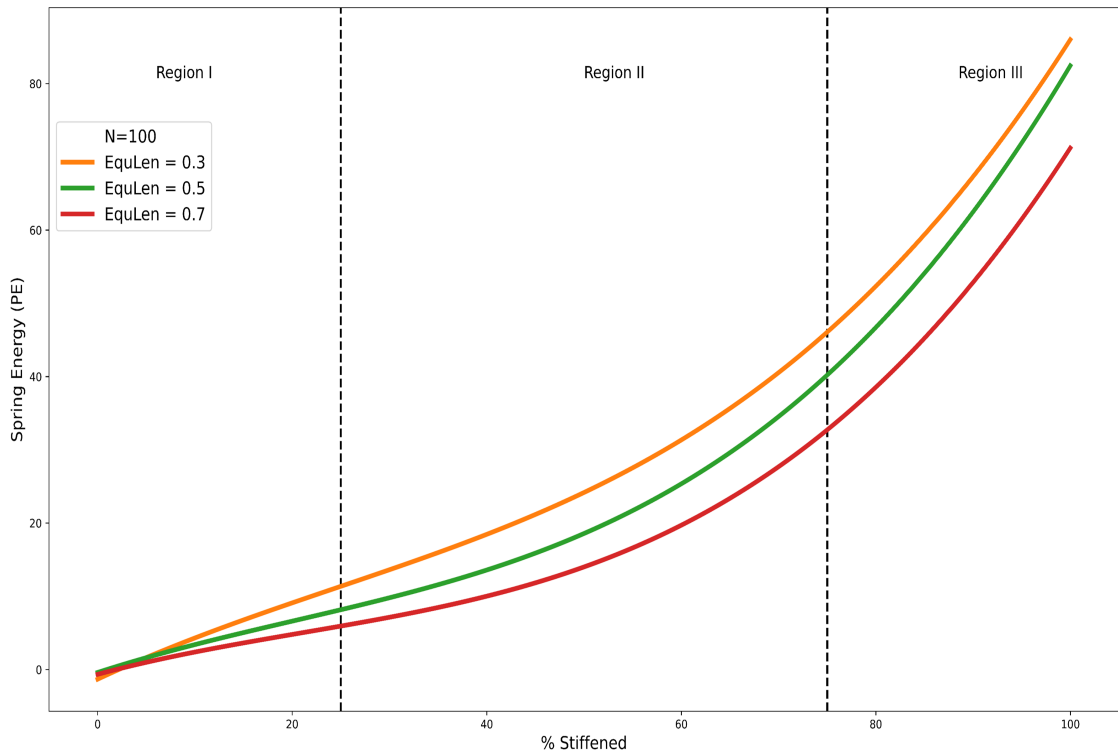


Figure 6.7: PE trends highlighting the differences in slope when the equilibrium lengths of the network are varied when $N = 100$. As the difference between the $EquLen$ increases, the greater the energy gap between simulation steps.

Chapter 7: Discussion

The progression of IPF is highly depended on the spatial and temporal manifestations of fibrosis within the alveolar intersitium. The characterization of radiological features in HRCT is employed to analyze and differentiate the extent of the disease in patients with IPF. This study witnessed that producing interdependent functions modeled after different parts of the lung, allowed for the reconstruction of cross-sectional representation of the lung as the diseased progressed. Adjusting the strain dependent random walk, and equilibrium spring length parameters of the model allowed for an array of unique depictions of the model at different concentration points. Altering these parameters created the biological diversity clinicians see when interacting with patients IPF since the incidence and progression of IPF are unique for each individual. Thus, a deeper understanding on the motivations of the model, and how each parameter influenced the outcome of the simulation should be taken to realize the similarities between the model and the physiological functions of the disease.

7.1 Model Iteration Motivation

The outlying motivation for creating a dual process for emulating pulmonary fibrosis was to recreate the biophysical properties associated with the progress of IPF. As each pulmonary septa are stiffened in the model, the adjacent septa in the interstitial space experience stress which contributes to additional local manifestation of the disease. One possible explanation for the spatial correlation associated with the disease as the model progresses is the presence of fibrogenesis that generates radial growth of collagen deposition as incidences of fibrosis increase. Another possibility may be that once occurrences of collagen arises in a particular location, the surrounding area increases in stiffness that gives rise to a profibrotic mechanical environment for creating a positive feedback loop in the surrounding tissue. Each rule in the

model is deliberately considered biological assumptions when modeling the system. Rule 1 assumed that fibrosis was random, and that its presences did not influence the overall fibrotic mechanisms. The stiffening of springs along a strain dependent random walk was then produced to represent the correlated local deposition of collagen due to the increased strain of its neighboring lung fibers. Rule 2, consequently assumed the local presence of fibrosis contributes to a significant amount of stress and mechanical dysfunction as the occurrences of fibrosis spreads about the initial onset point. As each rule is applied at random about the starting point, the regional localization of fibrosis is meant to capture the distinct morphological onset of the disease. Each region was given a distinct probability that correlated with the radiological characteristics of the progression of IPF in the lung. Higher probabilities were given to the exterior portion of the model to represent the early onset of fibrosis in the inferior portion of the lung. In addition, random interior springs were selected with similar probabilities to capture the random but distinct instances of acute exacerbation experiences as symptoms worsen that lead to rapid decline in clinical functions. One can see in Figure 7.1, when the model is 25% stiffened and the value of $N = 100$, the model starts to capture the regional manifestation of the disease with a uniform distribution of local fibrosis. The model illustrates that fibrosis development in the lung is not random, but rather progresses with a substantial degree of correlation. The resemblance between Figure 7.1a and 7.1b highlight this correlation, where the model effectively captures the early onset of radiological characteristics of IPF. The defined probability, *EquLen*, and the value of N , enables the ability of the model to create localized instances of fibrosis initiating in the peripheral parts of the lung, as seen in genuine HRCT images.

When parenchymal cells are aggregated, they release profibrotic mediators such as TGF- β , TNF- α , and other chemokines that lead to the recruitment of fibroblast and the production of abnormal levels of ECM proteins which trigger remodeling. These collections of mediators accumulate and spread outwardly throughout the site of initiation thus affecting the neighboring structures and aiding in further deposition and remodeling of lung tissue. This spread of fibrosis is represented by the value of N in the model that accounts for the

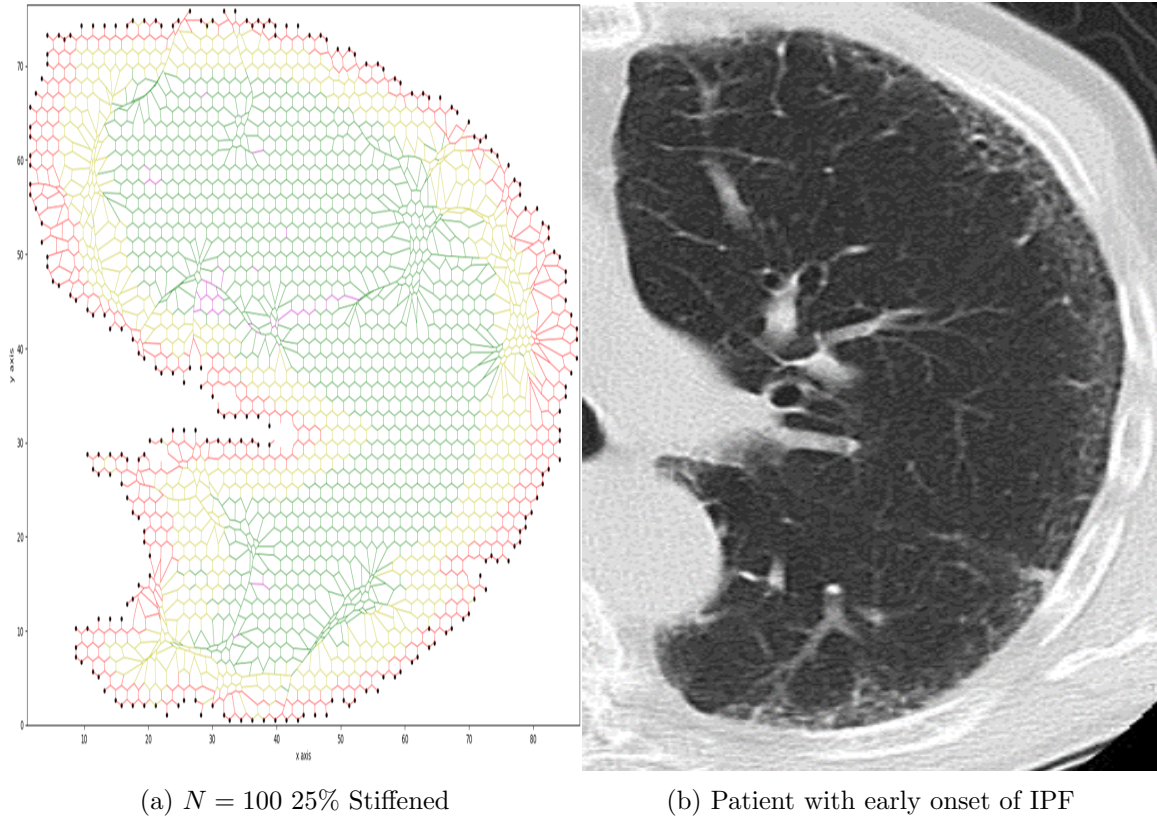


Figure 7.1: Comparison of network model at 25% stiffness (a), to a HRCT image of a patient with early onset radiological symptoms of IPF (b).

lengths of the strain-dependent random walks. Due to the increase in strain in the region, collagen is deposited as a response to the aggregation of fibroblast in the region adjusting for abnormal tissue architecture. In Figure 7.2, in addition to the regional manifestation of the disease progression, one can see the application of rule 2 as the local biological display of fibroblastic foci is randomly distributed within the initiation areas, which coincide with the excess deposition of collagen and fibroblasts and myofibroblasts juxtaposed in linear fashion about the interstitial space. As the model progressed to higher concentration, the influence of each rule and the regional onset of fibrosis established key additional features of the disease over time.

An importance inference of the percolation concept concerns the heterogeneity of the

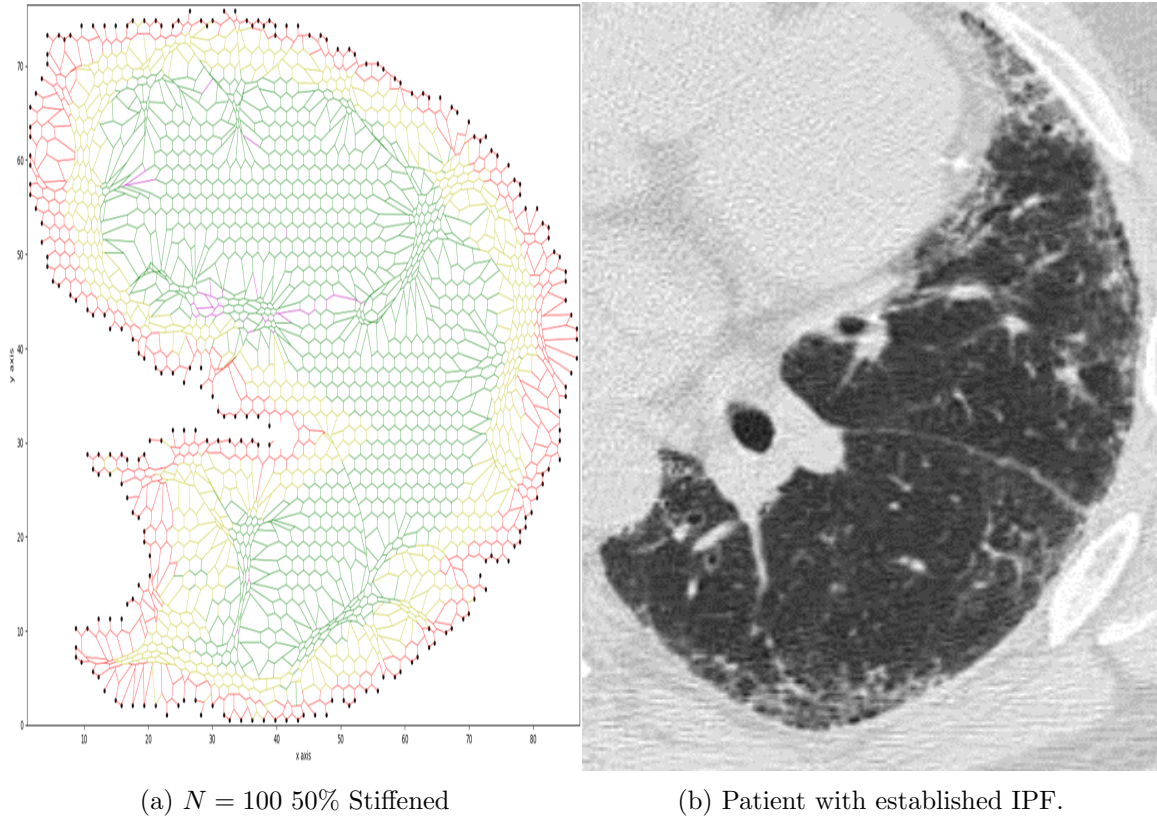
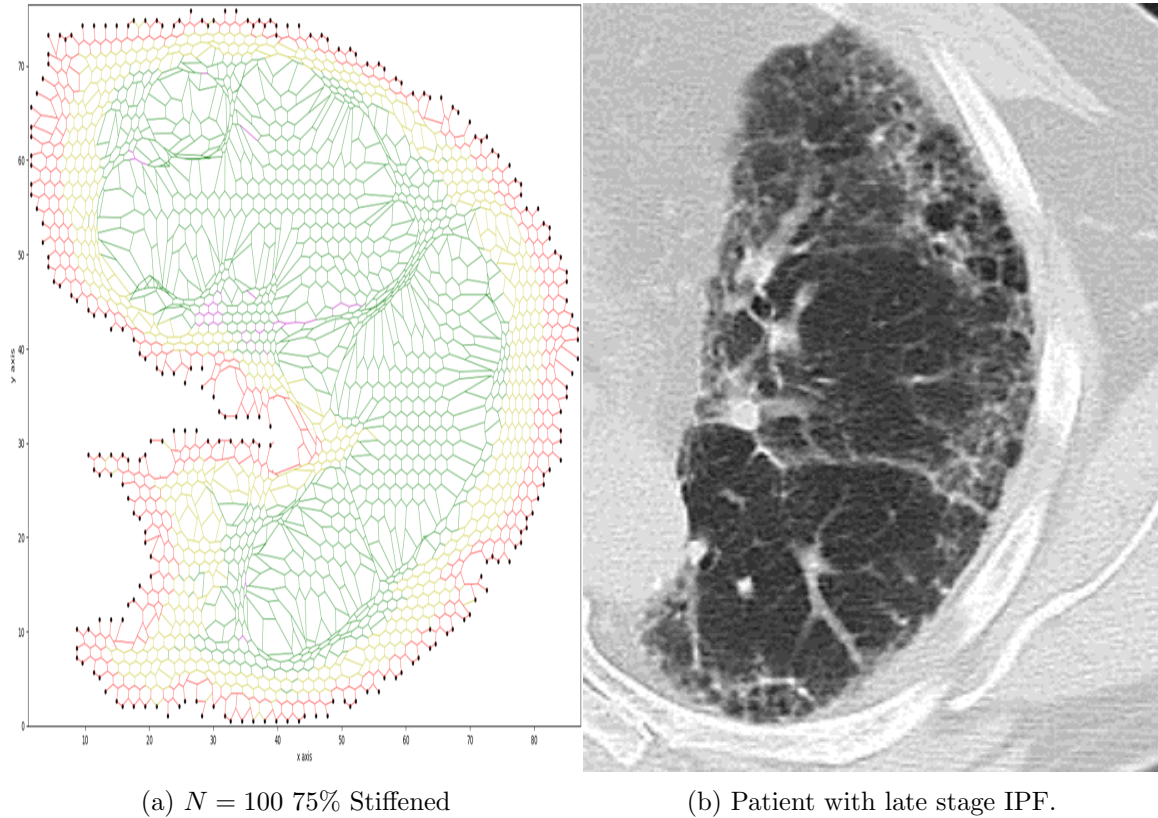


Figure 7.2: Comparison of network model at 50% stiffness (a), to a HRCT image of a patient with established radiological symptoms of IPF (b).

lung as the disease progresses. As the spatial heterogeneity of lung tissue increases, it becomes more clinically observant as it reaches the percolation threshold. Examining Figure 7.3, as heterogeneity increases, percolation also maximizes, which leads to the expansion of stiff springs in lung tissue creating holes in areas that display the classic peripheral honeycomb patterns observed in HRCT images. The textural variability observed can be used to model, predict, and identify patients near the percolation threshold, which can lead to the development of remedies or interventions to help manage patients' disease. Once the critical probability is obtained, the heterogeneity retreats until all the springs are stiffened and the network returns to homogeneity. This occurs because all the springs in the system contain the same physical characteristics, the energy minimization function returns the

network structure to its original spatial configuration.



(a) $N = 100$ 75% Stiffened

(b) Patient with late stage IPF.

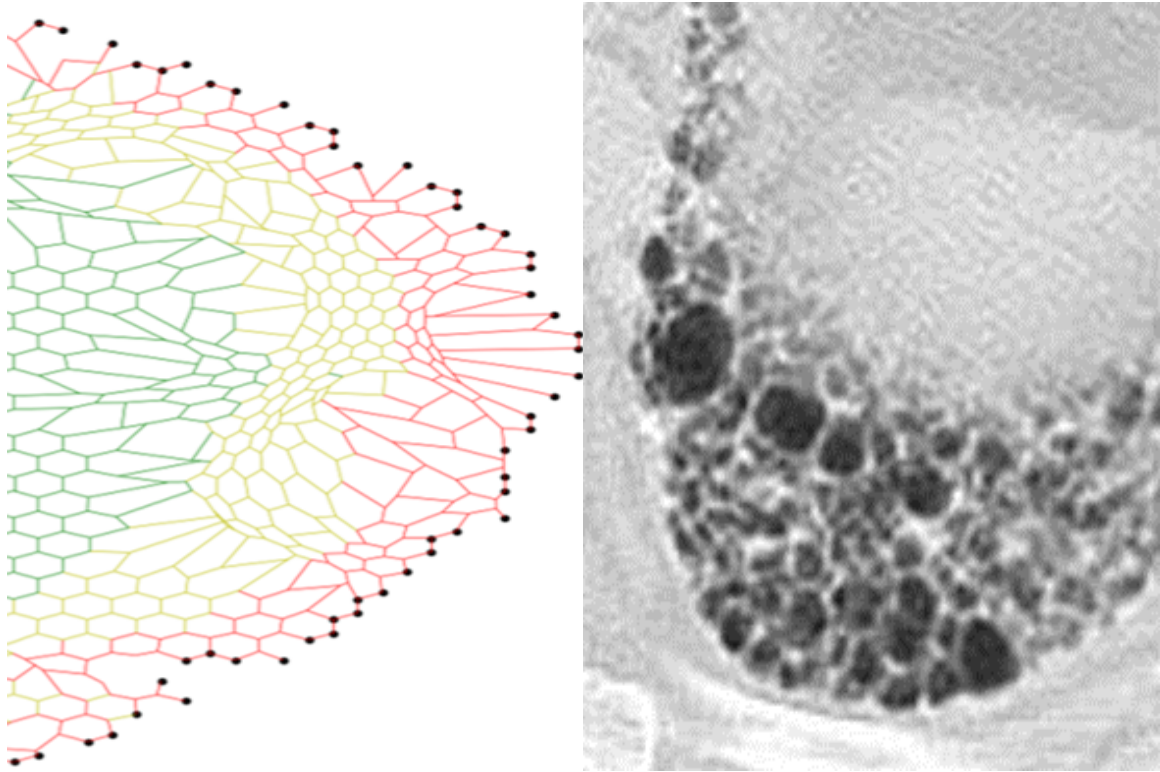
Figure 7.3: Comparison of network model at 75% stiffness (a), to a HRCT image of a patient with late stage radiological symptoms of IPF (b).

7.2 Spatial Pattern Stiffness and Pulmonary Deviation

The importance of the model and how it captured the progression of IPF as the mechanical properties begin to deviate from its normal behavior, was not exclusively functional based. Comprehending the connection between the biological properties, and how collagen load around the affected regions and lung stiffness, provides insights on how the mechanical stiffness and tissue design influence the progression of IPF. Examining the structural arrangements of the hexagon structures in Figures 7.1, 7.2, and 7.3, one can see that the

altered structures at each interval show remarkable resemblance to the HRCT images at various stages of the disease. In normal HRCT images, lung tissue is relatively uniform with alveoli intermittently surrounded by alveolar ducts. The overall alveolar septal thickness of the lung tissue is relatively uniform, however in the altered structures we can see the formation of honeycombing, septal thickening, and the characteristic features of cross-sectional radial growth of fibrosis about the lung structure. As the springs k constants increased and the disease progressed, the shape of the individual hexagons transformed in search for a minimum energy configuration. Since the network boundary was held fixed, the spring were confined to a define space where the movement of the springs were highly correlated to the state of its neighboring spring. Like the biological properties of the ECM, its components are highly dependent of the state of molecular components in its surrounding area. Elevated levels of certain proteins are a strong catalysis to the production of other proteins in IPF. Adjusting the model parameters, was like adjusting the individual components of the ECM and the progression of the disease. Adjusting the probabilities of the lung regions and equilibrium spring lengths allowed for the recreation of radiological features of honeycombing and reticulation in the network, as seen in Figure 7.4. The probabilities were set so that the outer regions had a greater likelihood of selecting a spring, producing the initial localization of fibrosis in the peripheral portion of the lung. The value of the springs' equilibrium length establishes the extent of the disease, which controlled the level of distortion of the hex structure. The smaller the equilibrium value was from the baseline value, the greater the extent of the disease was observed in the model. This established the ability to simulate unique expressions of the diseases depending on the attribute of focus. This is especially important, because the clinical the progression of IPF is highly dependent on the individual in question, and this would allow the customization of progression on a generalized individual use case.

During the network remodeling process its anticipated that at some point the lattice structure will reach a critical density where the spring energy will no longer follow the established trend. At this point, the springs should form clinically late-stage physiological

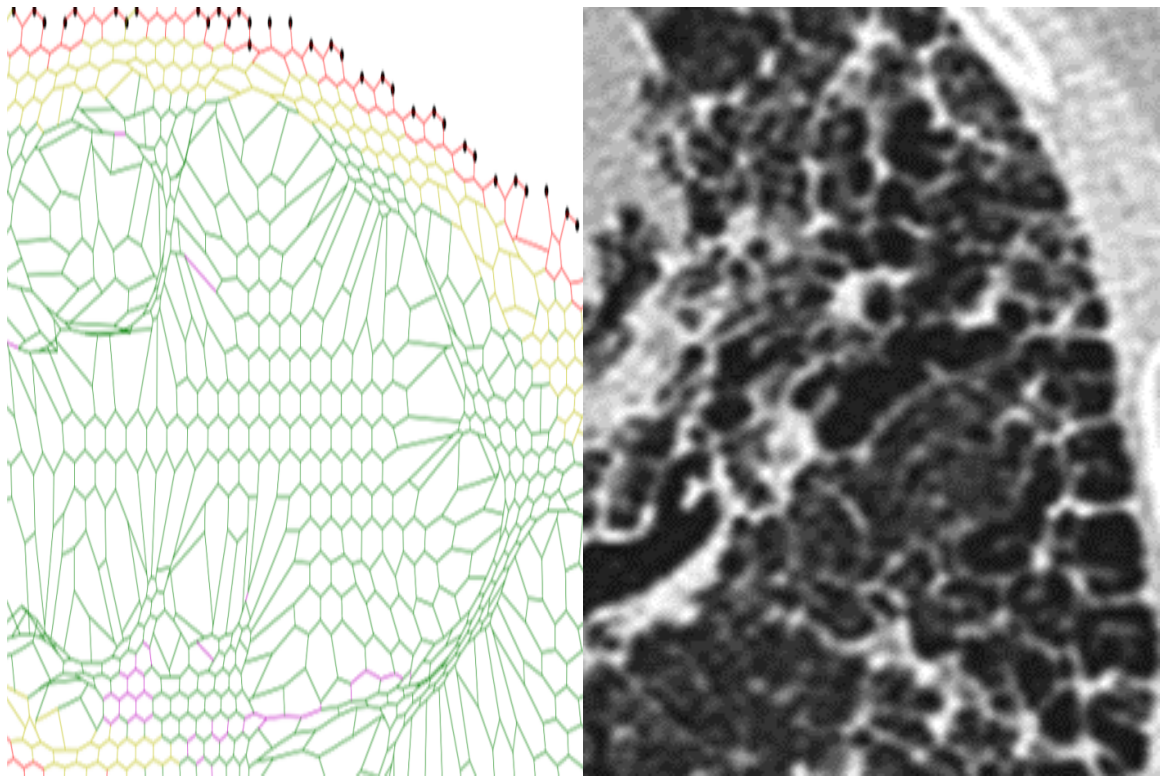


(a) Network model highlighting honeycombing (b) HRCT with prominent inferior honeycombing

Figure 7.4: Focused cross sectional views of the segmented network model and HRCT image capturing distinct characteristics of honeycombing.

characteristics of IPF with unbroken chain or link that percolate from one boundary of the lung to the next. This area can be any that create regional correlated sections of the lung, that present as localized interstitial thickening to peripheral honeycombing structures, as seen in Figure 7.5.

Approaching the critical percolation threshold, one should expect a decrease in normal lung function and an increase in overall prevalence of disease throughout the lung. This type of behavior, or sudden change in lung function may be magnified if there are complementary changes that couple these regional deviations to extend from one section of the lung to another. The percolation threshold of the network model is supported by the evidence shown in Figure 6.2. The graph displays the total energy of the model does not change



(a) Traction bronchiectasis and reticulation (b) Septal thickening and traction bronchiectasis

Figure 7.5: Focused cross sectional views of the segmented network model and HRCT image capturing distinct characteristics of traction bronchiectasis, septal thickening, and reticulation.

linearly, but rather progresses exponentially as the concentration of springs in the network increases. The slope of the energy steady increased until it reached the percolation threshold, where the sharp increase in the slope is observed, Figure 6.3. Once the percolation threshold is reach, a combination of contiguous pathways, and semi-deformed hexagonal structures of altered stiffness can be visible throughout the network. The system starts to display more radiological similarities to late stage IPF, Figure 7.3, as the network stiffness and energy start to increase at an accelerated rate, and the biophysiological characteristics are observed.

To represent the clinical progression of IPF, its progression was broken down into three

distinct Regions. Clinically, the numerical value reflecting concentration of fibrotic foci is used to assess the relevancy of the stages of fibrotic disease. Lower levels of stiffness represent the early to moderate stages of fibrotic disease, Regions I and II, where inferences can be made concerning the longevity of the patient based on their prognosis. Focusing on the early stages of fibrosis suggest that there is a possible connection between fibrotic remodeling and a positive feedback loop between collagen deposition and its consequent effects on the local mechanical function of the lung. This was modeled by the parameter N , where N was adjusted to test the local deposition, and its effects on the model, Figure 6.4. As the value of N increased, the number of localized incidences decreased, but the spread of regional deposition increased. Clinically, Region II could be considered the most significant out of all the regions. As the heterogeneity of the springs begin to manifest in Region I, the slope of total spring energy suggests that the early lesional patterns formed in the perimeter portion of the lung contribute relatively minimal effects on the total system mechanics. By the start of Region III the distinct characteristics of IPF already sets in and compromised the interior portion of the lung where the connected lesions extent about the various boundaries. When this level of fibrosis is reached, symptoms associated with lung dysfunction would have already manifest, and rapid decline in clinical expression is observed. Because of this, the focus should be places on Region II, where the progressive manifestation of the disease can be captured, model, and monitored so that effective care can be tailored to the patient. The exponential nature of the disease can shed light on why some patients have relatively stable physiological parameters for extended periods of time, then experience unforeseen rapid decline right before death.

7.3 Model Shortcomings and Possible Improvements

Many factors can contribute to the symptoms a patient may experience when battling an ailment such as IPF. Symptoms may be a complicated reflection of a single incident, or a culmination of many different factors that contribute to lung dysfunction. Nevertheless, the model presented a rather coherent but physiologically simplistic model of lung tissue over a

wide range of features. Consequently, the model created to mimic the mechanical behavior of the lung, can only do so in the broadest sense without considering a range of biologically relevant properties. During the development of the model, the system emulated a uniform expansion approach to capture the displacement of nodes as the network expanded and contracted to replicate pulmonary respiration although experimental data shows that the lung does not change uniformly with lung expansion. For simplicity, the lung was expanded and contracted uniformly around the center of mass to capture the effects of the change in strain have on the alveolar walls as each breath was taken as the disease progressed. The simplification of the model continued as the network was constructed with linearly elastic springs, which neglected the nonlinear elastic properties of the alveolar septa. The nonlinear component of the springs would provide a more accurate representation of the movement about the system, capturing the functional changes seen in nature. When force was applied to the springs, the model focused specifically on the stretch and didn't incorporate any bend of the springs. This omitted key biological features of the how the spring interact and orientates itself with the lung. The most noticeable limitation of the model is the lack of 3D inferences provided as the model was exclusively modeled in the 2D space. The cross-sectional reconstructions of the 2D model solely provide relatively nominal indications to the systems. The general construction of the 2D model leaves out key implications that can only be resolved as a 3D model is explored.

After examining the unique short coming of the model, various enhancements were taken into consideration as future iterations that could be implemented to improve the model and close the gap between the computational based approach and the physiological characteristics of the biological system. In future versions of the model the system could be expanded by introducing 3D properties of the lung to the network. The first steps in integrating this enhancement would be to define a 3D boundary to best replicate the functional characteristics of the alveolar airspace. This enhancement would provide increased accuracy for the spatial orientation and progression of fibrosis in IPF by examining how the depth and breadth of incidents of fibrous contribute to the architectural decline of the model as fibers

span the cross regional area of the network. In future iterations the model could expand to introduce additional functionality to better analyze the effects of the pressure-volume relationship on lung compliance by including nonlinear parameter to the model, and adjusting the variation of the pulmonary ventilation cycle. The pressure-volume relationship of the lung grows exponentially due of the gradual expansion of its linearly elastic fibers and nonlinear collagen fibers. As the volume reaches its maximum displacement, the pressure would increase rapidly due to the inflexible nature of collagen fibers. The net forces acting on the springs can be varied to add more force to the peripherals and basilar portions of the lobe as the node reaches a certain percentage from it maximum displacement. These additions should mimic the pressure-volume relationship and increase the accuracy of model when comparing the network to its HRCT findings. Although, the network model omits some of the internal mechanical behaviors of the lung by oversimplifying its characteristics, all functions and attributes added to the model effectively captures the general physical and biological aspects of the lung.

Chapter 8: Summary

This study developed a network model that represented the functional parts of the lung and the lungs parenchymal. It explored the theory of percolation of random fibrotic lesions across the lung while simulating local deposition of collagen about newly created fibrotic regions. This allowed the model to display how spatial organization of lung tissue effected the lung stiffness overtime. The elastic properties of the lung arise from the collection of protein fibers acting on the tissue. Previous studies showed how pathological changes in lung stiffness can be described through percolation in tandem with local stiffness through a random walk in a 2D model [54, 55, 59]. This model expanded on these concepts by stating that local stiffness is not attributed by random fashion only, but by a combination of a random walk and a strain dependency of its neighboring nodes. This model also introduced the mechanical property associated with pulmonary respiration, and targeted physiological regions associated with the IPF.

8.1 Model Development

A 2D network of linear elastic springs was constructed to represent a cross sectional portion of a high-resolution computed topography (HRCT) IPF image. The model was developed to reconstruct key radiological features of IPF, and to aid in determining at what point its mechanical functions start to decline as its biological manifestation begin to deviate from traditional representation. The network was built using springs and nodes to represent the spatial organization of the lung and the lungs parenchymal to mimic the ensembled behavior of the fibers. The microscopic study of elasticity for the affected pulmonary parenchyma was calculated by employing both percolation and a strain dependent walk to represent the random and dependent progression of fibrosis. The properties of fibrosis were then

modeled on the organelle level to study how the affected parenchyma effects the overall property of the lung. The model was oscillated to mimic the normal breathing pattern of an average healthy adult to influence the strain dependency of fibrosis; while random springs were stiffened about a defined region with an established probability representing the bilateral basilar subpleural and peripheral regions of the lung to represent the uncorrelated appearance of newly developed fibrotic points in IPF. The nodes were allowed to move in the direction of their applied force and after each iteration, the networks energy was minimized to stabilize the model configuration. This was repeated until all the springs in the network were stiffened, and the model was analyzed to extract the relevant information about simulation. The spatial and mechanical features of the model evaluated and compared with the physiological and radiological characteristics of IPF.

8.2 Model Validation

The individual components of the network model were validated to ensure the accuracy and validity of the functions that contributed to model. Each of the foundational functions were calculated analytically and compared to it computational solution to justify the acceptance of the function. The force and velocity functions were validated by applying a force to a node and comparing its analytical solution to its computational derived solution as it moved about the system. If the computational value fell within a specific error, the function was deemed acceptable. Like the force and velocity equations, increasing the springs k constant and testing a multi-hexagon network applied the same methodology. To validate the pulmonary ventilation function, the systems center of mass was leveraged to track the positions of the x and y components as the nodes moved about the network. Since the center of mass remained constant as the nodes expanded and contracted, the function was considered validated. Lastly the energy minimization function was tested to see if the system converged to an energy minimum. A single node was selected from the baseline configuration, and energy was artificially injected into the system by elongating its spring length. The energy minimization function was applied to the network, and the function was

considered validated if the networks energy returned to its original baseline configuration.

8.3 Results and Discussion

The model was tested by employing an array of values for N and $EquLen$ to justify how each individual component of the lung contributed to the overall elasticity of the lung as fibrosis progressed. As the springs k constants increased, the spatial configuration of the network and the total spring energy of the model was captured and analyzed. The shapes model hexagons were transformed as the network searched for a minimum energy configuration. The transformed hex-like structures depicted multiple structural features, each with its own interpretability. These features resembled the radiological characteristics of honeycombing, septal thickening, reticulation, and traction bronchiectasis as they transition through three distinct regions of concentration within the simulation. The shift in slope as the model progressed defined these regions, and the mechanical properties associate with the lung. The increase in slope as the model transitioned from Region II to Region III coupled with the constant energy distribution between the expanded and contracted states, defined the percolation threshold of the network model. Region II was arguably the most significant amongst all the regions, because although the radiological manifestation of IPF is well defined, normal mechanical properties can still be viewed as the region transitioned from low to high concentrations of stiffness. This attribute can help explain why the clinical expression of IPF tends not to follow the radiological progression of the disease.

Chapter 9: Conclusion

The characterization and differentiation of IPF from other ILD is still highly depending on the individual interpreting the HRCT scan. Various computational methodologies have been developed to characterize the radiological features of IPF. This study took a unique approach by modeling the progression of IPF by creating a computational model of the lung by leveraging existing IPF HRCTs. This was done to simulate the onset and progress of the disease, to examine the radiological features, and monitor the mechanical function of the lung. Despite the novelty of the model, its ability to recreate biologically relevant features provides merit that a computational based approach can be used to reproduced representations of HRCT images. If an efficient model can be constructed, it would be able to model the progress of the disease and determine the critical density at which the disease state will alter the mechanical properties of the lung, resulting in decreased lung function. With this information, physicians would be able to monitor the progression of IPF with greater accuracy and generate treatment options that would provide a better quality of life for their patients.

Bibliography

- [1] E. B. Meltzer and P. W. Noble, “Idiopathic pulmonary fibrosis.” *Orphanet journal of rare diseases*, vol. 3, p. 8, Mar 2008.
- [2] T. A. Wynn, “Common and unique mechanisms regulate fibrosis in various fibroproliferative diseases.” *The Journal of clinical investigation*, vol. 117, pp. 524–9, Mar 2007.
- [3] J. J. Tomasek, G. Gabbiani, B. Hinz, C. Chaponnier, and R. A. Brown, “Myofibroblasts and mechano-regulation of connective tissue remodelling.” *Nature reviews. Molecular cell biology*, vol. 3, pp. 349–63, May 2002.
- [4] K. P. Krafts, “Tissue repair: The hidden drama,” pp. 225–33, Oct-Dec 2010.
- [5] M. O. Li, Y. Y. Wan, S. Sanjabi, A.-K. L. Robertson, and R. A. Flavell, “Transforming growth factor-beta regulation of immune responses.” *Annual review of immunology*, vol. 24, pp. 99–146, 2006.
- [6] T. A. Wynn, “Il-13 effector functions.” *Annual review of immunology*, vol. 21, pp. 425–56, 2003.
- [7] —, “Cellular and molecular mechanisms of fibrosis.” *The Journal of pathology*, vol. 214, pp. 199–210, Jan 2008.
- [8] G. Raghu, H. R. Collard, J. J. Egan, F. J. Martinez, J. Behr, K. K. Brown, T. V. Colby, J.-F. Cordier, K. R. Flaherty, J. A. Lasky, D. A. Lynch, J. H. Ryu, J. J. Swigris, A. U. Wells, J. Ancochea, D. Bouros, C. Carvalho, U. Costabel, M. Ebina, D. M. Hansell, T. Johkoh, D. S. Kim, T. E. J. King, Y. Kondoh, J. Myers, N. L. Muller, A. G. Nicholson, L. Richeldi, M. Selman, R. F. Dudden, B. S. Griss, S. L. Protzko,

- and H. J. Schunemann, “An official ats/ers/jrs/alat statement: idiopathic pulmonary fibrosis: evidence-based guidelines for diagnosis and management.” *American journal of respiratory and critical care medicine*, vol. 183, pp. 788–824, Mar 2011.
- [9] P. J. Wolters, H. R. Collard, and K. D. Jones, “Pathogenesis of idiopathic pulmonary fibrosis,” pp. 157–79, 2014.
- [10] G. Raghu, D. Weycker, J. Edelsberg, W. Z. Bradford, and G. Oster, “Incidence and prevalence of idiopathic pulmonary fibrosis.” *American journal of respiratory and critical care medicine*, vol. 174, pp. 810–6, Oct 2006.
- [11] B. Ley and H. R. Collard, “Epidemiology of idiopathic pulmonary fibrosis,” pp. 483–92, 2013.
- [12] B. Ley, H. R. Collard, and T. E. J. King, “Clinical course and prediction of survival in idiopathic pulmonary fibrosis.” *American journal of respiratory and critical care medicine*, vol. 183, pp. 431–40, Feb 2011.
- [13] D. S. Kim, H. R. Collard, and T. E. J. King, “Classification and natural history of the idiopathic interstitial pneumonias.” *Proceedings of the American Thoracic Society*, vol. 3, pp. 285–92, Jun 2006.
- [14] J. W. Song, S.-B. Hong, C.-M. Lim, Y. Koh, and D. S. Kim, “Acute exacerbation of idiopathic pulmonary fibrosis: incidence, risk factors and outcome.” *The European respiratory journal*, vol. 37, pp. 356–63, Feb 2011.
- [15] H. R. Collard, B. B. Moore, K. R. Flaherty, K. K. Brown, R. J. Kaner, T. E. J. King, J. A. Lasky, J. E. Loyd, I. Noth, M. A. Olman, G. Raghu, J. Roman, J. H. Ryu, D. A. Zisman, G. W. Hunninghake, T. V. Colby, J. J. Egan, D. M. Hansell, T. Johkoh, N. Kaminski, D. S. Kim, Y. Kondoh, D. A. Lynch, J. Muller-Quernheim, J. L. Myers, A. G. Nicholson, M. Selman, G. B. Toews, A. U. Wells, and F. J. Martinez, “Acute exacerbations of idiopathic pulmonary fibrosis.” *American journal of respiratory and critical care medicine*, vol. 176, pp. 636–43, Oct 2007.

- [16] J. S. Lee, J. W. Song, P. J. Wolters, B. M. Elicker, T. E. J. King, D. S. Kim, and H. R. Collard, "Bronchoalveolar lavage pepsin in acute exacerbation of idiopathic pulmonary fibrosis." *The European respiratory journal*, vol. 39, pp. 352–8, Feb 2012.
- [17] S. C. Wootton, D. S. Kim, Y. Kondoh, E. Chen, J. S. Lee, J. W. Song, J. W. Huh, H. Taniguchi, C. Chiu, H. Boushey, L. H. Lancaster, P. J. Wolters, J. DeRisi, D. Ganem, and H. R. Collard, "Viral infection in acute exacerbation of idiopathic pulmonary fibrosis." *American journal of respiratory and critical care medicine*, vol. 183, pp. 1698–702, Jun 2011.
- [18] K. B. Baumgartner, J. M. Samet, C. A. Stidley, T. V. Colby, and J. A. Waldron, "Cigarette smoking: a risk factor for idiopathic pulmonary fibrosis." *American journal of respiratory and critical care medicine*, vol. 155, pp. 242–8, Jan 1997.
- [19] P. B. Bitterman, S. I. Rennard, B. A. Keogh, M. D. Wewers, S. Adelberg, and R. G. Crystal, "Familial idiopathic pulmonary fibrosis. evidence of lung inflammation in unaffected family members." *The New England journal of medicine*, vol. 314, pp. 1343–7, May 1986.
- [20] L. M. Noguee, "Abnormal expression of surfactant protein c and lung disease." *American journal of respiratory cell and molecular biology*, vol. 26, pp. 641–4, Jun 2002.
- [21] L. M. Noguee, A. E. r. Dunbar, S. E. Wert, F. Askin, A. Hamvas, and J. A. Whitsett, "A mutation in the surfactant protein c gene associated with familial interstitial lung disease." *The New England journal of medicine*, vol. 344, pp. 573–9, Feb 2001.
- [22] A. Q. Thomas, K. Lane, J. r. Phillips, M. Prince, C. Markin, M. Speer, D. A. Schwartz, R. Gaddipati, A. Marney, J. Johnson, R. Roberts, J. Haines, M. Stahlman, and J. E. Loyd, "Heterozygosity for a surfactant protein c gene mutation associated with usual interstitial pneumonitis and cellular nonspecific interstitial pneumonitis in one kindred." *American journal of respiratory and critical care medicine*, vol. 165, pp. 1322–8, May 2002.

- [23] M. Y. Armanios, J. J.-L. Chen, J. D. Cogan, J. K. Alder, R. G. Ingersoll, C. Markin, W. E. Lawson, M. Xie, I. Vulto, J. A. r. Phillips, P. M. Lansdorp, C. W. Greider, and J. E. Loyd, “Telomerase mutations in families with idiopathic pulmonary fibrosis.” *The New England journal of medicine*, vol. 356, pp. 1317–26, Mar 2007.
- [24] N. Hutchison, C. Fligny, and J. S. Duffield, “Resident mesenchymal cells and fibrosis,” *Biochimica et Biophysica Acta (BBA) - Molecular Basis of Disease*, vol. 1832, no. 7, pp. 962 – 971, 2013, fibrosis: Translation of basic research to human disease. [Online]. Available: [//www.sciencedirect.com/science/article/pii/S092544391200275X](http://www.sciencedirect.com/science/article/pii/S092544391200275X)
- [25] B. C. Willis, R. M. duBois, and Z. Borok, “Epithelial origin of myofibroblasts during fibrosis in the lung.” *Proceedings of the American Thoracic Society*, vol. 3, pp. 377–82, Jun 2006.
- [26] R. Kalluri and E. G. Neilson, “Epithelial-mesenchymal transition and its implications for fibrosis.” *The Journal of clinical investigation*, vol. 112, pp. 1776–84, Dec 2003.
- [27] M. W. Moore and E. L. Herzog, “Regulation and relevance of myofibroblast responses in idiopathic pulmonary fibrosis.” *Current pathobiology reports*, vol. 1, pp. 199–208, Sep 2013.
- [28] B. Hinz, S. H. Phan, V. J. Thannickal, M. Prunotto, A. Desmouliere, J. Varga, O. De Wever, M. Mareel, and G. Gabbiani, “Recent developments in myofibroblast biology: paradigms for connective tissue remodeling.” *The American journal of pathology*, vol. 180, pp. 1340–55, Apr 2012.
- [29] E. S. White, M. H. Lazar, and V. J. Thannickal, “Pathogenetic mechanisms in usual interstitial pneumonia/idiopathic pulmonary fibrosis.” *The Journal of pathology*, vol. 201, pp. 343–54, Nov 2003.
- [30] T. M. Maher, I. C. Evans, S. E. Bottoms, P. F. Mercer, A. J. Thorley, A. G. Nicholson, G. J. Laurent, T. D. Tetley, R. C. Chambers, and R. J. McAnulty, “Diminished

- prostaglandin e2 contributes to the apoptosis paradox in idiopathic pulmonary fibrosis.” *American journal of respiratory and critical care medicine*, vol. 182, pp. 73–82, Jul 2010.
- [31] M. W. Parker, D. Rossi, M. Peterson, K. Smith, K. Sikström, E. S. White, J. E. Connett, C. A. Henke, O. Larsson, and P. B. Bitterman, “Fibrotic extracellular matrix activates a profibrotic positive feedback loop,” *The Journal of Clinical Investigation*, vol. 124, no. 4, pp. 1622–1635, 4 2014. [Online]. Available: <https://www.jci.org/articles/view/71386>
- [32] N. L. Halliday and J. J. Tomasek, “Mechanical properties of the extracellular matrix influence fibronectin fibril assembly in vitro.” *Experimental cell research*, vol. 217, pp. 109–17, Mar 1995.
- [33] O. Larsson, B. Tian, and N. Sonenberg, “Toward a genome-wide landscape of translational control.” *Cold Spring Harbor perspectives in biology*, vol. 5, p. a012302, Jan 2013.
- [34] R. Kalluri and R. A. Weinberg, “The basics of epithelial-mesenchymal transition,” pp. 1420–8, Jun 2009.
- [35] G. S. Horan, S. Wood, V. Ona, D. J. Li, M. E. Lukashev, P. H. Weinreb, K. J. Simon, K. Hahm, N. E. Allaire, N. J. Rinaldi, J. Goyal, C. A. Feghali-Bostwick, E. L. Matteson, C. O’Hara, R. Lafyatis, G. S. Davis, X. Huang, D. Sheppard, and S. M. Violette, “Partial inhibition of integrin $\alpha(v)\beta6$ prevents pulmonary fibrosis without exacerbating inflammation.” *American journal of respiratory and critical care medicine*, vol. 177, pp. 56–65, Jan 2008.
- [36] A. Bandyopadhyay and S. Raghavan, “Defining the role of integrin $\alpha v \beta 6$ in cancer,” pp. 645–52, Jul 2009.
- [37] J. P. Annes, Y. Chen, J. S. Munger, and D. B. Rifkin, “Integrin $\alpha v \beta 6$ -mediated activation of latent $\text{tgf-}\beta$ requires the latent $\text{tgf-}\beta$ binding protein-1,” *The*

Journal of Cell Biology, vol. 165, no. 5, pp. 723–734, 2004. [Online]. Available: <http://jcb.rupress.org/content/165/5/723>

- [38] A. B. Roberts, A. Russo, A. Felici, and K. C. Flanders, “Smad3: a key player in pathogenetic mechanisms dependent on tgf-beta.” *Annals of the New York Academy of Sciences*, vol. 995, pp. 1–10, May 2003.
- [39] M. H. Branton and J. B. Kopp, “Tgf-beta and fibrosis.” *Microbes and infection*, vol. 1, pp. 1349–65, Dec 1999.
- [40] C. M. Osowski and F. Urano, “Measuring er stress and the unfolded protein response using mammalian tissue culture system,” pp. 71–92, 2011.
- [41] P. Walter and D. Ron, “The unfolded protein response: from stress pathway to homeostatic regulation.” *Science (New York, N.Y.)*, vol. 334, pp. 1081–6, Nov 2011.
- [42] H. Tanjore, T. S. Blackwell, and W. E. Lawson, “Emerging evidence for endoplasmic reticulum stress in the pathogenesis of idiopathic pulmonary fibrosis.” *American journal of physiology. Lung cellular and molecular physiology*, vol. 302, pp. L721–9, Apr 2012.
- [43] S.-I. Cha, C. J. Ryerson, J. S. Lee, J. Kukreja, S. S. Barry, K. D. Jones, B. M. Elicker, D. S. Kim, F. R. Papa, H. R. Collard, and P. J. Wolters, “Cleaved cytokeratin-18 is a mechanistically informative biomarker in idiopathic pulmonary fibrosis.” *Respiratory research*, vol. 13, p. 105, Nov 2012.
- [44] C. D. Cool, S. D. Groshong, P. R. Rai, P. M. Henson, J. S. Stewart, and K. K. Brown, “Fibroblast foci are not discrete sites of lung injury or repair: the fibroblast reticulum.” *American journal of respiratory and critical care medicine*, vol. 174, pp. 654–8, Sep 2006.
- [45] W. D. Travis, U. Costabel, D. M. Hansell, T. E. J. King, D. A. Lynch, A. G. Nicholson, C. J. Ryerson, J. H. Ryu, M. Selman, A. U. Wells, J. Behr, D. Bouros, K. K. Brown,

- T. V. Colby, H. R. Collard, C. R. Cordeiro, V. Cottin, B. Crestani, M. Drent, R. F. Duden, J. Egan, K. Flaherty, C. Hogaboam, Y. Inoue, T. Johkoh, D. S. Kim, M. Kitaichi, J. Loyd, F. J. Martinez, J. Myers, S. Protzko, G. Raghu, L. Richeldi, N. Sverzellati, J. Swigris, and D. Valeyre, “An official american thoracic society/european respiratory society statement: Update of the international multidisciplinary classification of the idiopathic interstitial pneumonias.” *American journal of respiratory and critical care medicine*, vol. 188, pp. 733–48, Sep 2013.
- [46] M. B. Gotway, M. M. Freemer, and T. E. King, “Challenges in pulmonary fibrosis · 1: Use of high resolution ct scanning of the lung for the evaluation of patients with idiopathic interstitial pneumonias,” pp. 546–53, Jun 2007.
- [47] N. Sverzellati, “Highlights of hrct imaging in ipf,” *Respiratory Research*, vol. 14, no. 1, p. S3, 2013. [Online]. Available: <http://dx.doi.org/10.1186/1465-9921-14-S1-S3>
- [48] J. S. Lee, D. A. Lynch, S. Sharma, K. K. Brown, and N. L. Muller, “Organizing pneumonia: prognostic implication of high-resolution computed tomography features.” *Journal of computer assisted tomography*, vol. 27, pp. 260–5, Mar-Apr 2003.
- [49] R. du Bois and T. E. King, “Challenges in pulmonary fibrosis · 5: The nsip/uip debate,” pp. 1008–12, Nov 2007.
- [50] K. R. Flaherty, G. B. Toews, W. D. Travis, T. V. Colby, E. A. Kazerooni, B. H. Gross, A. Jain, R. L. r. Strawderman, R. Paine, A. Flint, J. P. r. Lynch, and F. J. Martinez, “Clinical significance of histological classification of idiopathic interstitial pneumonia.” *The European respiratory journal*, vol. 19, pp. 275–83, Feb 2002.
- [51] K. R. Flaherty, E. L. Thwaite, E. A. Kazerooni, B. H. Gross, G. B. Toews, T. V. Colby, W. D. Travis, J. A. Mumford, S. Murray, A. Flint, J. P. r. Lynch, and F. J. Martinez, “Radiological versus histological diagnosis in uip and nsip: survival implications.” *Thorax*, vol. 58, pp. 143–8, Feb 2003.

- [52] D. Stauffer and A. Aharony, *Introduction to percolation theory*. London; Bristol, PA: Taylor & Francis, 1994.
- [53] B. Suki, D. Stamenovic, and R. Hubmayr, “Lung parenchymal mechanics,” pp. 1317–51, Jul 2011.
- [54] F. S. A. Cavalcante, S. Ito, K. Brewer, H. Sakai, A. M. Alencar, M. P. Almeida, J. S. Andrade, A. Majumdar, E. P. Ingenito, and B. Suki, “Mechanical interactions between collagen and proteoglycans: implications for the stability of lung tissue,” *Journal of Applied Physiology*, vol. 98, no. 2, pp. 672–679, 2005. [Online]. Available: <http://jap.physiology.org/content/98/2/672>
- [55] J. H. T. Bates, G. S. Davis, A. Majumdar, K. J. Butnor, and B. Suki, “Linking parenchymal disease progression to changes in lung mechanical function by percolation,” pp. 617–23, Sep 2007.
- [56] H. R. Collard, T. E. J. King, B. B. Bartelson, J. S. Vourlekis, M. I. Schwarz, and K. K. Brown, “Changes in clinical and physiologic variables predict survival in idiopathic pulmonary fibrosis.” *American journal of respiratory and critical care medicine*, vol. 168, pp. 538–42, Sep 2003.
- [57] F. J. Martinez, S. Safrin, D. Weycker, K. M. Starko, W. Z. Bradford, T. E. J. King, K. R. Flaherty, D. A. Schwartz, P. W. Noble, G. Raghu, and K. K. Brown, “The clinical course of patients with idiopathic pulmonary fibrosis.” *Annals of internal medicine*, vol. 142, pp. 963–7, Jun 2005.
- [58] R. M. du Bois, D. Weycker, C. Albera, W. Z. Bradford, U. Costabel, A. Kartashov, T. E. J. King, L. Lancaster, P. W. Noble, S. A. Sahn, M. Thomeer, D. Valeyre, and A. U. Wells, “Forced vital capacity in patients with idiopathic pulmonary fibrosis: test properties and minimal clinically important difference.” *American journal of respiratory and critical care medicine*, vol. 184, pp. 1382–9, Dec 2011.

- [59] C. L. N. Oliveira, J. H. T. Bates, and B. Suki, “A network model of correlated growth of tissue stiffening in pulmonary fibrosis,” *New Journal of Physics*, vol. 16, no. 6, p. 065022, 2014. [Online]. Available: <http://stacks.iop.org/1367-2630/16/i=6/a=065022>
- [60] S. Hallett, F. Toro, and J. Ashurst, *Physiology, Tidal Volume*, T. I. F. S. Publishing, Ed. In: StatPearls [Internet], 2022.
- [61] H. Qiu, D. Weng, T. Chen, L. Shen, S.-S. Chen, Y.-R. Wei, Q. Wu, M.-M. Zhao, Q.-H. Li, Y. Hu, Y. Zhang, Y. Zhou, Y.-L. Su, F. Zhang, L.-Q. Lu, N.-Y. Zhou, S.-L. Li, L.-L. Zhang, C. Wang, and H.-P. Li, “Stimulator of interferon genes deficiency in acute exacerbation of idiopathic pulmonary fibrosis,” *Frontiers in Immunology*, vol. 8, dec 2017.
- [62] T. H. Sisson, T. M. Maher, I. O. Ajayi, J. E. King, P. D. Higgins, A. J. Booth, R. L. Sagana, S. K. Huang, E. S. White, B. B. Moore, and J. C. Horowitz, “Increased survivin expression contributes to apoptosis-resistance in IPF fibroblasts,” *Advances in Bioscience and Biotechnology*, vol. 03, no. 06, pp. 657–664, 2012.

Curriculum Vitae

John O. Sangobowale grew up in The Bronx, New York. He attended University of Virginia, where he received his Bachelor of Science in Chemistry with a specialization in Biochemistry in 2009. He went on to receive his Master of Business Administration from the Hagan School of Business at Iona College in 2011. He was employed as a Research Scientist focusing on drug development for seven years prior to becoming a Data Scientist. He looks forward to continuing his career in the field of Bioinformatics and Computational Biology.